# SYNTHESIS AND OXIDATION OF NON-STOICHIOMETRIC TUNGSTEN CARBIDE STUDIED BY SCANNING TUNNELING MICROSCOPY/SPECTROSCOPY

---

A THESIS

PRESENTED TO THE FACULTY OF THE SCHOOL OF ENGINEERING AND APPLIED SCIENCES

UNIVERSITY OF VIRGINIA

IN PARTIAL FULFILLMENT OF THE REQUIREMENTS FOR THE DEGREE OF

MASTER OF SCIENCE (ENGINEERING PHYSICS)

BY

J. BRANDON MCCLIMON

JUNE, 2013

# APPROVAL SHEET

The thesis is submitted in partial fulfillment of the requirements
for the degree of
Master of Science
(Engineering Physics)

J. Brandon McClimon J. BRANDON MCCLIMON
Author

This thesis has been read and approved by the examining Committee:

Petra Reinke PETRA REINKE
Thesis advisor

William C. Johnson WILLIAM C. JOHNSON
Committee Chair

Olivier Pfister OLIVIER PFISTER

Accepted for the School of Engineering and Applied Science:

James H. Ayl

Dean, School of Engineering and Applied Science

June, 2013

## Abstract

Tungsten Carbide (WC) is a promising catalyst material for applications where cost is paramount, such as microbial fuel cells. Unfortunately, oxidation depresses performance which is a critical problem with respect to long term performance. In this work, non-stoichiometric carbon-rich WC is investigated to infer whether an excess of carbon near the surface can reduce or be utilized to repair oxidation of the active catalytic surface. The carbides are synthesized via a physical vapor deposition of metallic tungsten and $C_{60}$, which allows fine control over the composition of the resulting film. The films are studied predominantly via Scanning Tunneling Microscopy/Spectroscopy (STM/STS).

Prior to synthesizing the carbide, a number of RT depositions are performed onto graphite substrates to understand the interactions between the $C_{60}$ and W prior to thermally-induced destruction of the $C_{60}$ cage and formation of the carbides. These experiments showed a surprising lack of interaction between small W clusters and adjacent $C_{60}$ molecules. This result contrasts with literature of analogous experiments showing significant charge transfer from W to $C_{60}$ and strong interaction as a result. For W deposited on top of $C_{60}$ layers, it is found that isolated W atoms diffuse easily into the interstices of the $C_{60}$ matrix and that for high coverages, interactions between the W and $C_{60}$ induce a significant reduction in the $C_{60}$ bandgap. These interactions can also stabilize very small islands of $C_{60}$ on graphite that otherwise require hundreds of molecules before a stationary $C_{60}$ island can form.

Intermediate annealing at 400-500°C of $C_{60}$ on epitaxial W/MgO(100) produces novel nanostructures with a very similar size and shape to $C_{60}$ but with metallic conductivity, a unique atomic-scale stripe pattern on their surface, occasional mobility under the influence of the STM tip, and show signs of evolving towards $WO_3$ under oxidation. These structures increase in diameter and slowly dissolve into the W surface under increasing annealing temperatures.

Carbide thin films are synthesized by codeposition onto MgO substrates held above 600˚C. These thin films are determined to be predominantly metastable, cubic $WC_{1-x}$ phase. At a C/W ratio of 60/40 and above, carbon is observed to surface segregate and form graphite on the surface of the film. At a ratio of 60/40 the surface is heavily populated with graphene, rather than graphite.

Oxidation of the films at elevated temperatures in UHV shows that morphological changes, even at atomic resolution, were absent. STS shows that signs of oxidation overspread the surface immediately but that $WO_3$ nucleates well-defined islands which grow in size with harsher oxidation conditions. For the graphite covered surfaces, graphite appears to protect the underlying carbide from oxidation, and between 300 and 400˚C, $O_2$ begins to etch the graphite. The underlying carbide appears to oxidize similarly to films without a graphitized surface. Overall, the WC films oxidize much less rapidly than W clusters on graphite. Attempts to regenerate the oxidized carbide surface via annealing met with mixed results. Carbon diffuses easily through the oxide film and graphitizes the surface. There are signs that the $WO_3$ layer might decrease in thickness.

## Acknowledgments

This thesis could not have happened without the help of numerous people. First and foremost is Prof. Reinke. Petra helped me get my feet under me early on in my studies and has provided numerous ideas and limitless support in structuring this investigation and interpreting the results. My lab-mates as well have been a tremendous resource. Harmonie Sahalov laid the groundwork on this project with her investigation of Vanadium interactions with $C_{60}$. Chris Nolph, Sarah O'Donell, and Kiril Simov taught me much of the nuts and bolts of operating the vacuum system and STM and provided advice on the best ways to navigate a post-graduate degree. Gopal Ramalingam and Ehsan Monazami Alipour have been close confidants and have helped directly with some of the measurements presented here, for which I am very grateful. Matt Schneider performed all of the TEM measurements discussed in Section 4.6.

Numerous other students in the department have provided encouragement, advice, and company along the way, including but not limited to Ryan Comes, Chris Petz, Chris Duska, Justin Erwin, Jatin Amatya, Rob Golden, Balaji Kannan, Matt Steiner, Bonnie McFarland, Brad Richards, Theron Rodgers, Junchong Shen, Kathleen Shugart, and Arwen Wilson.

I thank Dr. Dmitri Pestov at VCU for performing XPS on numerous samples, only a small fraction of which are discussed in this thesis.

I thank my wife Tricia and my son Liam for the patience to let me pursue this degree. It has been every bit as fulfilling as I had hoped from the outset.

Finally, none of this research could happen without the support of the public, in our case taking the form of a National Science Foundation grant from the Division of Materials Research (Ceramics), DMR-100580.

# Table of Contents

# List of Figures

# List of Tables

# Chapter I. Introduction

Tungsten Carbide (WC) has occupied a place of promise in the catalysis community ever since it was found that its valence band shows remarkable similarity to that of Pt,[1] implying that they might show similar catalytic properties. This proved not to be the case. WC does not show similar reactivities or selectivities for the reactions for which Pt is the dominant catalyst. Nevertheless, WC and other transition metal carbides possess unique and oftentimes useful catalytic properties that have been studied in depth for the last several decades.[2–14] Their lower cost, relative to the noble catalysts, along with their biocompatibility and high resistance to CO and $CO_2$ poisoning has made them a strong candidate as an electrocatalyst in microbial-fuel cells,[15,16] where these properties are required. They have also shown promise in direct steam reforming of methane[17] and as a replacement support material for traditional noble metal catalysts.[18]

One issue with their adoption is their susceptibility to oxidation which depresses their catalytic performance.[19–21] Addressing this shortcoming is the main purpose of this project. The approach taken was to synthesize non-stoichiometric carbides which are carbon-rich. The hypothesis is that surface carbon would disrupt oxidation of the transition metal and/or provide a route to recarburize the surface once oxidation has occurred. We used WC specifically as the model to study due to its technical relevance and, not unrelatedly, the effort that has been expended in understanding the surface properties of its stoichiometric forms to date.

To achieve the compositional control required by our approach, $C_{60}$ was used as the carbon precursor rather than the gas-phase carburization that is frequently used to synthesize carbides.[3,22,23] This method gives very fine control over the C/W ratio.

To start the investigation, it seemed worthwhile to understand the interactions that occur when W and $C_{60}$ are in intimate contact. The understanding of interfaces between metals and organic molecules has been a frequent topic of study over the last several decades due to the attendant technologies that require an understanding of these systems.[24] In particular, $C_{60}$ and its derivatives are organic materials of interest since $C_{60}$ has a direct bandgap and electron acceptor properties that suit it to photovoltaic applications.[25–27] It has also been used as novel field effect transistor element.[28–30] The interaction of $C_{60}$ with metal and semiconductor surfaces has been studied extensively, and contributes to an understanding of contact formation and interfacial structures of relevance in many electronic systems.[31–34] In contrast, the deposition of metals on the $C_{60}$ layers, where the metal is the highly mobile reactant, has been studied only in a few systems and is a way to obtain different surface structures than can be made by depositing the metal first.[35–37] The deposition of size-selected Ag clusters showed the dissolution of Ag into the $C_{60}$ layer,[37] which is driven by the strong interaction between isolated Ag-atoms and the molecular matrix.

Several studies of sub-monolayer (ML) films of $C_{60}$ deposited on single crystal metallic surfaces have found strongly reduced bandgaps compared to those present in the bulk phase.[38–42] In all cases, the effect has been attributed to electron donation from the metal to the Lowest Unoccupied Molecular Orbital (LUMO) of the $C_{60}$ molecule along with image charge screening effects. This explanation has been corroborated to some degree by ab initio calculations.[40,41] The physical structure of such systems is relatively uniform, with the $C_{60}$ forming round islands with some hexagonal edges corresponding to the (111) plane of the $C_{60}$ FCC lattice.

Less well studied is the deposition of metals onto $C_{60}$ surfaces. A variety of behaviors have been observed. Au atoms have very high mobility on top of the $C_{60}$ layer and will travel to the edge of the layer before nucleating clusters.[35] Cr nucleates into clusters on the $C_{60}$ surface while Ti and La form a conformal layer due to a chemisorption interaction, then clusters at higher coverages.[43] Ag clusters deposited atop a ML of $C_{60}$ on a Au substrate penetrate the ML to maximize contact with the Au.[37]

To start our study, we observed the interaction of W deposited on $C_{60}$ and $C_{60}$ deposited on W clusters, which are formed on a graphite substrate. In the first system, the metal atoms are highly mobile, in the second system the $C_{60}$ molecules retain a high mobility on the graphite surface, which is exposed in between nanometer-scale W clusters. The resulting surface morphology and electronic structure of the surface is studied using Scanning Tunneling Microscopy (STM) and Scanning Tunneling Spectroscopy (STS). In these experiments, the order of deposition has profound effects on the resulting structure due to the interplay of different mobilities of reactants on the different surfaces. For the W deposited atop the $C_{60}$ interesting chemical interactions occur, which illustrates the impact of metal incorporation on the electronic structure of the molecular matrix.

The next step in the investigation was to study how these surfaces evolve under different annealing temperatures approaching the conditions required to form a carbide film. In the process, it was found that $C_{60}$ atop a W film transform into a novel nanostructure termed henceforth a nanosphere that is investigated and discussed at length in Chapter IV.

Finally, codeposition experiments with the substrate held at a high enough temperature to ensure destruction of the fullerenes and formation of carbide were performed and are discussed in Chapter V.  These films were then exposed to $O_2$ at elevated temperatures to understand their susceptibility to oxidation.  This is the focus of Chapter VI.

# Chapter II. Materials and Experimental Techniques

## Section 2.1: Highly Oriented Pyrolytic Graphite

Graphite is of course familiar to most people who have used a traditional pencil, and this use outlines some of the interesting properties of the material. Graphite is composed of flat sheets of graphene layered atop one another with a separation of 3.5Å between sheets. The interaction between sheets is of the weak van der Waals variety. This weak attraction between sheets is the reason graphite is useful for pencil lead and various lubrication applications; the sheets can be separated with very little effort. The sheets themselves exhibit the same crystallographic structure and many of the same properties of graphene, though interaction between the sheets eliminates the relativistic carrier mobility that is graphene's most exciting property. There is $SP^2$ hybridization of the Carbon orbitals which allows for the 120˚ planar bonding between carbon atoms and the resulting 2-D hexagonal lattice of the sheet itself.

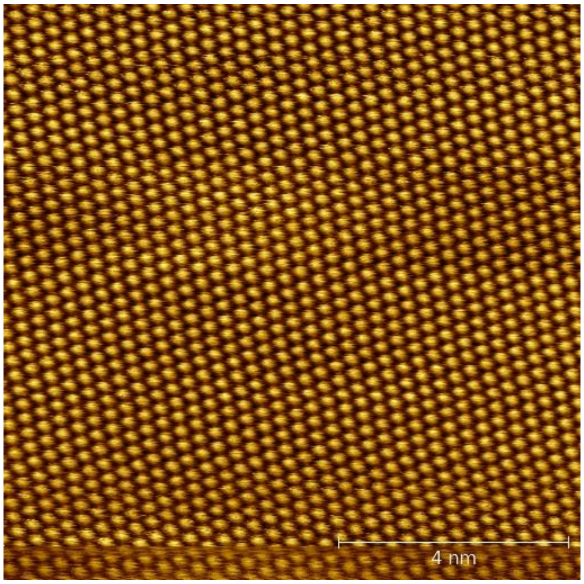

**Figure 1 Typical STM Image of HOPG. 0.05 V, 0.2 nA.**

The graphite used in the experiments is called Highly Oriented Pyrolytic Graphite (HOPG). The lengthy name, though catchy in acronym form, only refers to the synthesis method and indicates that the normal vectors of the graphene sheets of all the grains in the sample are oriented in the same direction to within some tolerance. This tolerance is specified as the grade of the graphite. In the experiments described here, HOPG with a grade of ZYB (Ted Pella Inc.) was used, indicating all grains are oriented within 1.4˚ of each other. Additionally, the grain size was observed to be in excess of 500 nm based on the separation between visible steps in STM images.

HOPG is often used as a standard in STM measurements since it is simple to prepare and relatively straightforward to obtain an atomic resolution image. Figure 1 is a typical STM image of HOPG. HOPG was used as a substrate for deposition in some of the experiments described since it is chemically inert to W and $C_{60}$ in the temperature window of the experiments.

## Section 2.2: Magnesium Oxide (MgO)

MgO is a ceramic that is stable against reduction at high temperatures and low $O_2$ partial pressures and also is commonly used, in single crystal form, as a substrate in UHV deposition experiments due to its tendency to accommodate heteroepitaxial growth.[44–46] MgO has the standard cubic rock salt crystal structure. MgO(001) substrates were selected for use in the high temperature codeposition experiments described here due to its previously demonstrated ability to grow W and WC epitaxially in magnetron sputtered films.[47]

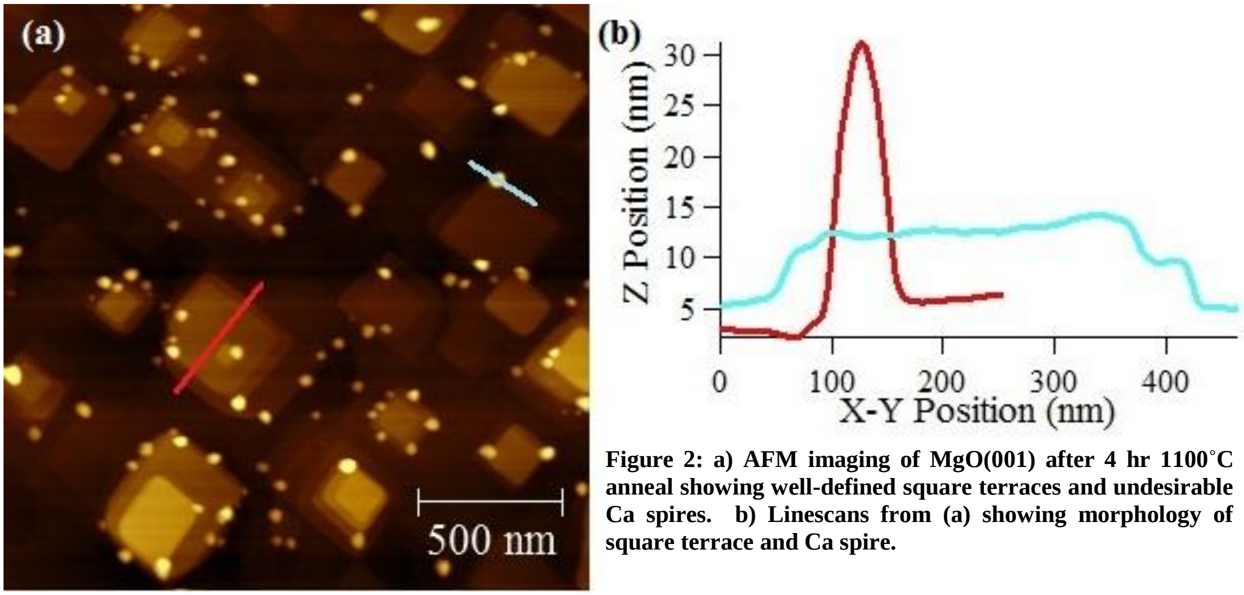

**Figure 2: a) AFM imaging of MgO(001) after 4 hr 1100°C anneal showing well-defined square terraces and undesirable Ca spires. b) Linescans from (a) showing morphology of square terrace and Ca spire.**

To prepare the substrates, a scheme specified in the literature was followed initially that consisted of a 30 s etch in 14.6 M $H_3PO_4$, a rinse with deionized water, and a 2 hr oxygen anneal at 1000˚C in air in a box furnace.[48] It was found immediately that the rinse with deionized water was insufficient to remove all the acid, as white, rough deposits were left on the substrate after the anneal. Ultrasonicating the substrates for several minutes after the etch corrected this issue. Several annealing temperatures and times were tried and 4 hr at 1100˚C provided the best morphology, Figure 2. Characterization of these substrates by Atomic Force Microscopy after the anneal revealed atomically flat cubic terraces up to 300 nm across separated by steps up to 10 nm in height, which was in accordance with expectations from the literature. Additionally, there were numerous spires up to 40 nm in height and 100 nm in diameter. These structures were described as ubiquitous after anneal for all current MgO suppliers by several graduate students in the department who utilize MgO regularly. They are likely surface segregated CaO.[49,50]

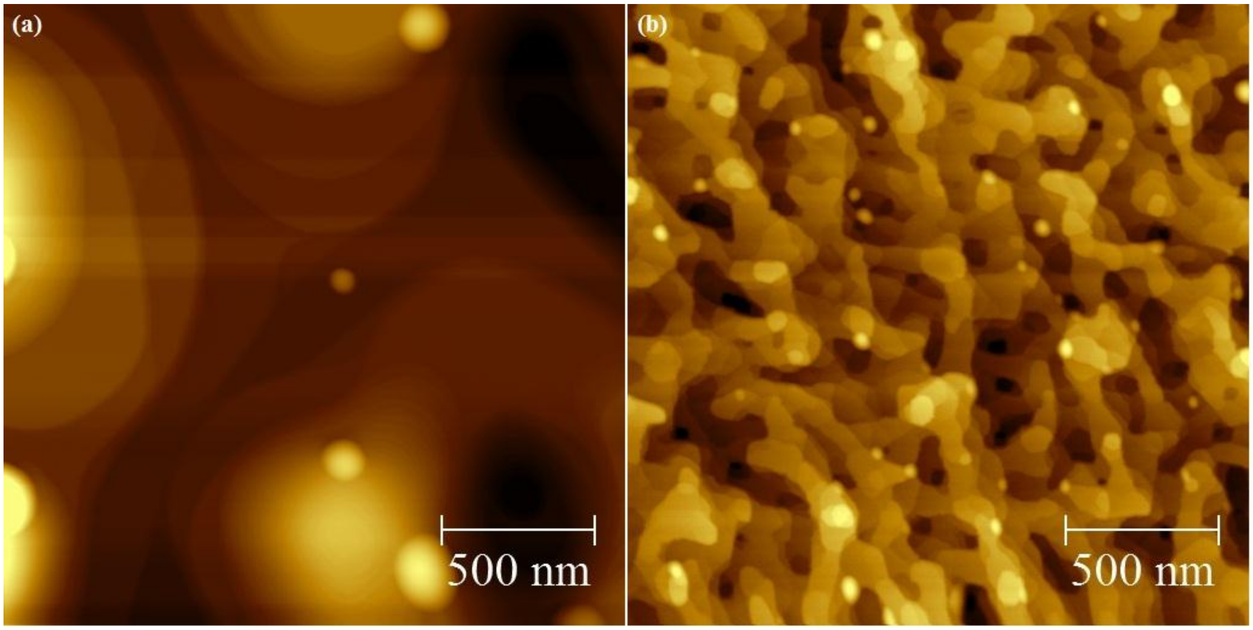

**Figure 3: a) AFM image of MgO(001) after etch and 10 hr 1200˚C anneal showing the consolidation and growth of the Ca protrusions. b) Image of MgO(001) after re-etch and 5 hr 1100˚C anneal showing reduction in density and height of Ca spires relative to single-annealed substrate.**

To combat this issue, I decided to use the surface segregation of Ca to my advantage by extended annealing at very high temperatures followed by an additional acid etch to remove the Ca spires. This was followed by an additional, milder anneal in hopes that near-surface Ca was depleted sufficiently to limit additional surface segregation and the formation of spires. The best results were found for: 30 sec etch, 10 hr 1200˚C anneal, 30 sec etch, 5 hr 1100˚C anneal. The evolution of the surface is displayed in Figure 3. After the initial 1200˚C anneal, the Ca spires had agglomerated into a low density of hemispherical islands up to 40 nm in height and 300 nm across. The large steps between terraces were replaced by many atomic height steps between terraces and the cubic terrace structure was replaced by uniformly curved terrace edges. This surface could prove adequate for many experiments as large atomically flat terrace areas were available with a low density of Ca protrusions, although the gradual transition between terraces could interfere with epitaxy. After the re-etch and re-anneal, the density and height of the protrusions was much reduced relative to the substrates with a single anneal at 1100˚C, with no protrusion rising more than 5 nm above the surrounding surface structure. Terraces remained atomically flat with similar steps of several nm between them although the area of any individual terrace was significantly smaller than on the 1100˚C annealed substrates. The terraces had curved edges in common with the 1200˚C annealed surface which proved useful in ruling out substrate influence on the formation of cubic structure on W/C codeposited films. This substrate pretreatment was followed for all depositions onto MgO substrates in this thesis.

MgO was also synthesized on top of holey carbon TEM grids so depositions could be performed and imaged in the TEM. The synthesis method and characterization of these MgO substrates will be described in Section 4.6.

## Section 2.3: Fullerenes ($C_{60}$)

$C_{60}$ was discovered in 1985[51,52] to great fanfare due to its fascinating properties as an organic direct bandgap semiconductor, a non-polar carbon molecule, and its unique geodesic sphere structure that captured the public imagination. Fullerenes are composed of $SP^2$ hybridized C atoms bonded to three neighbors as in graphite with the atoms forming the corners of pentagons and hexagons on the surface of the molecule, 20 hexagons and 12 pentagons in the case of $C_{60}$. Other geometries with more or less carbon atoms exist constrained by the need to construct a sphere out of hexagons and pentagons, but $C_{60}$ is the most common and is the molecule studied here.

STM studies of $C_{60}$ on various surfaces have found that the molecule forms large islands on weakly interacting substrates such as graphite and stacks up in an FCC structure with the

(111) vector normal to the substrate.[53] On these substrates at room temperature, the molecules have enough energy to excite rotational modes with periods short enough that the molecule appears as a featureless sphere in STM images. More strongly interacting substrates tend to suppress this phenomenon. The interstices between the molecules in the solid form are large, and have been shown to readily accommodate the intercalation of various alkali and alkali earth metals.[54,55] Complexes of $C_{60}$ and transition metals have also been synthesized.[56,57]

## Section 2.4: Metals: Tungsten and Tungsten Carbide

One goal of the later experiments is synthesis of WC to study the resulting surface structure under various synthesis and subsequent oxidation conditions. The W component of these surfaces was evaporated directly from the pure W metal. At room temperature the group VI transition metal W has a stable BCC structure. It is very reactive to $O_2$, readily transforming to a stable $WO_3$. This necessitates UHV conditions to study deposited W via STM.

Figure 4 is the W-C phase diagram.[58] At the temperatures of interest in this study, the only stable phases are W, α-$W_2C$, graphite, and WC as line compounds and in multiphase regions. Metastable species are possible and have been observed on, for instance, MgO.[47]

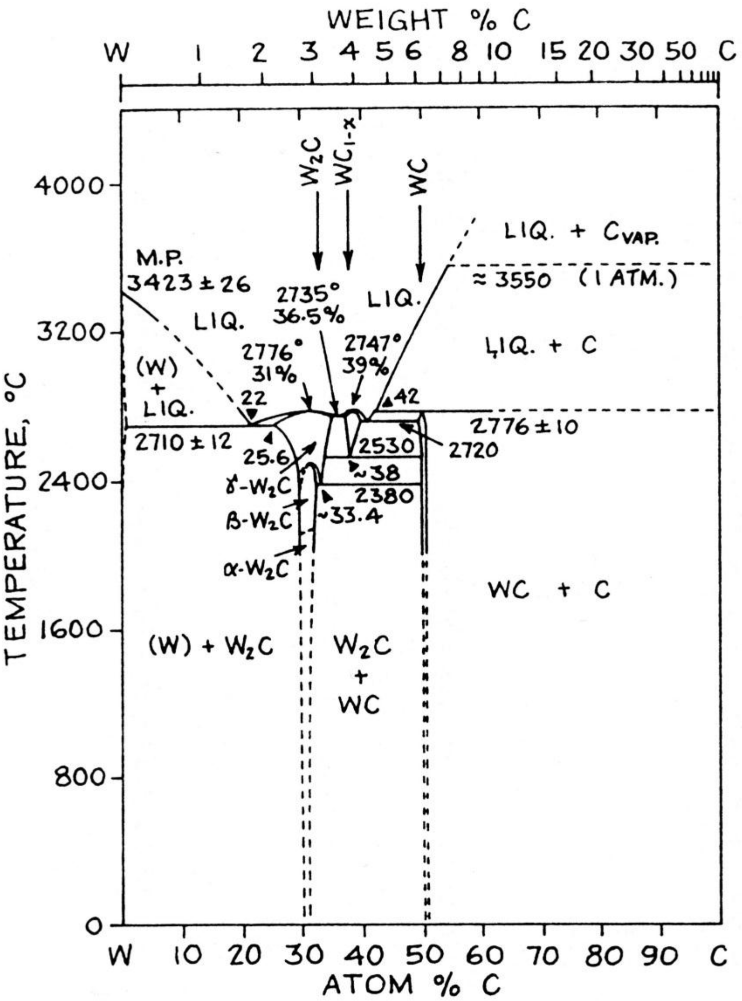

**Figure 4: W-C Phase Diagram**

## Section 2.5: UHV System

The UHV system used by our group for both deposition and STM imaging was manufactured by Omicron. It consists of a deposition chamber where various sources can be attached which are all aimed at a central manipulator arm that allows for axial rotation and translation to allow for sample transfer and to place either the sample or an attached quartz crystal monitor in the deposition region in front of the sources. The ion pump and titanium sublimation pump are both below this chamber. The deposition chamber adjoins the STM chamber which contains a manipulator to transfer the sample into the microscope without breaking UHV conditions. The deposition chamber also adjoins the turbomolecular pump isolated by a large gate valve, and the load lock which is isolated from the deposition chamber by a much smaller gate valve. These two valves allow the deposition and STM chambers to be isolated from the turbomolecular pump, which can be shut down to help minimize vibrations during STM imaging. UHV conditions are maintained by the ion pump and periodic operation of the Titanium Sublimation Pump (TSP). The load lock is also directly connected to the turbo so the load lock can be pumped down to allow sample insertion via an attached manipulator while the main chamber is continuously held at UHV conditions.

As is true of most UHV chambers, all unwelded connections between metal components contain compressed Cu gaskets to minimize gas leakage into the chamber, or, in the case of the load lock, a viton gasket that replaces the Cu gasket after the bakeout. Bakeout is the process by which high vacuum is converted to UHV. Pumping alone cannot achieve UHV in anything like a reasonable amount of time due mostly to the partial pressure of $H_2O$ in the chamber that is a result of water that is adsorbed to essentially all internal surfaces of the chamber and desorbs in an Arrhenius fashion where the activation energy is much, much larger than the thermal energy of the molecules at room temperature, kT. This leads to a high partial pressure of $H_2O$ at the start of pumping due to the large inventory and a very slow decay due to the unfavorable energetics of desorption. The solution is to heat the entire chamber to the point where kT is significantly greater than the activation energy for desorption which increases the rate exponentially and leads to a very rapid reduction in the inventory of adsorbed $H_2O$ in the chamber i.e. bakeout. When the chamber is cooled back down, the partial pressure of $H_2O$ is several orders of magnitude lower and UHV can be maintained with the ion pump and occasional TSP activation. Bakeout is achieved in our chamber by using insulated panels to create a tent that is heated by a resistive element and blower mounted below the table supporting the system. In other labs, bakeout is often achieved by wrapping the chamber in electrical heating tapes and tinfoil insulation.

## Section 2.6: Scanning Tunneling Microscopy

The primary characterization technique used in this thesis is STM. The mechanics of the measurements are relatively straightforward. A W wire that has been etched in NaOH to achieve a tip so sharp that it is terminated by a single atom is brought within ~2 nm of the sample to be studied. Within this range and with a voltage applied between the tip and sample, if there is a reduction in energy by transferring an electron from tip to sample or vice versa (which there will be due to the applied voltage if the sample is a conductor) the probability of quantum mechanical tunneling between tip and sample becomes appreciable.

The wavefunctions of the tip and sample decay exponentially in the vacuum and the resulting tunneling current between the two can be modeled in 1-D using the WKB approximation for a trapezoidal potential as follows:

$$I_t \propto N(E_F)exp\left[-2z\frac{\sqrt{2m(U-E)}}{\hbar}\right]$$

where $N(E_F)$ is the sample's density of states (DOS) at the Fermi Energy, z is the separation between the tip and sample, U-E is the energy difference between the vacuum level and the bound electron energy, and ħ is Planck's constant divided by 2π.[59] The important thing to note is that there is an exponential change in the tunneling current with a linear change in separation, z. This allows the system to be exquisitely sensitive to small changes in tip-sample separation. Figure 5 shows this process visually, with an $E_F$ electron from the tip tunneling into the empty states of the sample. The tip is mounted on a piezoelectric

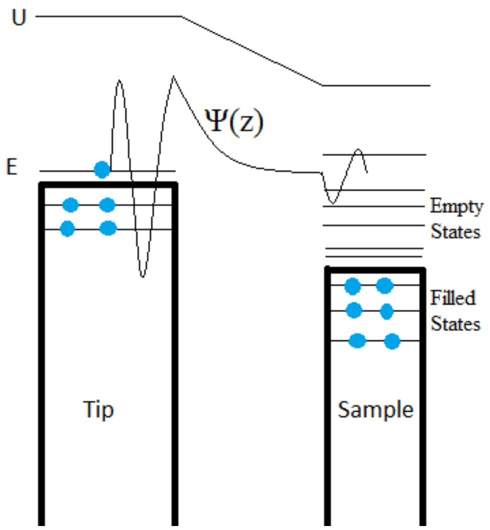

**Figure 5: Visualization of tunneling between metallic tip and sample.**

actuator that can move the tip in all three directions relative to the sample surface. Measurements are normally carried out in "constant current mode," where the tunneling current is fed into feedback circuitry that moves the tip in z to maintain a fixed tunneling current. The piezo is then rastered back and forth across the sample with the (x,y,z) position measured at specified intervals until the entire area of interest has been covered. The collection of coordinates forms an image of the surface of constant Local Density of States (LDOS). This is different from the more general DOS in that there are features in the DOS at the surface of a sample that are absent in the bulk and vice versa, and also because different electron orbitals decay into the vacuum at different rates and the STM is more sensitive to those states that extend farther into the vacuum. These deviations from what would be the simplest interpretation of the images: that the image is just a topograph of the surface atom heights, becomes important when atomic resolution is available. As but one example, Figure 1 is an STM image of HOPG. Recourse to a ball and stick model of a graphene sheet reveals that each C atom has three nearest neighbors commensurate with carbon $SP^2$ bonding, but interpretation of the image as simple atomic topograph indicates that each atom has six nearest neighbors. This is because chemical interaction with the second layer of carbon atoms perturbs the LDOS around every other C atom and causes it to be invisible to the STM, leading to an imaged lattice that is very different from the physical lattice of C atoms at the graphite surface. Examples like this abound in the literature.

In analyzing the images certain changes to the image are made that enhance contrast or highlight certain features. Essentially all images are linearly planarized. This does not introduce significant distortion since the changes tend to amount to a very small azimuthal rotation of the image that enhances contrast because the color scale covers a smaller height range. If very large angles of the surface ralitive relative to the X-Y plane of the tip are corrected for, significant distortion could result since the correction algorithm only pushes each pixel up or down in Z, rather than rotates the entire image in azimuth. This situation was not encountered for any of the figures presented here. Another correction that is occasionally performed is a quadratic leveling, where the image is fitted to a quadratic function in X and Y, which is subsequently subtracted from the image. This correction is justified based on the physical geometry of the piezo scanner. The scanner is referred to as a tube scanner since it is literally a tube that deforms to map the surface. As a result, the tube traces out a parabolic curve over the surface that is not taken into account in the raw images, with the amount of distortion increasing with increasing image area. A quadratic leveling corrects for this faithfully, although a natural quadratic component to the surface curvature can be removed as well, so images presented in this thesis are generally limited to linear planarization.

## Section 2.7 Scanning Tunneling Spectroscopy

Another type of measurement that can be made with the same apparatus used to acquire STM images is Scanning Tunneling Spectroscopy (STS). To perform this measurement, the tip is brought to a specific X-Y position over the sample and the feedback loop is disconnected so that the tip will maintain a constant height Z above the sample. The voltage is then swept through a specified range of voltages while simultaneously measuring the resulting tunneling current. This results in an I-V curve that contains a wealth of data about the electronic structure of the underlying sample. To understand why, a glance back at Figure 5 helps explain. In the figure, the voltage applied between tip and sample determines which, and how many of the empty states of the sample are available to be tunneled into. The tunneling electrons can fall into any of a large number of empty states between $E_F$ of the sample and the applied voltage so that $I_t$ depends on the integrated LDOS up to that voltage. To determine the LDOS at the voltage of interest, the I-V curve must be differentiated so that only the empty states in a small dV near the applied voltage is represented by the dI/dV at a given voltage. However, from the equation in Section 3.6 it is clear that in addition to the integrated LDOS, $I_t$ depends

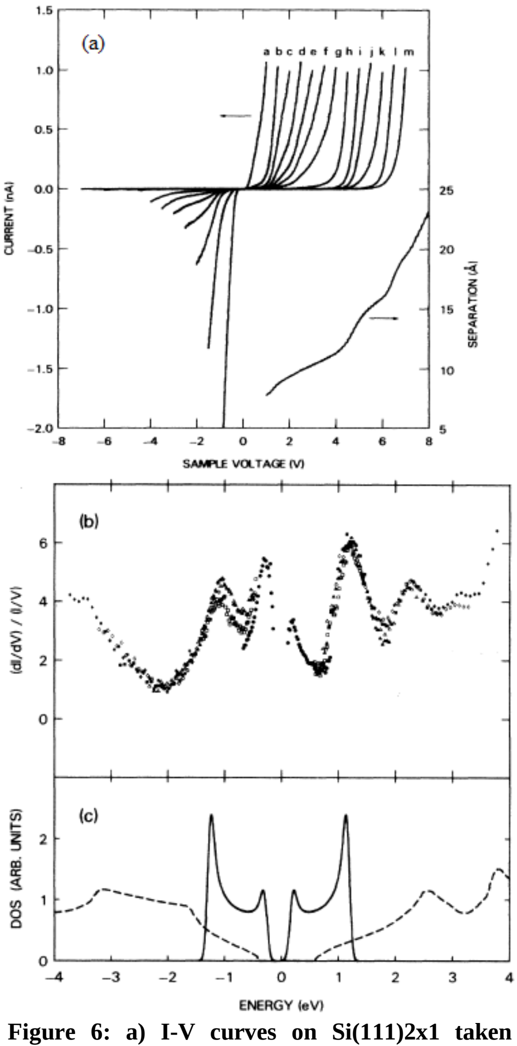

**Figure 6: a) I-V curves on Si(111)2x1 taken at various tip-sample separations b) $(dI/dV)(I/V)^{-1}$ of curves in (a). c) Theoretical DOS from valence and conduction bands along with π-bonded chains (solid)**

exponentially on voltage and separation, and so dI/dV does not show just LDOS but LDOS multiplied by an exponential factor that varies throughout the voltage sweep because of the changing voltage and is different for different tip-sample separations. In practice, this can be done by calculating $(dI/dV)(I/V)^{-1}$ which suppresses the exponential contributions to dI/dV and gives a better approximation to the true LDOS.[60] This can clearly be seen in Figure 6, where the spectra taken at various voltages collapse onto a single curve when $(dI/dV)(I/V)^{-1}$ is calculated.[60] This method is not without issues, however. Noisy spectra, which are normal due to the extremely small currents measured, tend to have the noise exacerbated when these normalized differential conductance spectra are calculated. Also, the edges of bandgaps are problematic in this calculation since $I_t$ goes to zero faster than dI/dV leading to erroneous singularities in the LDOS.[61] In this investigation, dI/dV was calculated; this proved to be adequate to analyze the positions of bandgap edges and general features of the LDOS of the structures studied. Oftentimes, averaging a number of spectra in a homogenous area of the sample led to an easily identified LDOS and minimized problems caused by noise in the spectra. Also, by mapping the dI/dV at a voltage of interest to the X-Y position the spectra was taken, spatial maps could be created that showed how regions with certain spectral features were distributed across a surface. This method of visualization is used extensively in this thesis.

## Section 2.8 Photoemission Spectroscopy

X-Ray Photoemission Spectroscopy utilizes a high energy photon of known energy to knock an electron from an atom at or near the surface of a sample free. The energy of these free electrons leaving the sample is then measured to deduce the binding energy. For this thesis, the high energy photons were created by accelerating electrons to high speed in a vacuum tube which then collide with an Al target. Many electrons are knocked loose from their Al atoms and collide with other atoms until only enough kinetic energy is left to excite elctrons into excited but bound states. The electrons then relax to lower states via the emission of photons. The photons have many energies corresponding to the various shell-to-shell transitions. A single energy is then isolated as well as possible using X-ray mirrors; in our case, the $K_\alpha$ energy of 1486 eV from the 2p to 1s transition is used. These monoenergetic photons then strike the sample and knock electrons free from their atoms through absorption with enough energy to escape the sample and reach a detector.

Evaluating the binding energy of a measured free electron is a straightforward conservation of energy calculation. The binding energy is just the photon energy minus the measured free electron energy minus the work function the electron must overcome at the surface of the sample:

$$E_b = h\upsilon - E_{kin} - \phi$$

This simple equation neglects a number of loss mechanisms by which the emitted electron can lose energy after it's absorption of the photon such as inelastic scattering, plasmon losses, and relaxation shifts.[62] These loss mechanisms can be considered in very precise composition determination and other analyses but were not evaluated as part of this thesis.

XPS is extremely surface sensitive since the deeper in the bulk an electron is liberated the more opportunity there is for interactions such as inelastic scattering that reduce kinetic energy and remove the measured electron from the characteristic binding energy peaks of the spectra. In practice, this means the spectra are only sensitive to the first few nm beneath the surface of a sample. Within this range, XPS provides chemical composition accuracy within 5 to 10% from the relative peak area of certain electron binding energies:

$$\frac{N_1}{N_2} = \frac{A_1}{A_2}\frac{\sigma_2}{\sigma_1}$$

where A is the area of the binding energy peak and σ is the photoelectron excitation cross section.[63] This equation can take other forms that provide additional corrections for the loss mechanisms and detector efficiencies, but is adequate to the task here.

XPS also provides valuable information about bonding in the sample. Bonding alters the electronic configuration of the atom and

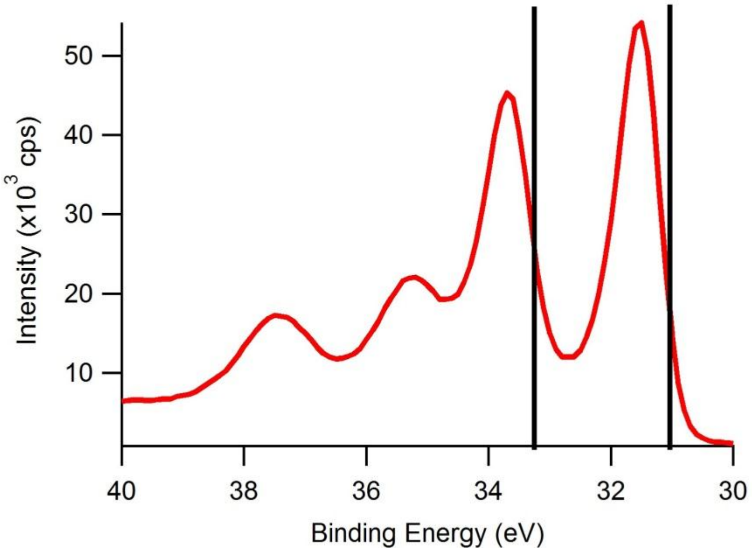

**Figure 7: XPS spectrum of an oxidized WC thin film 4f level. Vertical black lines are the expected peak positions for metallic tungsten.**

causes detectable changes in the binding energy of electrons. These changes manifest themselves, as one might expect, in peak shifts of the characteristic binding energies. Figure 7 provides a representative example. Metallic tungsten exhibits a double peak at 31.0 and 33.2 eV for the 4f electrons due to spin-orbit interactions.[64] In Figure 7, the two peaks have become four with two of the peaks shifted only slightly due to bonding that forms WC and two additional peaks shifted much more substantially due to the presence of $WO_3$. This is the type of chemical information that bridges a gap in information that cannot be provided with STM/STS analysis in isolation.

## Section 2.9: Transmission Electron Microscopy

Transmission Electron Microscopy (TEM) can provide an atomic resolution picture of samples that are thin enough for a beam of 100-300 keV electrons to penetrate in large numbers. In this technique, highly accelerated electrons are focused in much the same way photons are focused, except with magnetic lenses. These electrons can then penetrate a very thin sample (10’s of nm or less) and are focused onto a large phosphor screen where the image is formed. Atoms in the sample scatter electrons out of the focused beam and so the atoms appear as dark spots in the image. This is called the bright field mode of imaging.

Contrast can also be formed by selecting a Bragg peak of electrons diffracting in the sample, which is then projected on the back focal plane as the image. This is referred to as dark field imaging, and is characterized by bright areas (in the real space image) where electrons have diffracted into the chosen Bragg peak, and dark regions where that diffraction peak is not present.

Energy Dispersive Spectroscopy (EDS) can also be performed by measuring the energy of photons emitted from an atom after a core electron is ejected through scattering with an electron in the microscope beam.

For this thesis, only bright field imaging was utilized with EDS to confirm the presence of the expected constituent atoms.

## Section 2.10: Electron Beam Evaporation

To deposit tungsten in this investigation, simple thermal evaporation from a crucible (as was done for the $C_{60}$ in these experiments) is not very practical since W is highly refractory and has a melting temperature of 3422˚C. Instead, electron beam evaporation from a Mantis M-EV source was chosen since only the source material is heated to the required temperature. The principle of operation is very simple. A large voltage (2000 V here) is applied between a filament and the source material. The filament is heated by a direct current until thermionic emission begins. The emitted electrons accelerate and collide with the source material where their energy is thermally dispersed, heating the material. In the case of tungsten, the source rod conducted away too much heat to the water-cooled source housing to attain an appreciable deposition rate so the source rod was notched, as in Figure 8, to limit thermal conduction enough to allow the tip of the rod to melt with a reasonable emission current. A non-standard circular filament was also used to allow more uniform heating of the W. Deposition rates of several monolayers (ML) per minute were attained with emission powers of approximately 180 W.

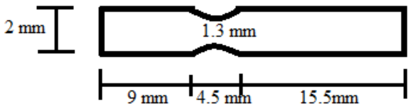

**Figure 8: W source rod**

## Section 2.11: Sample Heaters

Two types of sample heaters were used on the manipulator arm to heat the samples in UHV, either during deposition or for anneals and during oxidation experiments. The first type was a boron nitride radiative heater that allowed temperatures up to 800˚C to be reached at the sample surface. This heater was calibrated via a thermocouple spot welded to a molybdenum sample plate, allowing heater power to be correlated to temperature in vacuum up to approximately 350˚C; above this temperature, the calibration curves provided by Omicron were used to correlate heater power to surface temperature. This heater had an approximately twenty minute delay from setting the appropriate power to the plate reaching the expected temperatures. All annealing/heating times quoted in this manuscript omit this heatup time.

An electron beam heater was also used for some of the codeposition experiments discussed. The mechanism of operation is identical to the electron beam source discussed in the previous section except that the accelerated emission electrons collide with the bottom of the sample plate. This heater has a temperature limit of approximately 1100˚C. There is a permanently mounted thermocouple adjacent to the sample plate whose temperature can be correlated to the temperature on the plate itself via a manufacturer-supplied calibration curve. Additionally, a calibration was performed correlating thermocouple readings to emission power and pyrometer temperature readings on the sample plate itself above 600˚C. Since the thermocouple was about a cm away from the sample, there was a time lag of a minute or more before the temperature differential between the plate and thermocouple was reached. Care had to be taken using this heater's auto-approach function for reaching a temperature as the sample plate temperature could overshoot its target significantly before the appropriate temperature was reached at the thermocouple and prompted the heater to reduce power.

## Section 2.12: $O_2$ Leak Rig

A significant fraction of this investigation is concerned with oxidation of sample surfaces. To perform this oxidation, an $O_2$ leak rig was assembled. As schematically illustrated in Figure 9, the rig consists of a Varian leak valve, a line to the $O_2$ lecture bottle, and a line to the loadlock side of the chamber, allowing the line to be pumped down with the turbo isolated from the sample chamber. Prior to the introduction of $O_2$ a bakeout was performed where all components shown in the figure, with the exception of the regulator and lecture bottle, were heated to ~150˚C for several hours with both isolation valves and the regulator open while pumping with the turbo in order to desorb as much $H_2O$ and other adsorbed gases as possible from the inner walls of the system. At the end of that time, the pumpdown line was isolated and the system was filled with several psi of $O_2$ from the lecture bottle. The line was then pumped down once more with the

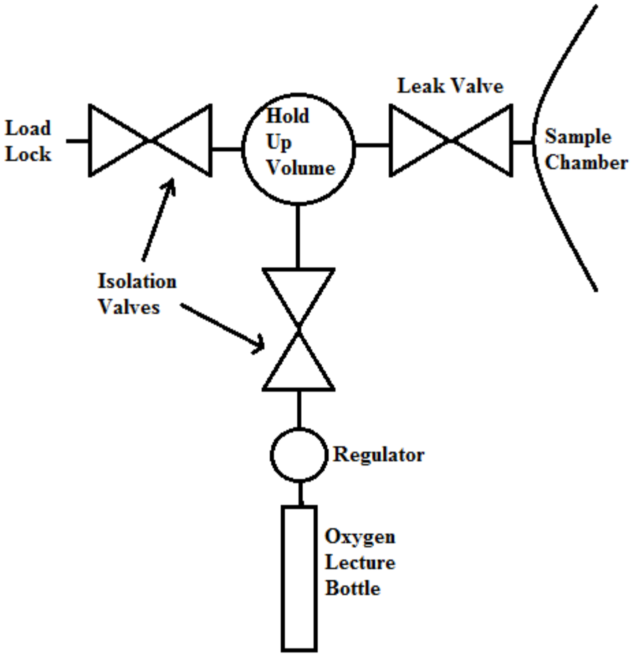

**Figure 9: $O_2$ leak rig.**

turbo and then isolated and refilled with $O_2$ and both isolations were shut.  The $O_2$ remaining in the hold-up line was then adequate to perform several experiments.  The bakeout procedure and line flushing ensured that the level of contaminant gases during the experiments was limited by the specification of the gas in the lecture bottle, which was Matheson Trigas ultra-high purity 99.98% $O_2$ with $H_2O < 5$ ppm, $N_2 < 15$ ppm, and $CO_2 < 1$ ppm.

The leak valve itself operates by varying the compression of a Cu gasket against an optically flat sapphire crystal and was easily able to maintain a leak rate to hold chamber pressure within 1% of a desired setpoint for many minutes without much adjustment.

# Chapter III. Low-Temperature W-$C_{60}$ Surface Interactions

Two different reaction sequences are distinguished in the study of $C_{60}$-W composite material: the first type of experiment began by depositing the W on HOPG followed by the deposition of $C_{60}$. In the second type of experiment the sequence was inverted and $C_{60}$ was deposited first, and was followed by W deposition. The inversion of the deposition sequence leads to significant differences in the final morphology of the thin films, which is driven by modulation of the surface environment the reactants encounter - for example, W adatoms experience a flat graphite surface, where diffusion is nearly unhindered, in one scenario, and a highly corrugated $C_{60}$ island surface in the inverted scenario. The study of the impact of reaction sequence on morphology allows us to draw conclusions on metal-graphite-fullerene interactions.

## Section 3.1: Results

Figure 10a(b) show representative images obtained after a two-step deposition of 0.7 ML (6 ML) W on HOPG at room temperature, followed by the deposition of 0.23 ML (1 ML) $C_{60}$. We will begin with a discussion of the morphology of the W-clusters, followed by an analysis of their size distribution. W, which is deposited on the flat graphite surface, coalesces into agglomerates composed of smaller sub-clusters on top of the HOPG substrate. W does not interact strongly with graphite and has a very high cohesive energy which favors the Vollmer-Weber growth mode, which is indeed commonly observed for transition metals on graphite[65–70]. Imaging was generally challenging, and a stable image could only be obtained with tunneling currents of 50 pA or less, although even with a current this low the tip scan frequently triggered motion of clusters and agglomerates. This effect has been reported also for Mo on graphite [71] and can be attributed to the small adhesion forces between clusters and surface. The tip-induced motion of the agglomerates prevents the measurement of the sub-cluster distributions for low W coverages.

The agglomeration clusters on the 6 ML W (0.7 ML W) surface were >4 nm (4-8 nm) in diameter with an average value of 5.6 nm for the 0.7 ML deposition, and 1.5-3 nm (1.0-2.8 nm) in height with an average value of 2.2 nm (1.9 nm). The average agglomeration cluster diameter could not be determined for the 6 ML deposition due to the presence of very large, irregularly shaped agglomeration clusters up to 100 nm in diameter. Many of these clusters were large enough that they could not be imaged in their entirety. The sub-clusters that make up the agglomeration clusters were approximately spherical in shape and 1-4 nm in diameter when measured at their widest point with a most probable size of 2.5 nm.

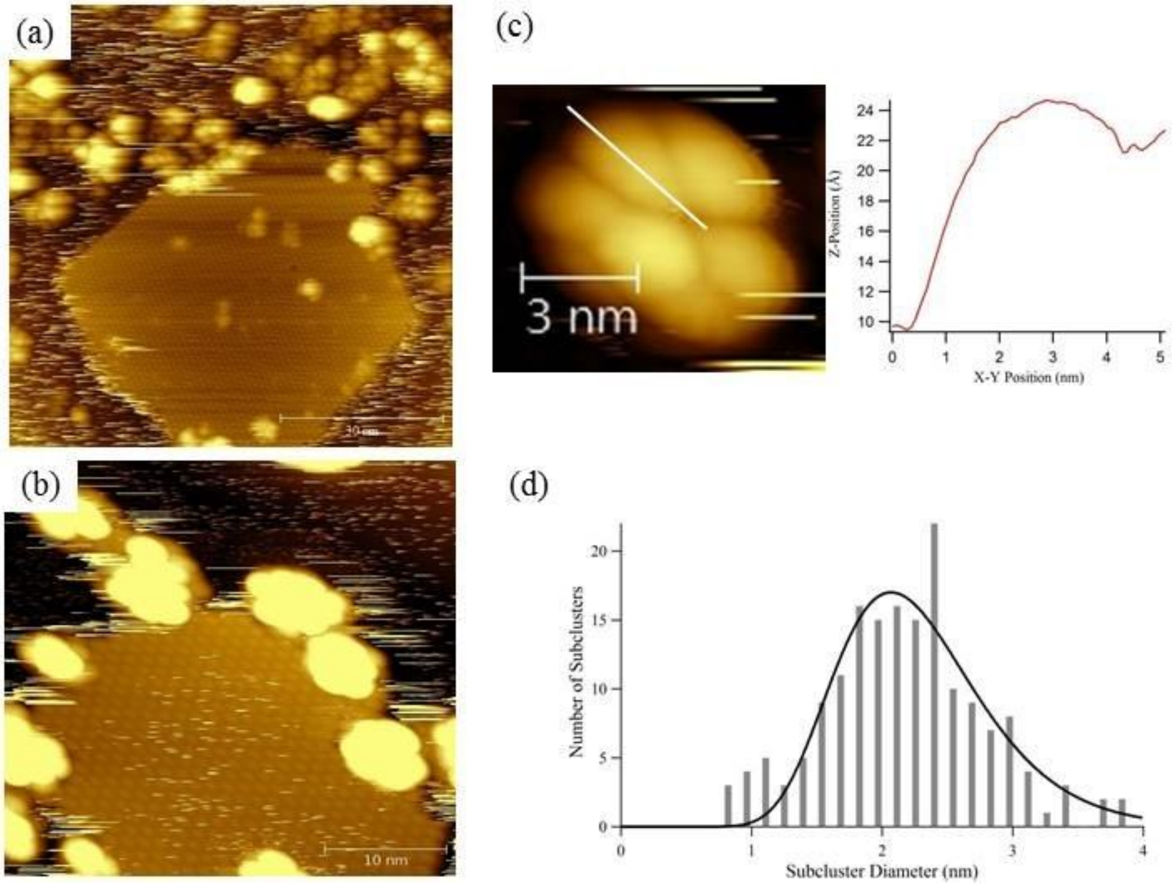

**Figure 10: a) Large $C_{60}$ island formed by deposition of 0.7 ML W followed by 0.23 ML $C_{60}$. ($V_b$ = -1.95 V, I = 0.006 nA) b) 6 ML W followed by 1 ML $C_{60}$. Image contrast was chosen to emphasize features of the $C_{60}$ island rather than the surrounding clusters. Corralling of $C_{60}$ by W clusters evident here. ($V_b$ = 2.00 V, I = 0.07 nA.) c) Cluster and linescan demonstrates how cluster diameters were determined. Subcluster sizes were only analyzed for the 6 ML W case as individual subclusters could not be fully resolved in 0.7 ML W images. d) Log-Normal distribution of the subclusters observed within agglomeration clusters for 6 ML W on HOPG. Trendline is a Log-Normal fit of the distribution**

A size distribution of the sub-clusters incorporated in the agglomerates was measured to gain more detailed information on the mechanisms, which contribute to their nucleation and growth prior to agglomeration. The formation of the agglomerates is therefore interpreted currently as a two-step process, firstly the nucleation of clusters from W-adatoms, and secondly, nucleation of the agglomerates from mobile clusters.

Figure 10d shows the distribution of the sub-cluster diameters for the 6 ML deposition. The diameter was measured along the longest visible axis, as shown in Figure 10c, for uniformity of measurement. The experimental data are compared to the liquid droplet model, which describes the size distribution of metal clusters obtained by coalescence in the gas phase. This model's assumptions are that growth is achieved by irreversible coalescence, and that any two clusters in the system have equal probability of coalescing. This model predicts that the logarithm of the cluster size distribution will obey a Gaussian distribution (a so called log-normal distribution)[72] and has been successful in explaining distributions of small clusters in a wide range of material systems.[73,74] Figure 10d includes the fit of log-normal distribution to the experimental data which are very well described by a distribution with an average diameter of $\bar{D} = 2.07 \pm 0.05\, nm$ and a standard deviation of $\sigma = 1.29 \pm 0.03\, nm$. The high quality of the fit indicates that the liquid droplet model can be applied to the nucleation and growth of small surface clusters of W. An Ostwald-type ripening process is, on the other hand, represented by a Lifshitz-Slyozov-Wagner (LSW) distribution, which has a shallower slope on the small-cluster side of the distribution's maximum, and is thus clearly distinct from the distributions observed here. The W deposit prior to agglomeration can consequently be described as a 2D gas of ad-atoms and even ad-clusters on the graphite surface. Agglomeration then immobilizes the clusters and removes them effectively from the surface "gas phase".

The maximum observed subcluster diameter seems to be the size where the subclusters agglomerate to form the aggregates. The transition can be explained by the limited mobility of subcluster surface atoms. Although continuing to form spherical drops is nearly always favored thermodynamically barring substrate interaction, the diffusion length of W atoms at the cluster surface is short enough that coalescence becomes kinetically limited at a very small size, relative to most metals, which form spherical clusters on graphite up to much larger diameters before transitioning to more irregular shapes. This is bolstered by the fact that Mo, another metal with a very high cohesive energy, formed similar agglomerations when 100-atom size selected clusters were deposited on graphite.[71]

The next step is the deposition of $C_{60}$ and the corresponding images are shown in Figure 10a,b. The molecules are well-resolved and the formation of large islands is consistent with previous studies.[75,76] For deposition onto graphite alone, $C_{60}$ islands will nucleate preferentially at step edges, or grain boundaries and very rarely on the free terrace due to a large mean free path of several hundred nm.[53]

In the presence of W, the $C_{60}$ islands are frequently bordered by several W agglomerates, and Figure 10b provides a representative example. The W agglomerates surround but are only rarely embedded in $C_{60}$ islands and no $C_{60}$ molecules can be detected on top of W clusters and agglomerates. This indicates a weak interaction between the $C_{60}$ and W clusters, and the W agglomerates do not function as nucleation centers for $C_{60}$ island growth. The 2-D hexagonal $C_{60}$ lattice remains unperturbed at the periphery of W-agglomerates, and the fullerenes maintain their perfect spherical shape indicating free rotation. For some metal surfaces such as Cu(111)[77] the interaction between molecule and metal can freeze molecular rotation and allow for the imaging of individual molecular orbitals (MO). Overall, the W- agglomerates and $C_{60}$ molecules behave more like a non-wetting material combination. The nucleation pattern of the $C_{60}$ islands inside incomplete rings of W agglomerates, is likely due to a geometric constraint: $C_{60}$ molecules have a higher likelihood to be reflected from the boundary of W-agglomerates and thus will remain inside the (incomplete) boundary defined by the W-agglomerates for extended periods of time increasing the pressure of ad-molecules and thus likelihood of $C_{60}$ island nucleation.

The inversion of the deposition sequence, $C_{60}$ deposition followed by W, leads to dramatically different structures from those discussed in the previous paragraph. This sequence where highly mobile metal ad-atoms interact with a $C_{60}$ matrix, mimics also most closely the deposition of contacts on molecular layers in solar cell or molecular electronics assemblies. The analysis of the film structure showed significant differences between W- interaction with a single $C_{60}$ layer on graphite, and the W-interaction with a thicker $C_{60}$ layer. In this results section we will therefore first discuss the multilayer structure, and then address the single-layer material. The remainder of this section discusses two different regions of a single sample where 4ML of $C_{60}$ were deposited onto HOPG held at 150˚ C to preclude the formation of fractal islands above the first ML[75] followed by a deposition of 1 ML of W. Different regions of the sample had different thicknesses of $C_{60}$. The regions where more than a single layer of $C_{60}$ was present will be discussed first.

Figure 11a depicts a multilayer of $C_{60}$, whose thickness was verified by imaging of an adjacent lower terrace of $C_{60}$ (not shown). The surface is characterized by a small W coverage, with cluster diameters of only 1.5-4 nm and heights of 0.3-0.8 nm. The distance between clusters is 1-5 nm, and no agglomerates with sub-cluster structures exits. The small cluster size and consequently higher areal density can be attributed to the reduced mobility of W atoms and clusters on the highly corrugated $C_{60}$ surface, which facilitates cluster nucleation but depresses cluster mobility thus leading to smaller clusters and the absence of cluster agglomerates as compared to HOPG.

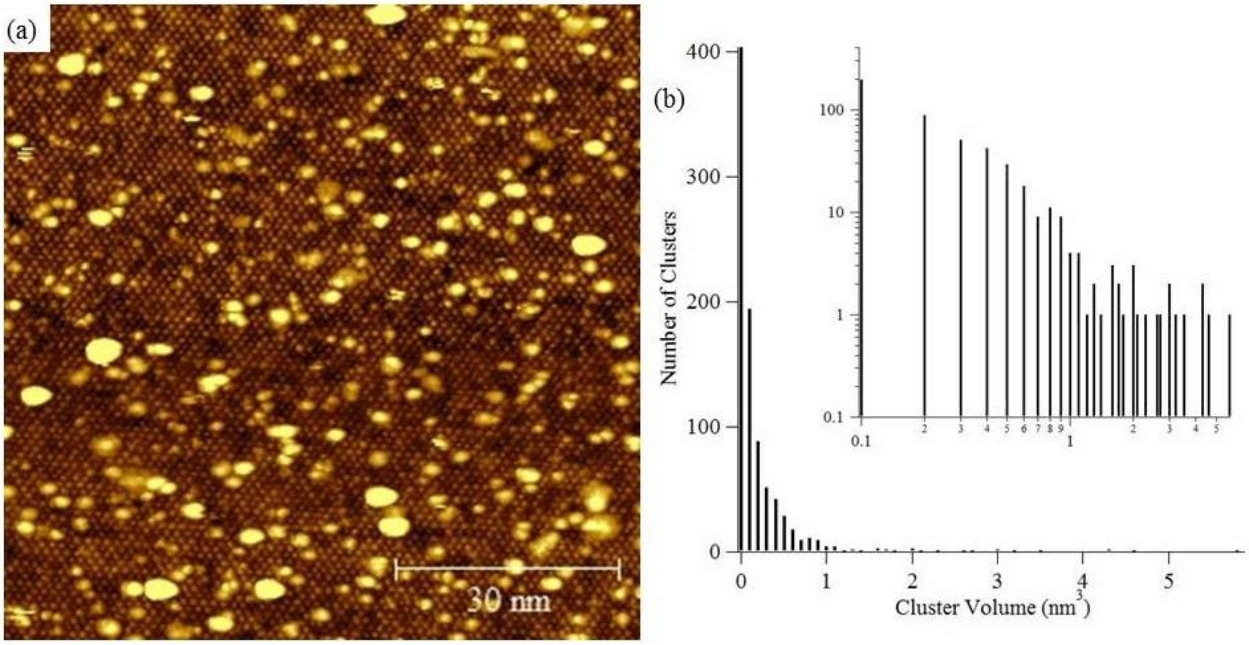

**Figure 11: a) 4 ML $C_{60}$ followed by 1 ML W. Surface composed of small clusters with no sign of W on the surface in between. ($V_b$ = 2.00 V, I = 0.07 nA.) b) Cluster volume distribution of 1 ML W deposited on 4 ML $C_{60}$ surface, inset is a log-log presentation. The behavior is consistent with a model of cluster aggregation incorporating size-dependent diffusivity where there is an initial power law decrease followed by increasing magnitude of the slope on the log-log graph.**

The liquid drop model, which has been used to describe the growth of W clusters on HOPG clearly breaks down for W on $C_{60}$ surfaces. Figure 11b illustrates the distribution of cluster volumes obtained via an image mask from part of the image shown in Figure 11a. A distribution of volumes inferred from measured particle diameters showed identical behavior meaning that the distribution obtained from the mask is valid and does not overrepresent very small clusters by erroneously counting the tops of $C_{60}$ molecules as clusters. The monotonic size decrease is rather unusual. Analogous metallic cluster systems were not found in the literature and this distribution does not adhere to the liquid drop model. Common mechanisms of cluster growth such as Ostwald ripening and the associated LSW distribution, as well as the liquid droplet model produce a peak in the size distribution and not the monotonic decrease seen in Figure 11b.

A possible explanation for this unusual distribution is provided by the analysis of the growth kinetics of particles within colloidal suspensions. A monotonically decreasing distribution is possible with a model of particle aggregation[78] where the particle mobility scales with the volume of the particle raised to some exponent. This allows the mobility to increase or decrease depending on the choice of exponent. Monte-Carlo simulations of such a system in 2-D produces a similar monotonic decreasing distribution to that observed in Figure 11b provided that the exponent is greater than 0, i.e. mobility increases as the particle size increases.

The increasing mobility at small cluster sizes can be rationalized by how very small clusters can sit in the interstice between fullerenes on the surface which is an electronically well-coordinated position. As the clusters grow they sit less deeply in the interstices, are less well-

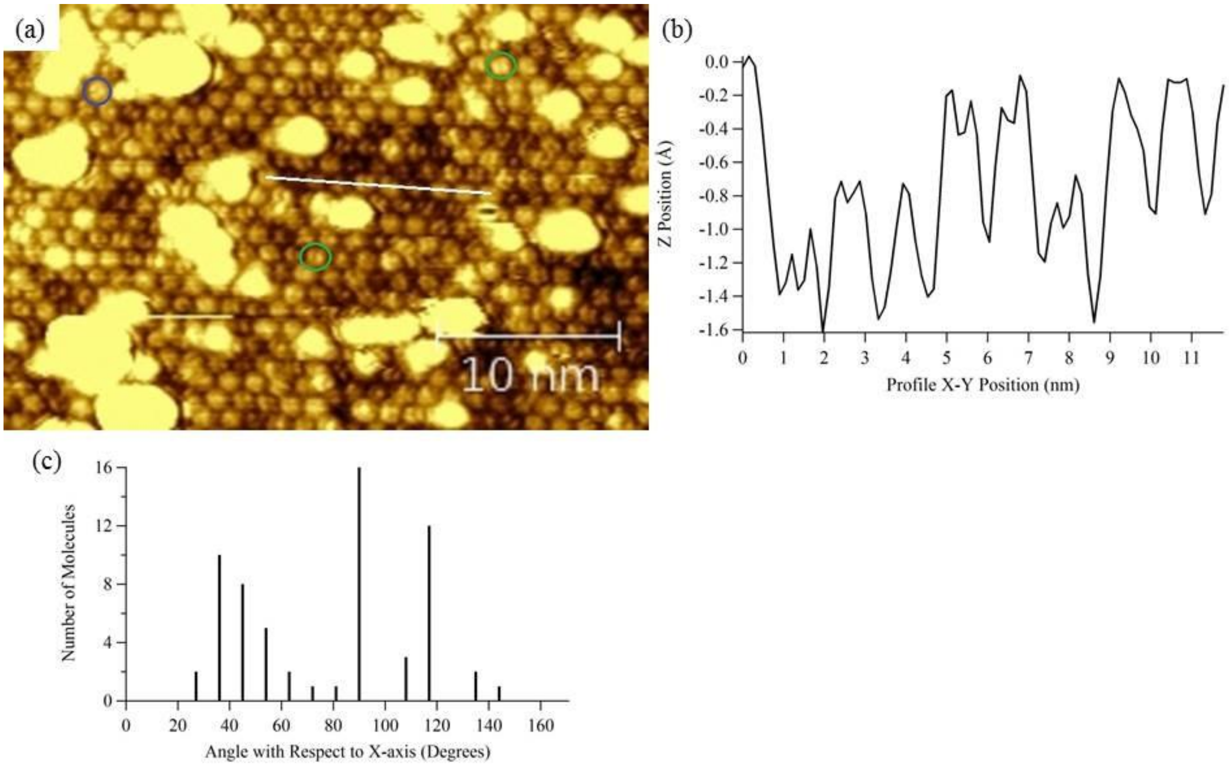

**Figure 12: a) 4 ML $C_{60}$ followed by 1 ML W. The ability to image molecular orbitals indicates that the $C_{60}$ has ceased rotating. There was no correlation of such molecules to the presence of nearby surface clusters, indicating the molecules are interacting with subsurface W . Molecules circled in green have an apex bond separating two hexagon rings (6:6 bond), characterized by a linear bisector; the blue circled molecule has an apex hexagon ring characterized by a division into three sectors of similar area. b) Linescan of white profile line in Figure 3a. Reduced apparent height is observed in many $C_{60}$ with frozen rotation. c) Rotational orientations of apex 6:6 bond molecules. There are preferred orientations but no clear symmetry.**

coordinated, and therefore interact less with the fullerenes. This results in higher mobility. Once the clusters grow large enough, an increase in volume no longer decreases coordination appreciably and so a more conventional regime of decreasing mobility with increasing size will be in place.

The $C_{60}$ layer in between the W clusters now shows structure that was absent before the W deposition. Figure 12a shows a representative image section from within Figure 11a, including a linescan across 10 $C_{60}$ molecules (Figure 12b). This linescan illustrates even more clearly than the image itself, that many of the molecules exhibit a characteristic sub-structure, which is directly related to the molecular orbitals (MO) of the molecule. The sub-structure of the stationary or frozen molecules can be correlated uniquely to their orientation, and lobes of the MOs correspond to the five-membered rings[40]. Bulk $C_{60}$ molecules at room temperature have an estimated rotational period of 9-12 ps[79] and therefore rotate too fast to allow for imaging of individual MOs - the molecules appear as featureless "balls", which can be seen in e.g. Figure 10b. The MOs have been observed at low temperatures when rotation is hindered, or if $C_{60}$ is deposited on a strongly interacting metal surface.

Once W has been deposited, the stationary molecules with visible MO sub-structure amounts to more than 50% of surface molecules and they exhibit different lobe-structures, albeit the structure with a bisector along the molecule centerline and two lobes on either side dominates. This configuration corresponds to the topmost feature being a bond between two carbon atoms which belong to adjacent hexagonal rings[80], henceforth 6:6 bond, which will be reflected in the STM images as two identical lobes, and many of the molecules in Figure 12a show one brighter lobe and a slightly tilted bisector, and therefore correspond to a slightly tilted geometry with an apex atom. A few atoms have a hexagon ring at the apex based on three radial depressions emanating from their apex. However, it is readily apparent that many of the molecules show the MOs, but about half of the molecule sub-structures could not be resolved well enough for categorization of their orientation. Many of the stationary $C_{60}$ molecules also have a reduced apparent height compared to the freely rotating molecules, which is seen in the linescan in Figure 12b.

The spatial distribution of the stationary molecules appears random, and is not correlated to the position of the W-clusters on the surface. Figure 12c shows the distribution of rotational orientations of the fullerenes identified as having a 6:6 bond; calculated by measuring the angle of the bisecting depression with respect to the x-axis. The distribution shows that there are three distinct preferred orientations for the molecules, one at 90°, and two less favored orientations around 40° and 120° with a broader range of angles around 40°. This orientational preference is different from molecule orientations observed in low temperature phases, or for molecules on strongly interacting surfaces.

The appearance of the large percentage of stationary molecules is unequivocally tied to the deposition of W, but not connected to the formation of the W-clusters at the surface. Cessation of rotation can be explained by assuming that W-adatoms diffuse into the $C_{60}$ matrix, adopt interstitial positions, and bond with the molecules thus freezing the rotational motion. W has indeed been shown to form molecular complexes with $C_{60}$, although the ligands investigated in detail are often more complex than isolated $C_{60}$.[81] The presence of several orientations indicates that interstitial W atoms have some freedom in which part of the fullerene it interacts with and the different bonding configurations are energetically close. Our observation strongly indicates the formation of stable intercalation compound with a transition metal, although this configuration has previously been assumed not to be stable. However, these calculations as presented by Wertheim et al.[38] did not take into account the formation of organometallic W-$C_{60}$ complexes, but only considered the cohesive energy of the metal clusters. Our observation shows a competition between surface cluster formation, and intercalation of W in the $C_{60}$ matrix.

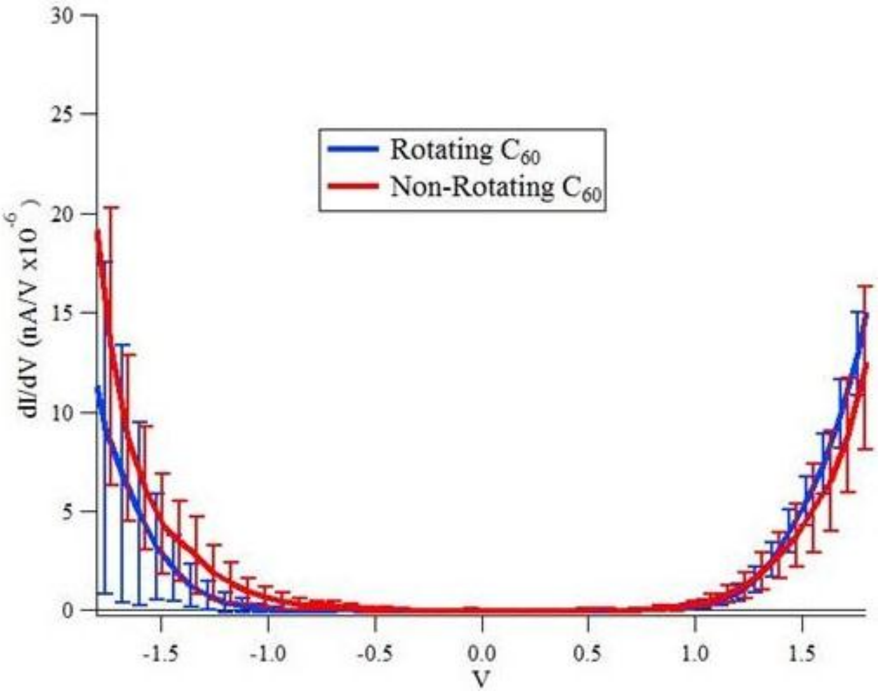

**Figure 13: STS spectra from two regions, one with reduced apparent height and visible MOs and one where the fullerenes are still spinning freely. The traces are an average of many spectra in each region. There is very little difference in the density of states between the two regions. The error bars represent a 95% confidence interval and each resides within the other's error envelope.**

The locations of these reduced apparent height molecules does not correlate with the location of visible surface W; some are several nm's from any cluster while some molecules immediately adjacent to a cluster do not have reduced apparent height. Moreover, all $C_{60}$ with reduced apparent height have visible MOs. This points strongly to interaction with intercalated W with reduced apparent height attributable to a charge transfer to the molecule which is associated with a change in LDOS. The broad extent of this intercalated W suggests that W intercalates into the $C_{60}$ matrix easily at room temperature.

To identify whether these interactions with W have any significant effect on the electronic structure of the $C_{60}$ layer STS was performed over the area of Figure 12a. Figure 13 shows the STS curves for two different areas. One area had obvious apparent height reduction and visible MOs. The other had a topographically unperturbed layer of $C_{60}$ with spinning molecules. As discussed in the introduction, the curves are proportional to the LDOS. Above $E_F$ there are no visible changes. Below $E_F$ however, there is a subtle reduction of the bandgap by up to 0.2 eV. This is further evidence of the interaction between the W and the $C_{60}$, at least in the case where the W is intercalated into the layer.

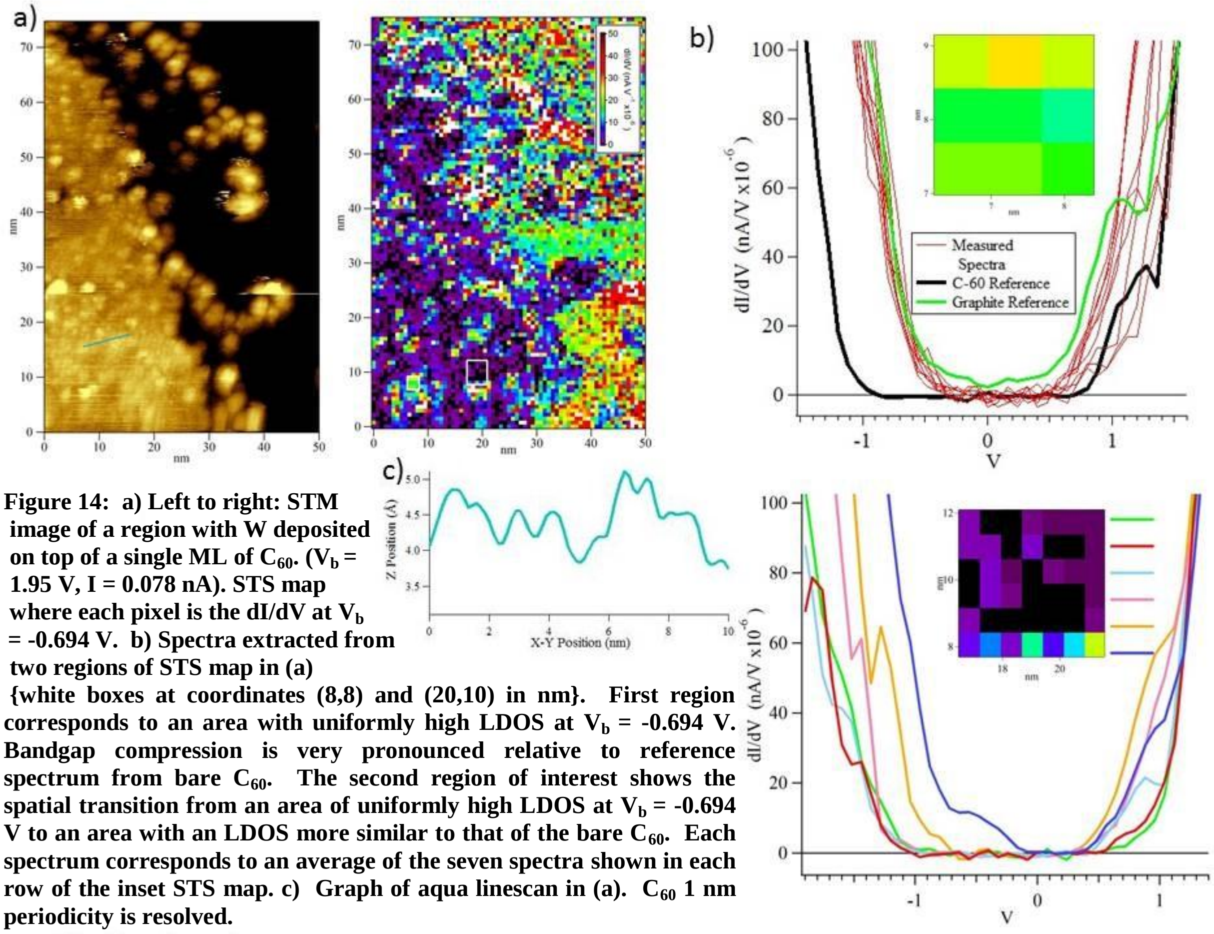

**Figure 14: a) Left to right: STM image of a region with W deposited on top of a single ML of $C_{60}$. ($V_b$ = 1.95 V, I = 0.078 nA). STS map where each pixel is the dI/dV at $V_b$ = -0.694 V. b) Spectra extracted from two regions of STS map in (a) {white boxes at coordinates (8,8) and (20,10) in nm}. First region corresponds to an area with uniformly high LDOS at $V_b$ = -0.694 V. Bandgap compression is very pronounced relative to reference spectrum from bare $C_{60}$. The second region of interest shows the spatial transition from an area of uniformly high LDOS at $V_b$ = -0.694 V to an area with an LDOS more similar to that of the bare $C_{60}$. Each spectrum corresponds to an average of the seven spectra shown in each row of the inset STS map. c) Graph of aqua linescan in (a). $C_{60}$ 1 nm periodicity is resolved.**

The deposition of W onto an area of single ML $C_{60}$ on the same sample caused more significant changes to the morphology of the surface and electronic structure, relative to the areas with more than a single ML of $C_{60}$. Figure 14a depicts one such area. The STM image in Figure 14a is an area of single ML $C_{60}$ adjacent to an area of bare HOPG. On top of the HOPG are what appear to be small W clusters. These clusters are small and linked into chains which are not typical for clusters of this size which normally tend to agglomerate into larger round clusters on bare HOPG. The $C_{60}$ island itself has a very high surface coverage of W that limits the local resolution and prevents the imaging of individual $C_{60}$ molecules at the surface as well as obscured details of the W clusters on top of the island. Within these resolution limitations, clusters of 4-7 nm diameter and up to 1 nm in height above the island surface were observed. Clusters did not decorate the edges of the single ML islands as was observed for the deposition of Au onto $C_{60}$.[35] This, along with the smaller size and denser distribution of surface clusters, is an indication that the W was less mobile atop the $C_{60}$ surface compared to Au.

The STS map in Figure 14a was created by taking a full grid of STS dI/dV data then creating an image where each pixel corresponds to a dI/dV value at a given voltage chosen to maximize contrast between different spectral shapes. In the case of this data, that value was V=-0.694 V. The edge of the $C_{60}$ ML island, which runs from the top left to bottom right corners of the image, is clearly visible in the STS map since the HOPG, a semimetal, has an appreciable LDOS at V= -0.694 V, while the island, which is mainly dominated by $C_{60}$ LDOS, does not. Within the island there is a large degree of inhomogeneity in the LDOS. The source of the inhomogeneity is not obvious from inspection of the STM data for the same region.

The first region of interest is in the lower left-hand corner of the STS map. The spectra from that region are extracted at the lower left-hand corner of the figure. This region has a clearly compressed bandgap, as is evident from comparison to an average of a number of spectra taken on a bare $C_{60}$ ML prior to the W deposition. The reduction of the bandgap comes almost entirely from the occupied states below the $E_F$ with the empty states remaining mostly unperturbed. The total bandgap reduction is ~0.5 eV.

The second region of interest tracks the progression of the change in electronic structure from the highly compressed bandgap region to a region with approximately bulk $C_{60}$ electronic structure. Each displayed curve is an average of the seven individual spectra in the specified row. There is evidently a continuous change between the two states over a distance of 2-3nm.

In the STS map, some of the clusters on the bare HOPG have a similar LDOS to the $C_{60}$ island based on their purple color, e.g. the cluster centered at the coordinates (40 nm,25 nm). This gives a clue as to why these clusters have such an atypical structure compared to W clusters seen on HOPG without $C_{60}$ on the surface. These clusters are actually composed of $C_{60}$ with W interactions holding them together. $C_{60}$ is never imaged on HOPG at room temperature unless the molecule is part of an island at least tens of nm. The ability to image such small islands of $C_{60}$ here is a consequence of interactions with W stabilizing the island enough to be imaged.

Figure 15 is a comparison of the bandgaps on the two surfaces discussed above relative to what is observed on a multilayer of $C_{60}$ in isolation. The measurement of the bandgaps was made by selecting a dI/dV level just above the noise level in the bandgap region and finding the difference between the two voltages where this threshold was crossed. It is clear that there is a reduction of the bandgap of approximately 1 V when W was deposited on the $C_{60}$ monolayer, as discussed above. Within the accuracy of the measurement, the bandgap in $C_{60}$ within the multilayer region is indistinguishable from the bandgap for $C_{60}$ alone on an HOPG surface.

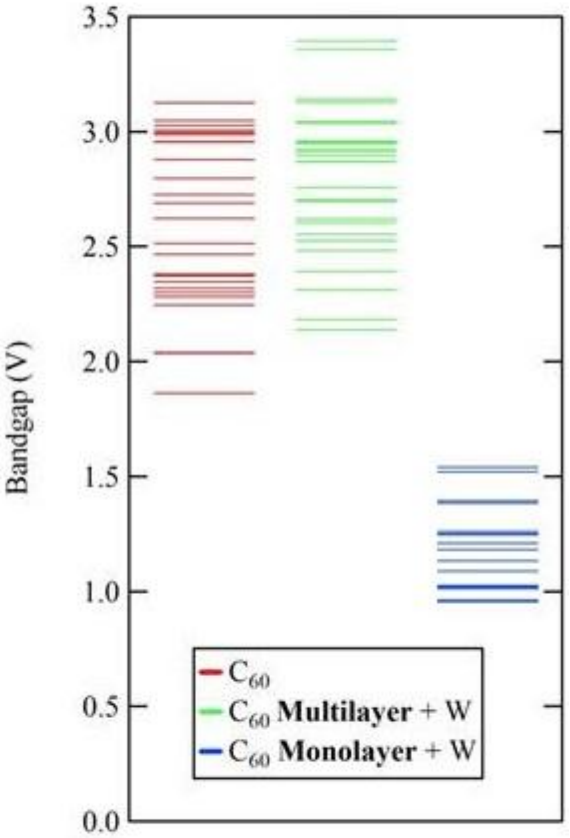

**Figure 15: Measured bandgaps for different surfaces. The bandgaps on the single ML of $C_{60}$ are compressed dramatically. There is a slight but apparent increase in the bandgap for W deposited on a multilayer relative to bare $C_{60}$ that is likely due to noise in the STS spectra since such an increase is inconsistent with our understanding of this (and similar) systems and STS data at room temperature exhibit a significant degree of noise.**

## Section 3.3: Discussion

The compilation of data presented thus far suggests a cohesive model for the behavior of the W/$C_{60}$ system. For W initially deposited on HOPG the extremely high mobility of the W atoms on the surface allows for the coalescence of round clusters only 1-4 nm in diameter which adhere closely to the size distributions predicted by a liquid drop model. These clusters remain mobile and come together to form larger agglomeration clusters. The strong cohesion of the sub-clusters and resulting short diffusion length of surface atoms on the subclusters (W has the highest cohesive energy of all elements) limits the degree to which they can be sintered into the larger agglomeration clusters and so their structure remains visible as lobes on the larger agglomeration clusters. Free W atoms are effectively nonexistent on the HOPG surface after this has taken place, as revealed by the lack of streaks in the STM images over the substrate, which are seen when an STM tip interacts with mobile atoms. This lends strong support to the model presented where the agglomeration clusters are formed in a two-step process requiring the subclusters to be formed prior to the agglomerations.

Subsequent deposition of $C_{60}$ leads to mobile $C_{60}$ on the HOPG substrate. These $C_{60}$ molecules interact very weakly with the W clusters as their only effect on the final formation of the $C_{60}$ islands is a corralling effect whereby W clusters confine $C_{60}$ long enough for the nucleation of islands to occur. The clusters themselves do not function as nucleation centers for the $C_{60}$ islands. This result is strange in light of a previous study of $C_{60}$ on a W(100) single crystal studied by XPS which showed significant charge transfer from the W into the adjacent $C_{60}$.[38] One could reasonably expect that such an interaction would manifest itself in a detailed STM study of such a similar system.

This set of results stands in contrast to the reverse sequence of deposition. When $C_{60}$ is deposited first on HOPG it follows the well-understood behavior of nucleating into large round islands of a hexagonal 2-D lattice followed by similar islands on top to form an FCC(111) lattice normal to the surface. The subsequent deposition of W leads to strong interactions with the $C_{60}$ layer. This is clear from the observation of large areas of the surface with frozen $C_{60}$ rotation, reduced apparent height, and perturbation of the DOS near $E_F$. It is clear from imaging of W on multiple ML $C_{60}$ that W intercalates into the $C_{60}$ matrix rather easily since areas with these effects occur far from surface clusters so these visible clusters cannot be causing the effect. This intercalation stands in apparent contrast to an XPS study of $C_{60}$ deposited onto W(100) and heated where intercalation was not observed and a phenomenological model was introduced to predict whether intercalation into $C_{60}$ would occur for any metal based on the metal's cohesive energy.[38] This model successfully predicted the intercalation behavior of nearly all metals for which data was available, and strongly indicated W would not intercalate. This prediction is certainly true when the W atoms must first escape the surface of a finite amount of W before intercalating, but in the current investigation, it is extremely likely that the W atoms intercalate before interacting with other W atoms on the surface.

For W deposited onto a single ML of $C_{60}$, the modifications to electronic structure are much more profound than on a multilayer. Bandgaps are reduced almost to the point of making the surface metallic, and indeed the surface coverage of W in these areas is visibly high enough that STS could be starting to image the LDOS of the surface W in isolated areas. The high surface coverage of W on the single ML $C_{60}$ provides additional support for the ease with which W intercalates into $C_{60}$ since there is limited vertical extent here for the $C_{60}$ to intercalate and so more of it must necessarily remain on the surface.

The strong interaction between the W and the $C_{60}$ for this sequence of deposition can likely be explained through a charge donation from the W to the $C_{60}$ and possible image charge effects just as it was for $C_{60}$ on Au and Ag single crystals,[40,41] semiconducting carbon nanotubes on Au,[82] and indeed for $C_{60}$ on W as well.[38,83] Why the larger W clusters do not interact with adjacent $C_{60}$ in any obvious way is more of an enigma as their situation is analogous to the $C_{60}$ on top of single crystal surfaces which have in the past shown very strong interaction in X-ray Photoemission and Auger Electron Spectroscopy studies.[38,83] It is not at all clear why the interaction should be significantly less for clusters when compared to a single crystal. The fact that single atoms or very small clusters of only a few atoms of W would interact more strongly with $C_{60}$ makes intuitive sense as isolated W atoms will be looking for bonding situations to fill their valence orbitals. W atoms at the surface of a large W cluster are able to satisfy more of this requirement and so would be less prone to react.

# Chapter IV. Annealing of $C_{60}$ on W and the Formation of Nanospheres

In this section, a novel nanostructure will be introduced which was synthesized by annealing $C_{60}$ on layers of W with an MgO(100) substrate. At this point, it's instructive to review the kinds of interactions that have been observed when $C_{60}$ is deposited on and annealed on transition metal surfaces.

Charge transfer from the metal to the $C_{60}$ LUMO has been reported for Au(110), polycrystalline Ag, Ni(110),[31] Ag(111),[84] Cu(100), Cu(110), Cu(111),[85] and of course W.[38] Pt(111) has been reported to form covalent bonds due to its large work function and the lack of evidence for charge transfer in vibrational spectra; this despite a strong interaction characterized by perturbations to the electronic structure of both substrate and $C_{60}$.[32] The charge transfer has been explained in most cases as the result of work function mismatch between the metal surface and $C_{60}$ which allows electrons to reduce their energy by moving from the metal's $E_F$ into the $C_{60}$ LUMO. This explanation can be too simple, however, since the degree of charge transfer is not inversely proportional to the metal work function, as this explanation would suggest.

In all cases, when an anneal above 200˚C is applied, all but the 1st ML of $C_{60}$ are removed through sublimation. For the 1st ML, desorption has never been observed on any metal except for Ag, where desorption was inferred at 375˚C.[84] If very high temperatures are applied to an adsorbed ML, dissolution of the ML into graphite or carbide is observed.[32,34,83]

## Section 4.1 Experimental Details

The depositions of W (and subsequently $C_{60}$) were conducted onto MgO(100) substrates that were prepared in accordance with Section 2.2 and affixed to Mo sample plates with spot welded Ta strips. Silver epoxy was applied from the substrate, up a vertical side of the substrate and extended to a corner of the top of the sample to ensure that a conductive path was available from the deposited metallic thin film to the sample plate. This was necessary to allow STM characterization of the sample. The MgO substrates were preannealed in UHV overnight at 200˚C to desorb any surface contaminants. MgO is stable against reduction for all temperatures probed in this thesis at laboratory UHV oxygen partial pressures. The substrates were then heated to 600˚C and ~50 nm of W were deposited at a deposition rate of 2.7-2.9 nm/min. This temperature was chosen because it had previously been shown the W grows epitaxially on MgO(100) above 400˚C.[47] After the deposition was completed, the substrates were annealed 10 min to promote surface diffusion to create a flatter surface for imaging.

These W films were then cooled and characterized with STM before a room temperature deposition of ~4 ML of $C_{60}$ was performed. Several ML of $C_{60}$ were deposited to ensure complete coverage of the surface and because it was known that a low temperature anneal would be sufficient to desorb all but the 1st ML. This multi-layer deposition was then characterized with STM. The samples were then annealed at either 400 or 500˚C for 20 min. After cooldown the samples were characterized in detail by STM/STS. The sample annealed at 500˚C was then oxidized for 20 min at 300˚C and $1x10^{-7}$ mbar $O_2$ partial pressure and recharacterized by STM/STS.

## Section 4.2 The Tungsten Thin Film

The best imaging conditions for the W surfaces was found to be <0.1 V and >0.5 nA. The W films were characterized by some non-uniformity of morphology at large scales (50-500 nm); there were regions containing cubic structures with straight terrace edges interspersed with regions lacking long range structure within 1 mm of each other on the same sample as shown in Figure 16. The most likely explanation for this non-uniformity is temperature gradients across

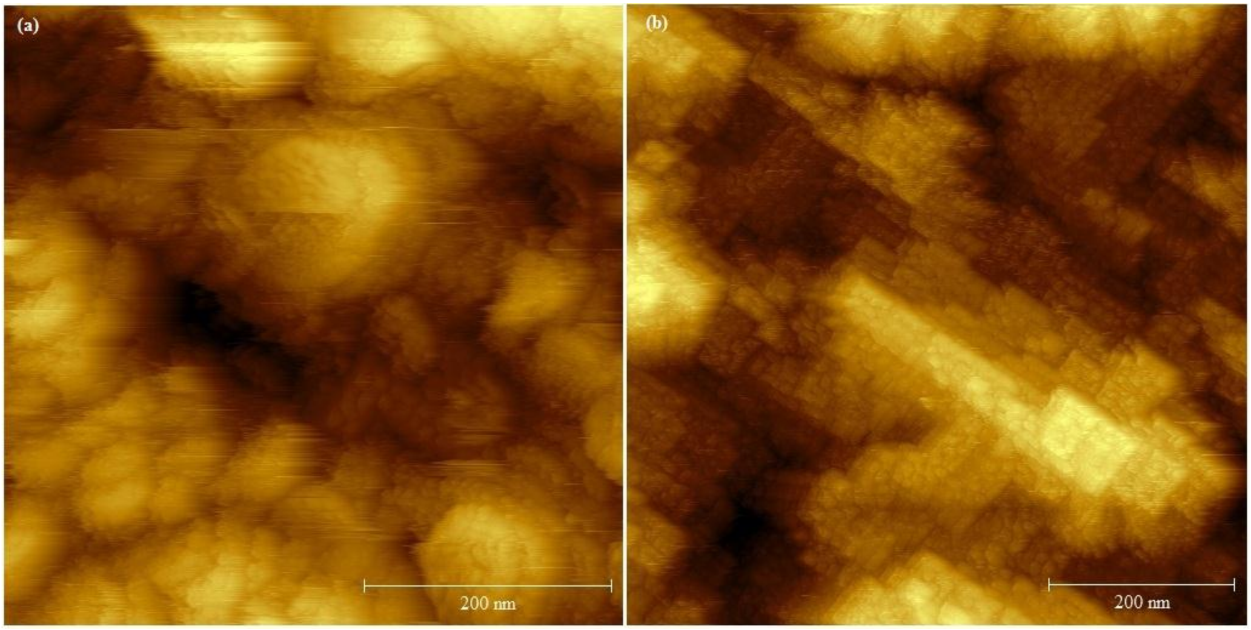

**Figure 16: a) 250 mV, 1 nA b) 6 mV, 0.66 nA. Note the significant differences in morphology at different points on same sample.**

the sample. Thermal contact was only established by the pressure from the spot-welded Ta strips so there were likely only a few contact points between substrate and sample plate, thereby leading to thermal non-uniformity at the substrate surface. For later samples, the entire bottom surface was coated with Ag glue to improve thermal contact between the MgO and sample plate. Homogeneity of surface features was generally good for these later samples.

The presence of the cubic terraces is an indication of epitaxy with the cubic MgO substrate. All cubic features have edges that point in one of two directions, regardless of where on the sample surface they were imaged. This is really only plausible if the W crystallites adopt a set orientation defined by the substrate crystallography. The W thin film does not follow the step structure or island shape of the MgO substrate (Figure 3), and the cubic structure and straight terrace edges are therefore not an imprint of the MgO substrate topography but can indeed be attributed to epitaxy.

This epitaxy is not entirely unexpected, as magnetron sputtered W has been shown to grow epitaxially on MgO.[47] Additionally, MgO(100) accommodates epitaxy for numerous metals, both BCC and FCC, including but not limited to Fe[86], Ni, Cu, Pd, Pt, and Pb.[87]

On a smaller length scale, the morphology is composed of small irregularly shaped protrusions from the film of 3-10 nm in diameter and less than 1 nm in height. Figure 17 is a representative region. Steps across a terrace edge were 0.5-2 nm in height but also several nm in width (more slope than step) so the terrace edges were not well defined.

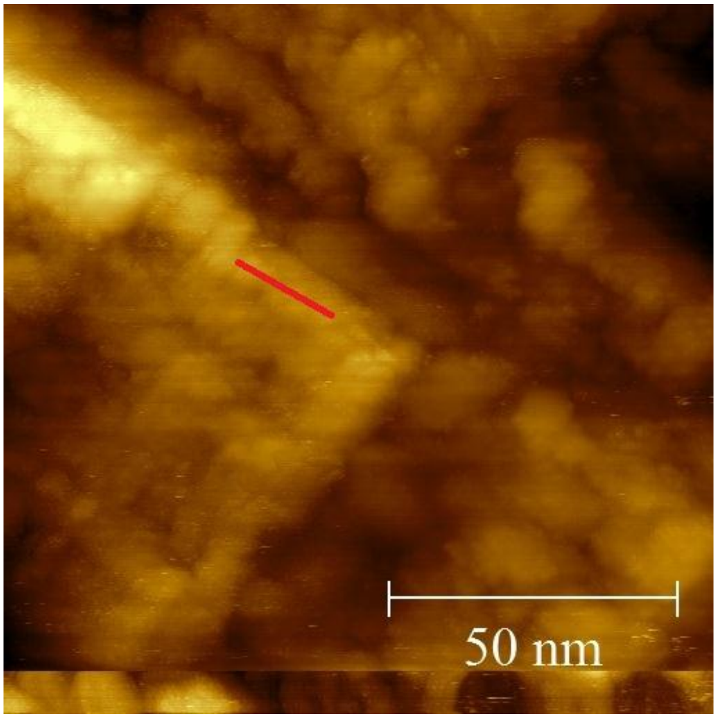

**Figure 17: 50 nm W film on MgO(100) deposited at 600˚C. See Figure 19 for profile of red linescan.**

The mobility of surface atoms is small enough at these temperatures that surface atoms do not diffuse far enough to create a flat surface structure. This conclusion is bolstered by images from a separate deposition performed with the substrate surface held at 800˚C. As can be seen in Figure 19, the surface in this case organizes into a series of flat terraces with a surface roughness much lower than any region observed in the 600˚C depositions. Also, edges of the terraces are curved and do not retain any of the 90˚ corners that were visible in the 600˚C depositions. The change in roughness and island shape can be attributed to an increase in surface adatom mobility, and is kinetically driven. However, we currently lack sufficient data to draw more extensive conclusions on activation barriers and growth kinetics.

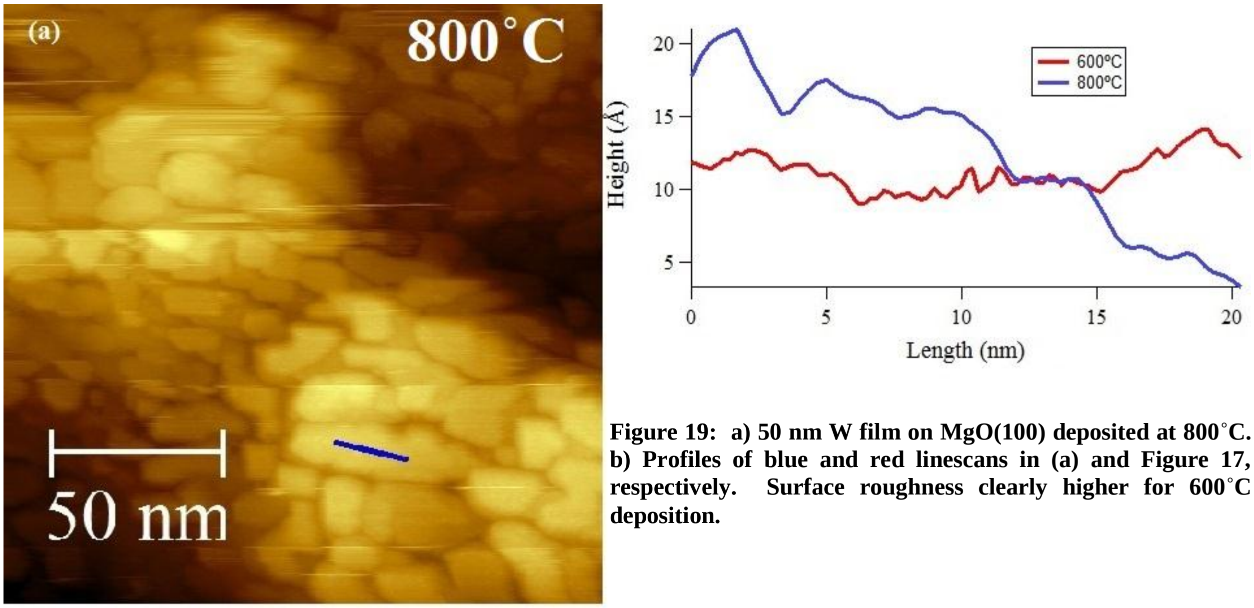

**Figure 19: a) 50 nm W film on MgO(100) deposited at 800˚C. b) Profiles of blue and red linescans in (a) and Figure 17, respectively. Surface roughness clearly higher for 600˚C deposition.**

At higher magnification, a new type of structure emerges on the film deposited at 600˚C.

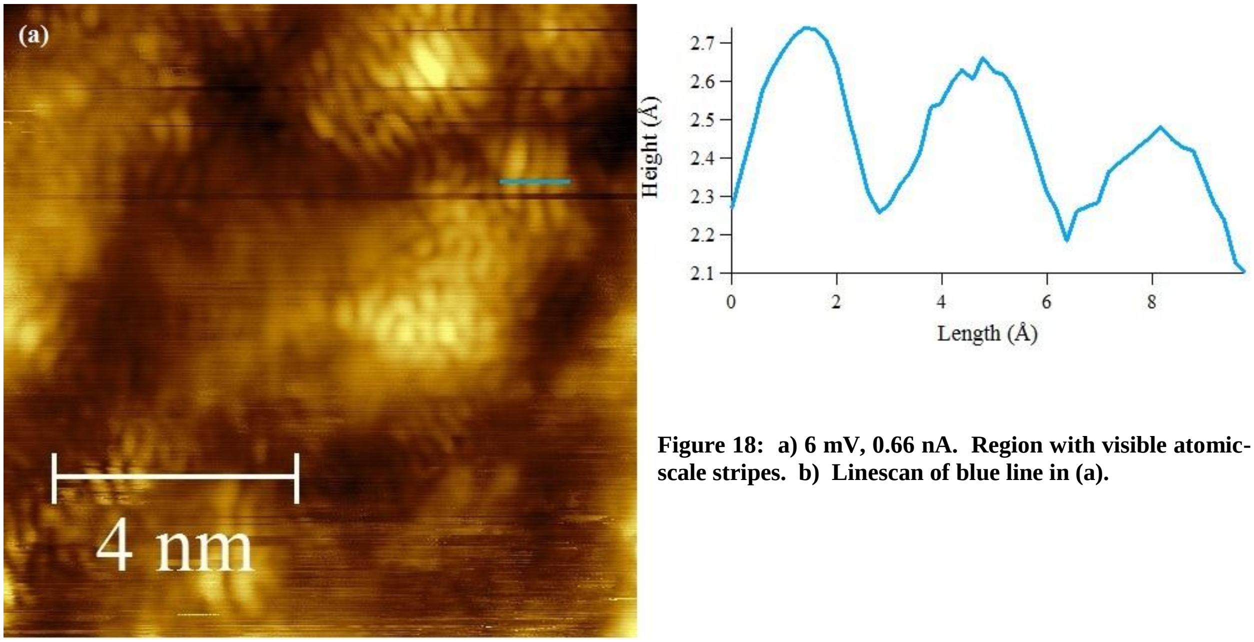

**Figure 18: a) 6 mV, 0.66 nA. Region with visible atomic-scale stripes. b) Linescan of blue line in (a).**

As can be seen in Figure 18, parallel stripes emerge if appropriate low voltage, high current imaging conditions are chosen. The stripes are ~3 Å apart with a corrugation of about 0.4 Å, peak to valley. This structure on W has not been reported in the past. The stripe periodicity is close to BCC W's lattice constant of 3.16 Å, but does not show the preferred orientations implied by epitaxy with the cubic substrate. W(100) is known to reconstruct into a similar p(2x1) structure due to oxygen adsorption[88], but its periodicity is closer to 6 Å in that reconstruction. The stripes are also clearly perpendicular to each other in the p(2x1) reconstruction as there are two equivalent orientations {p(2x1) and p(1x2)}, whereas that effect is not seen here. Other adsorbate-induced reconstructions on W have been found for C and H as well,[88,89] but do not closely resemble the striped domains of Figure 18.

The origin of the stripes has not been conclusively resolved. If epitaxy to the MgO is assumed, any true reconstruction would need to adopt some set orientation or set of orientations with a fixed relationship to the underlying substrate lattice. Instead, the stripes occupy a large number of orientations in the X-Y plane. It was argued recently that stripes in the STM images of round nanoparticles can be attributed to an imaging artifact,[90,91] but in that case the spherical nanoparticles were greater than 5 nm in height and the stripes were all oriented perpendicular to the tip scanning direction, which was a characteristic of that artifact. Both of those criteria are not met, so that type of artifact is unlikely to be what is imaged here.

Alternatively, the striped regions might be caused by the differentiation of nanocrystalline domains.

## Section 4.3 $C_{60}$ on W/MgO(100)

The $C_{60}$ covered surface proved challenging to image since the STM tip often moves or picks up $C_{60}$ molecules under the best of circumstances since the molecules do not interact strongly with each other or, oftentimes, the substrate. Relatively high bias voltages (>1.5 V) must also be used since $C_{60}$ is a wide bandgap semiconductor and thus lacks states to tunnel into at low bias voltages.

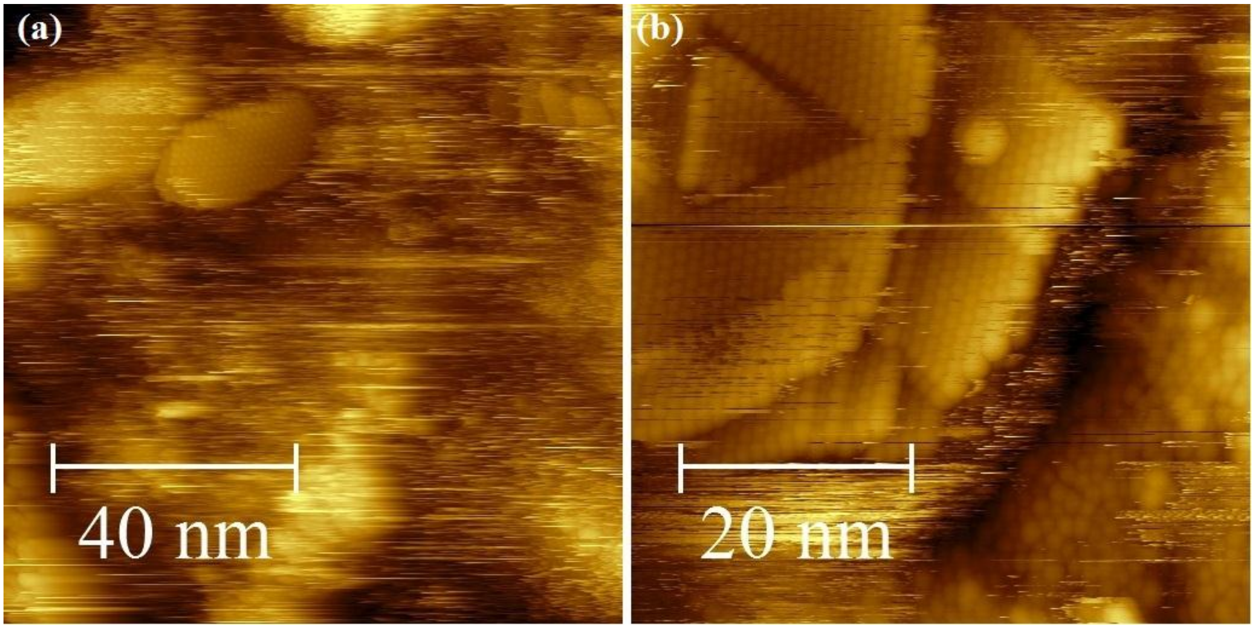

**Figure 20: 2.0 V, 0.07 nA Two images of 4 ML $C_{60}$ on W/MgO(100). Large fractions of the surface are obscured by tip-induced motion of the $C_{60}$ molecules. Note the two different types of surface ordering in (b), the top left shows FCC(111) ordering whereas at bottom right $C_{60}$ adopts an amorphous surface arrangement.**

Figure 20 shows two images from a deposition of 4 ML $C_{60}$ on W/MgO(100) and two different surface arrangements of $C_{60}$ can be distinguished in Figure 20b. The first orientation was a densely packed layer corresponding to an FCC(111) plane, similar to what was observed earlier for $C_{60}$ on HOPG (e.g. Figure 10b). This configuration is evident in Figure 20a,b.

The second configuration was an amorphous surface arrangement with many molecules displaying an increased apparent size, as in the lower right-hand corner of Figure 20b. Curvature effects cannot explain the presence of the disordered phase since the curvature in the two regions is similar. Instead, it's possible that surface roughness and the presence of a high density of defects which pin the individual molecules creates the necessary conditions. A similar disordered arrangement has been observed for $C_{60}$ deposited on heavily ion-damaged graphite surfaces.[92]

## Section 4.4 Anneal of $C_{60}$ on W/MgO(100) - Generation of Nanospheres

As described in the previous section, the 4 ML $C_{60}$ on W/MgO(100) were annealed to 400 or 500˚C for 20 minutes to desorb all but the first layer of $C_{60}$ and to induce a reaction with the underlying W.

The resulting surface morphologies were similar for both annealing temperatures and the surface morphology is dominated by small spherical particles, subsequently termed "nanospheres." The coverage of the surface is quite high (>90%) but regions are observed where no nanospheres were observed (e.g. Figure 21b).

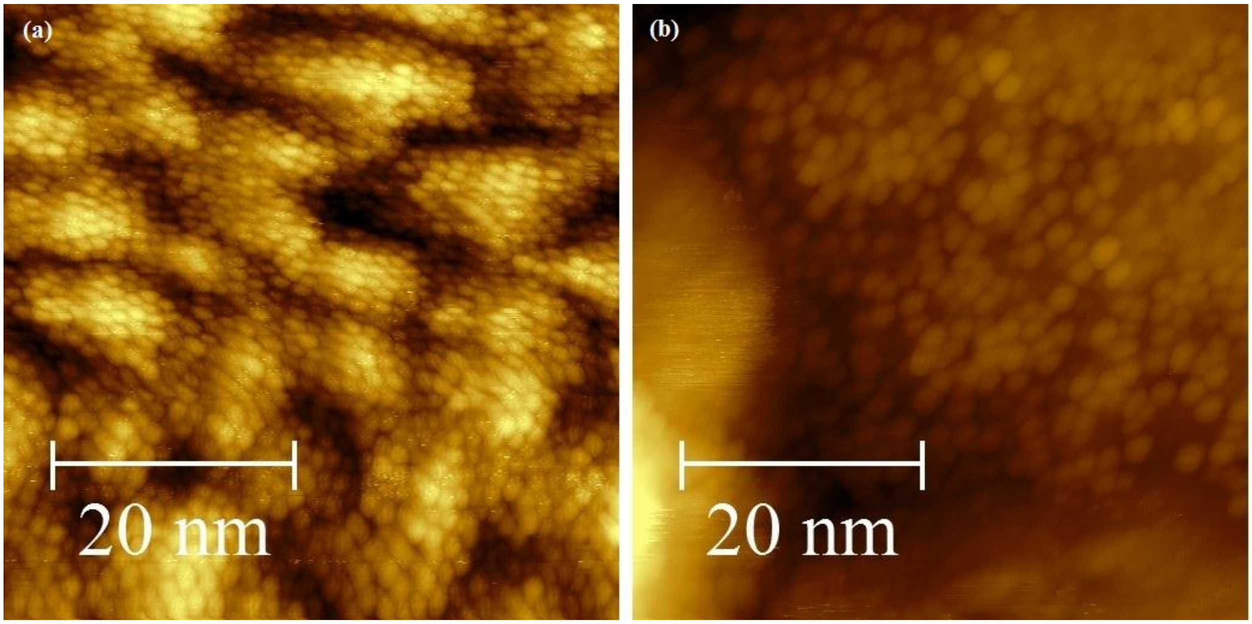

**Figure 21: (a) 0.1 V, 0.66 nA (b) 1.0 V, 1.5 nA. $C_{60}$ on W/MgO(100) after (a) 400 or (b) 500˚C anneal. Surfaces are covered by nanospheres with a few bare areas like left side of (b). (a) shows some distortion due to thermal drift.**

The nanospheres are fully metallic. This was evident initially when the spheres could be easily imaged with gap voltages as low as 0.1 V. STS also provides clear proof that the $C_{60}$ bandgap has fully disappeared, as can be seen in Figure 22c,d, which are the regions (marked 1 and 2) of the STS map in Figure 22b that have the lowest and highest LDOS at zero bias, respectively. From Figure 22c,d, it is seen that the spectra are nearly featureless parabolas, similar to spectra taken from bare W. From these spectra alone, it is not possible to differentiate whether the surface is composed of W or WC.

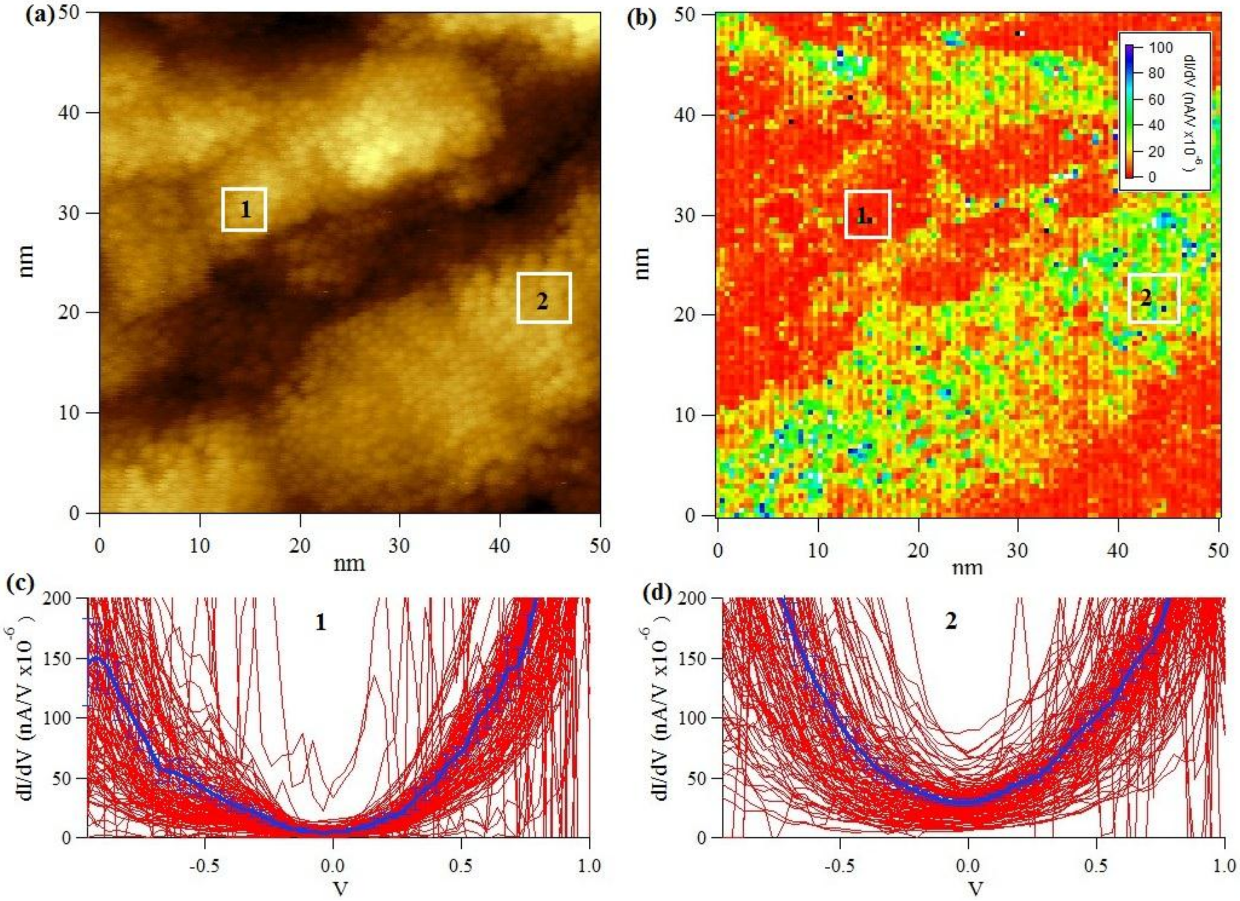

**Figure 22: (a) 1 V, 1.2 nA. Image of region fully covered with nanospheres. Image captured simultaneously with spectral map. (b) Spectral map of dI/dV values at $E_F$. Colorscale chosen to maximize contrast but spectra are very similar throughout image. (c) and (d) Spectra captured within areas 1 and 2, respectively. Spectra show metallicity everywhere with no spectral features similar to the preanneal $C_{60}$ spectra.**

The most significant, but small, difference in the dI/dV curves between the representative regions 1 and 2 is the magnitude of dI/dV at $E_F$, which can be related to the LDOS. The topography in these two regions in identical. The origin of the relatively subtle differences in

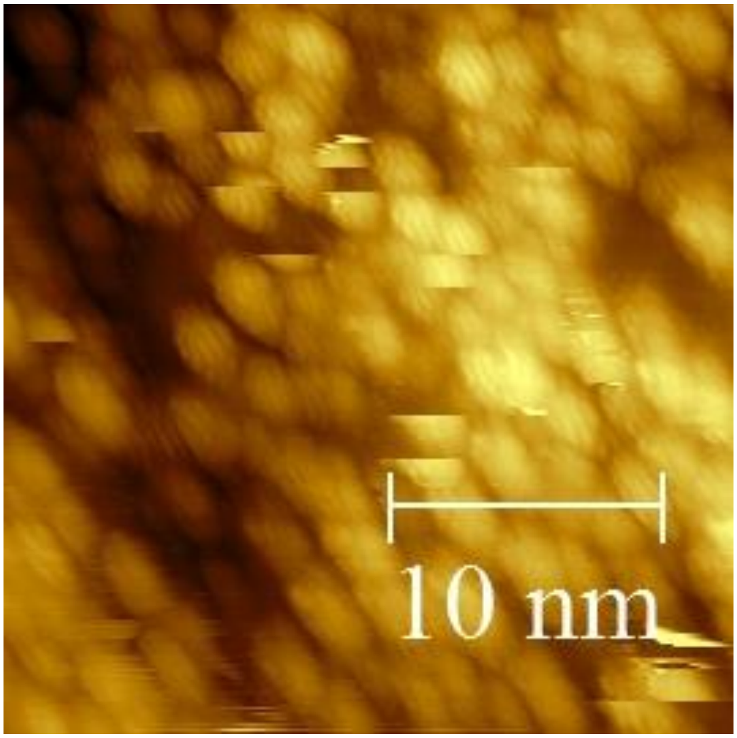

**Figure 24: 1 V, 0.1 nA. Nanospheres with evidence of at least one mobile nanosphere.**

dI/dV curves is currently unclear, but likely attributable to subtle differences in the reaction between W and $C_{60}$.

Some nanospheres are actually mobile under the influence of the tip. This can be seen in Figure 24 where several nanospheres appear to be cut in half. This occurs when the tip images part of a stationary nanosphere that then moves before it can be imaged fully. This is intriguing since, presumably, the very high W cohesive energy would prevent a nanosphere from moving under the tip's influence if it remains strongly bonded to the W film. Serendipitously, the mobile nanospheres provided an excellent opportunity to measure the heights of the nanospheres by taking line scans across the plane where the sphere appears to be cut in half. For the 500˚C annealed sample, nanspheres were measured to be 5-8 Å in height from 13 examples in three images. For the 400˚C annealed sample, no mobile nanospheres were observed, which may indicate that bonding to the film decreases with increasing annealing temperature. The 13 examples cited could involve multiple counting of the same nanospheres. Once a nanospheres is released from the surface, it's quite possible that it follows the tip and is redeposited somewhere else in the image, only to be imaged again. This occurred multiple times while imaging small W clusters on graphite.

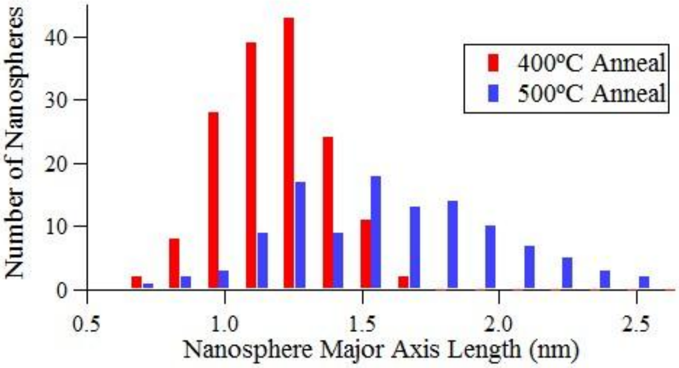

**Figure 23: Histogram of nanosphere major axis lengths. Increasing annealing temperatures correspond to greater deformation of the original $C_{60}$ cage structure. The apparent diameter of $C_{60}$ in a close packed lattice is uniformly 1.0 nm.**

The measured heights indicate that the original $C_{60}$ shell is significantly compressed in height by the anneal. This distortion is consistent with the measurements of the nanospheres' major axis lengths. Figure 23 shows that as annealing temperature is increased from 400 to 500˚C, the length of the longest in-plane axis increases in tandem. With the observation that the height of the spheres after the 500˚C anneal decreases significantly relative to the pre-anneal fullerene cage, it is most likely that the dimensional change is due to deformation of the nanosphere structure rather than the addition of significant material from the W film. The major axis length measurements could be affected by sample drift, which would tend to add length to each measurement, but these measurements were a taken after running the microscope for a sufficient period of time to reach the instrument steady state drift, which we have measured to be approximately 1 nm/min. This could add up to 5 Å to the measurement assuming it takes 30 sec to image a single nanosphere in a 20x20 nm$^2$ image (a conservative estimate).

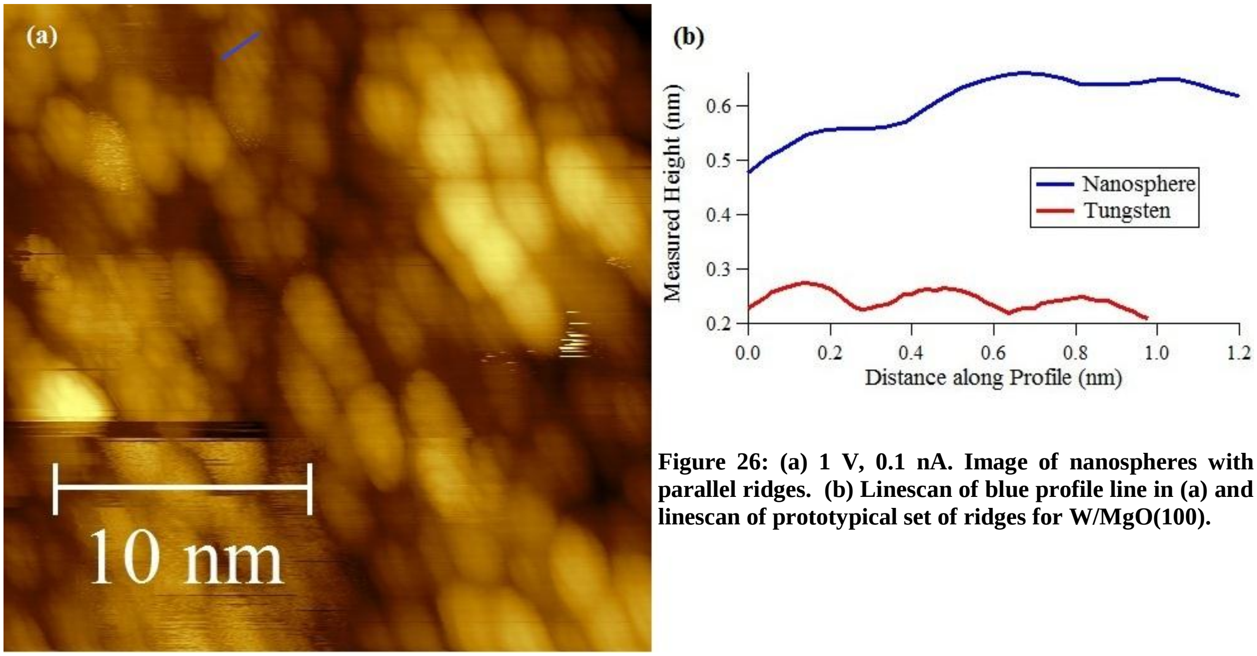

**Figure 26: (a) 1 V, 0.1 nA. Image of nanospheres with parallel ridges. (b) Linescan of blue profile line in (a) and linescan of prototypical set of ridges for W/MgO(100).**

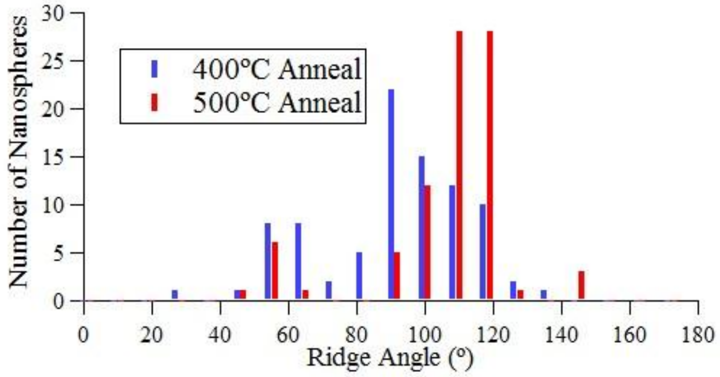

**Figure 25: Angle of ridges on tops of nanospheres, countercloskwise from +X-axis of image. The vast majority of ridges within ±40˚ of +Y-axis.**

The nanospheres themselves do not have a perfectly smooth surface but show ridges. Figure 26 shows an area where these ridges are clearly visible, and they are reminiscent of ones that were observed on the W/MgO(100) surface (Figure 18a). The ridges on the nanospheres are about 4 Å apart with a peak-to-valley corrugation of about 0.25 Å. The ridges on the W surface are deeper and narrower, indicative of a different surface structure/termination.

About 50% of the spheres exhibit ridges. Of those, Figure 25 shows that a majority are oriented within 40˚ of the y-axis. The origin of the orientational preference of ridges remains unresolved, but is likely connected to an imaging feature. It is, in general, easier to resolve ridges perpendicular to the piezo fast scan direction (±X in all images presented) than ridges which are parallel. We will resolve this question in a future simulation of imaging traces as a function of surface corrugation.

It was observed that the different orientations are not uniformly distributed throughout an image, rather if a particular orientation was observed in a nanosphere, all nearby nanospheres would have a similar, if not identical, orientation, as shown in Figure 27. Only a few images had enough nanospheres with the ridges resolved to determine the angular distribution of their orientations, and in these images orientations counterclockwise of the y-axis covered large areas, with smaller groups of nanospheres showing other orientations. While imaging direction is likely to introduce a bias into the orientational distribution, it is probably not the only factor driving the ridge orientations.

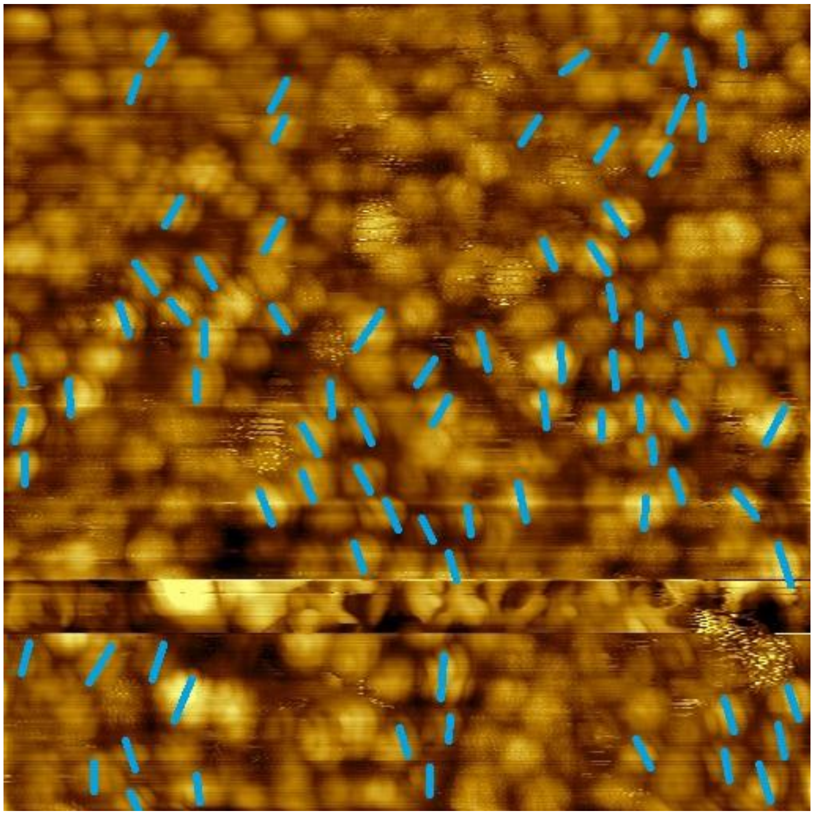

**Figure 27: Ridge orientation showing how similar orientation tend to be in close proximity to each other.**

## Section 4.5 Oxidation of Annealed $C_{60}$ on W/MgO(100)

The next step in this investigation is concerned with the oxidation characteristics of the nanospheres as examples of a unique nanostructure that are likely terminated by W atoms in a carbide bonding configuration. The 500˚C annealed surface was exposed to $1\text{x}10^{-7}$ mbar of $O_2$ for 20 min at 300˚C for a total dose of $3.3\text{x}10^{16}$ $O_2/\text{cm}^2$.

Prior to the oxidation step, the sample was left under UHV of ~$4\text{x}10^{-10}$ mbar overnight (18 hours elapsed since annealing to form the nanospheres). This exposure alone led to noticeable changes to the electronic structure in some of the nanosphere covered region, and can be seen in a comparison of Figure 22c,d and Figure 28d. These changes indicate that oxidation

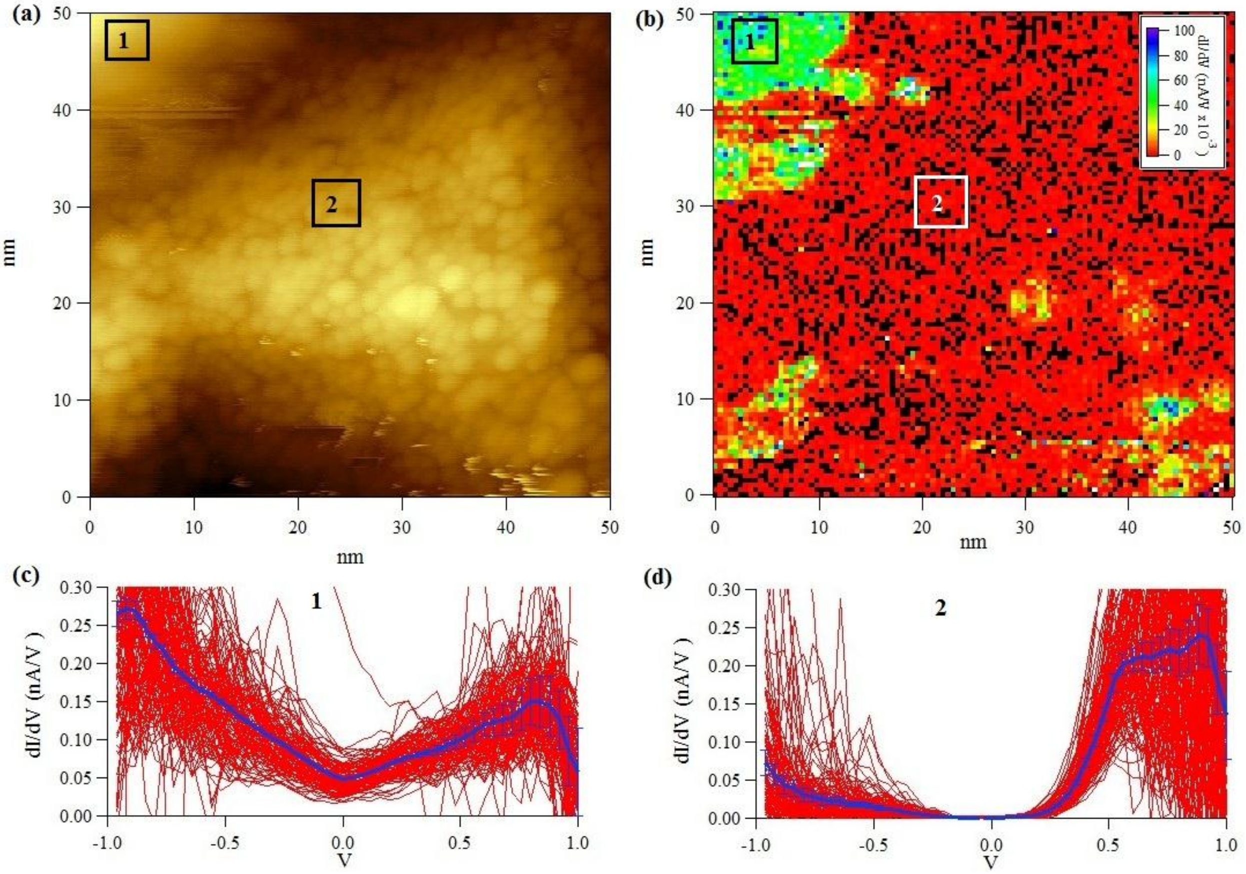

**Figure 28: Early stages of oxidation: (a) 1 V, 0.1 nA. Image of region partially covered with nanospheres. Top left, including Region 1 is free of nanospheres. (b) Spectral map of dI/dV values at $E_F$. (c) and (d) Spectra captured within areas 1 and 2, respectively. Spectra show metallicity in nanosphere-free Region 1 but strong spectral changes over the nanospheres, Region 2.**

has probably already started in areas of the nanosphere region where a small bandgap is seen and an intermediate spectral shape between that of the metal and $WO_3$ is observed (for comparison, spectra for W and $WO_3$ are seen in Figure 45).

After the controlled oxidation of the surface at 300˚C ($3.3\text{x}10^{16}$ $O_2/cm^2$), no obvious topographic changes to the surface were observed and even the surface ridges were preserved. The preservation of the surface ridges is indeed unexpected, especially since the oxidation already started at very low $O_2$ exposure. These ridges are presumably related to a surface reconstruction since the features are atomic-scale, both in height and extension. It is highly unusual for a true surface reconstruction to be preserved during oxidation.

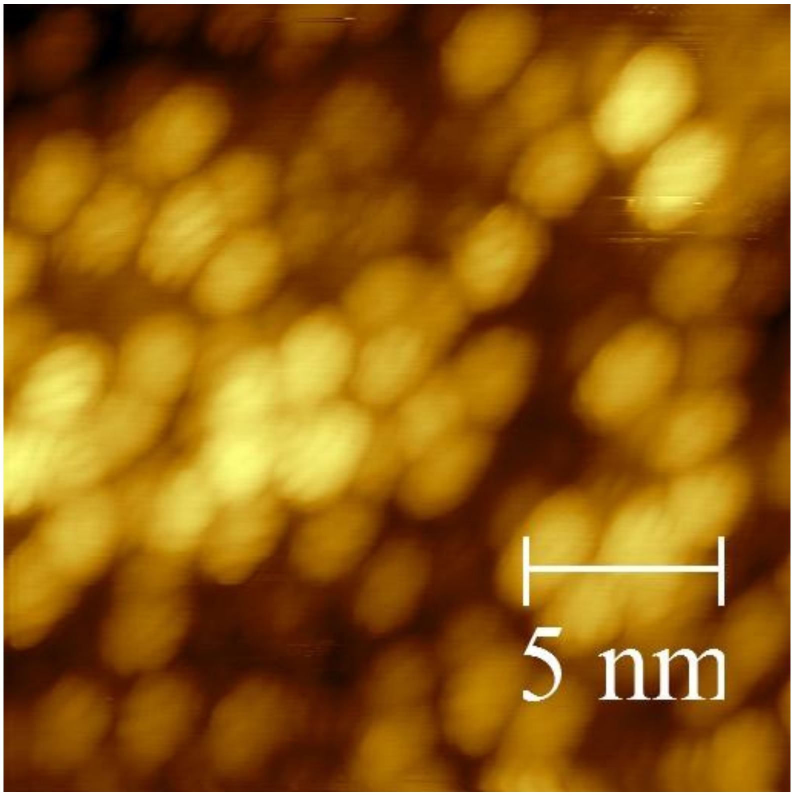

**Figure 29: 1 V, 1.5 nA. Image of nanosphere covered region after oxidation at 300˚C ($3.3\text{x}10^{16}$ $O_2/cm^2$). The ridges on top of the nanospheres are unaltered.**

Spectroscopic investigation of the surface shows that the conversion of the surface to $WO_3$ remains incomplete (compare to Figure 45) even after the controlled oxidation. In Figure 30, regions 1 and 2 are both in a region entirely covered with nanospheres. Regions 3 and 4 are not covered with nanospheres and most likely represent the original W prior to the oxidation step. The growth of an oxidized region does not appear to be strongly impeded by the boundary of a nanosphere as the area around region 1 is a single oxide island that has overgrown

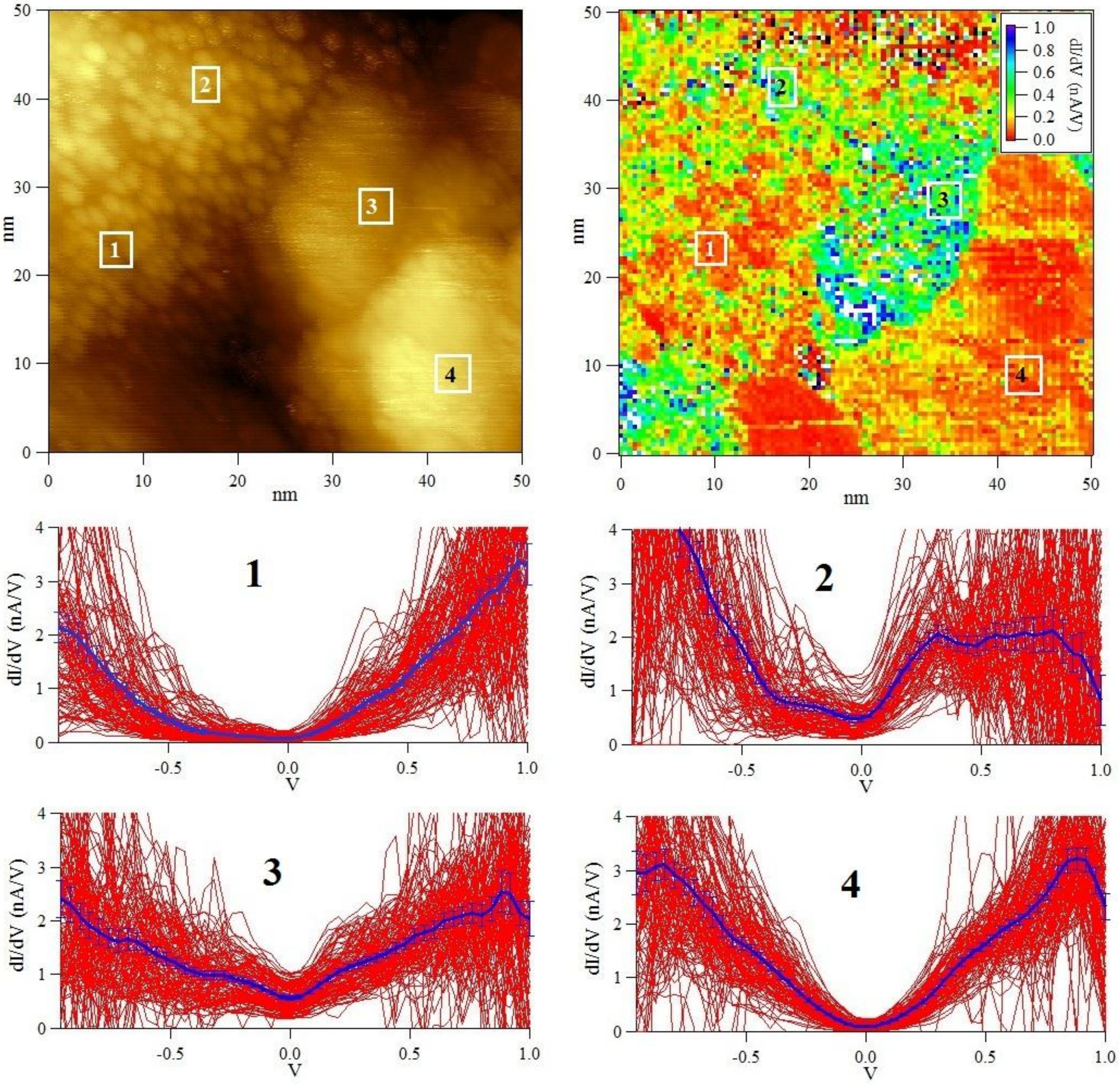

**Figure 30: (a) 1 V, 1.5 nA. Image of region fully partially covered with nanospheres after controlled oxidation. (b) Spectral map of dI/dV values at $E_F$. (c) through (f) Spectra captured within areas 1 through 4, respectively. Spectra show the progression of oxidation within the nanosphere region (1,2) and within an area of exposed W (3,4). The nanospheres are more susceptible to oxidation than the nearby W.**

several adjacent nanospheres.

The spectra in region 1 have transitioned to a state with an LDOS much closer to that observed for $WO_3$. This transition seems to evolve gradually with the negative polarity (filled states) side of the dI/dV curve approaching the x-axis while the empty states remain relatively static. Region 2 shows that the areas without widespread oxidation show considerable variability in the spectral shapes, both in a wider envelope that the spectra occupy and in the wider 95% confidence interval error bars around the average of the displayed spectra. Likewise, regions 3 and 4 show differing degrees of W oxidation. The less oxidized spectra are relatively featureless and oxidation results in a reduction of the $E_F$ dI/dV. More extensive oxidation of W on graphite done in prior experiments with the same methodology results in a reduction of LDOS, similar to what is observed here for the nanospheres. After very extensive oxidation, the LDOS comes to resemble the bulk $WO_3$ band structure, with a bandgap from -2 V to +0.5 V and $E_F$ positioned near the conduction band minimum. It seems clear that the nanospheres are significantly more susceptible to oxidation than W at these oxidation conditions, consistent with changes observed in Figure 28.

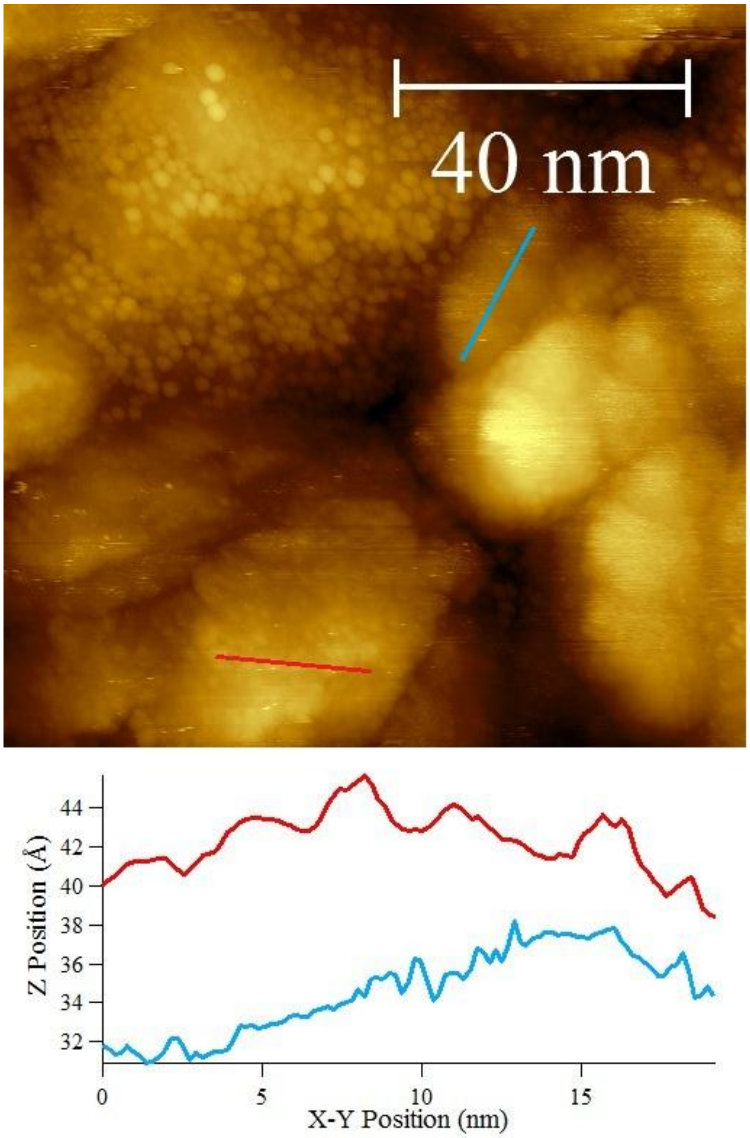

**Figure 31: 1 V, 1.5 nA. Image containing several different varieties of surface structure. The blue and red linescans show how the region with the red linescan has a surface texture similar to the nanosphere covered region but with much shorter structures.**

Assigning the designations of "W-covered" and "nanosphere-covered" was also more difficult on this surface as there are regions where the incorporation of the nanospheres into the film surface is nearly complete. This is likely the case for the region with the red linescan in Figure 31. The surface texture is quite dissimilar from the bare W (blue linescan). The surface features are much larger, both in width and height. The general appearance and measured linescans are consistent with nanospheres that have a similar width to the distribution in Figure 23 but with heights compressed to 1-3 Å (measured from the red linescan), as compared to the 5-8 Å measured prior to oxidation. Whether this near total incorporation of the nanospheres into the W surface occurred prior to, or as a result of oxidation at elevated temperature (300˚C) is unclear. This type of surface feature was not observed prior to oxidation, but the sample of well-resolved images of the surface prior to oxidation is small enough that the possibility cannot be discounted.

The area of the blue linescan corresponds to Region 3 of Figure 30. This region does not have features like the area of the blue linescan, but rather more similar to the 600˚C W deposition in Figure 19b, and so it can be said with some confidence that this was a region of pristine W prior to oxidation.

## Section 4.6 Analysis of Nanosphere Structure - TEM Studies

One tantalizing question about the nanospheres is whether they are hollow inside. This information would provide more basis for understanding their synthesis and would certainly have

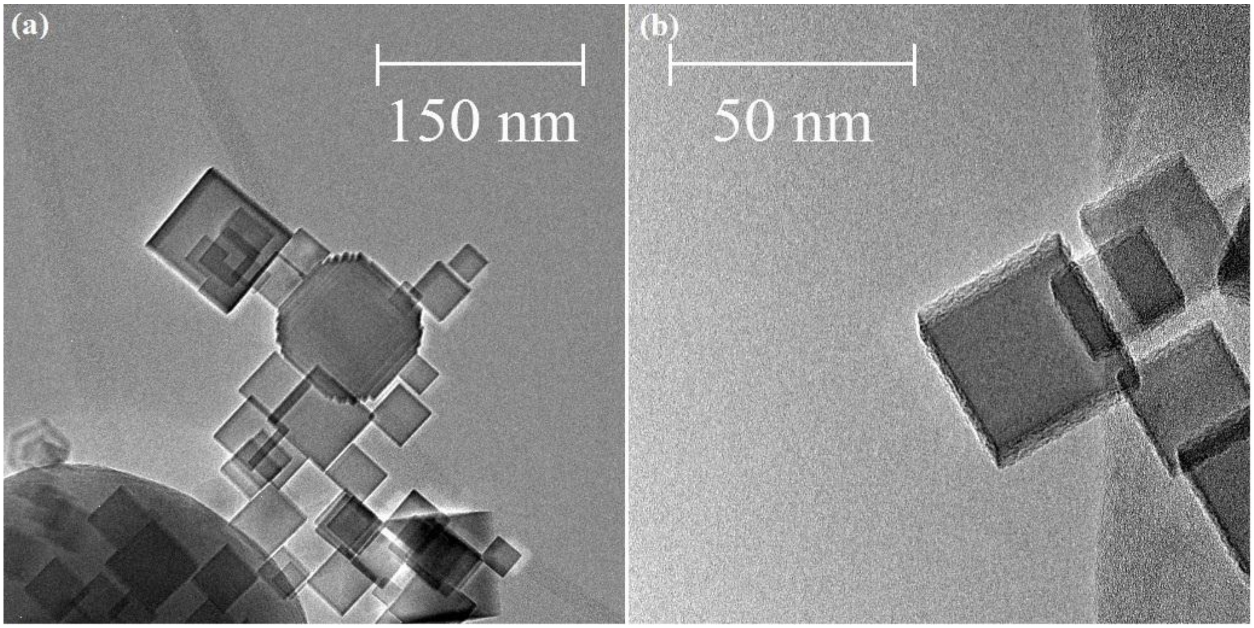

**Figure 32: TEM images of nanocubes on holey carbon grid shortly after synthesis. a) Nanocubes tended to cluster together on the grid. b) More surface roughness relative to the prepared MgO single crystals was observed. c) Atomic resolution shows that lattice is free of visible defects**

implications for the sort of properties they exhibit. Unfortunately, STM analysis cannot provide this information directly. TEM seems to be the most straightforward path for accessing this information. The samples described above are not ideal for TEM analysis since cross sectioning is required and it is not clear the nanospheres adhere to the surface well enough to remain stationary during the cross sectioning process. Instead, we decided to make use of a process where MgO nanocubes of high quality can be grown in air directly on the surface of a holey carbon TEM grid.[93–95] These nanocubes can then be used as substrates in the same manner as the single crystals but are thin enough to be imaged in the TEM without further processing. To grow the nanocubes, pure Mg ribbon (>99%, Acros Organics) was ignited under a fume hood with a butane torch. A holey carbon TEM grid was then wafted briefly through the smoke which allows the MgO smoke to condense and organize into cubic structures. Several distances and residence times in the smoke were tried with 1 s in the smoke about 5” away from the flame producing the best results.

Figure 32 shows the MgO nanocubes, as imaged by fellow graduate student Matt Schneider with an FEI Titan TEM. The total observed coverage of nanocubes was ~1%. The nanocubes tended to form extended clusters of many cubes and were stacked as little towers. Nanocubes with a side length over 100 nm showed some propensity to facet in a manner so that the overall shape approximated a spherical structure. Nearly all other nanocubes formed a visually perfect cube morphology. From Figure 32b, there was significant surface roughness on the cubes, likely due to the low surface mobility of atoms for this low temperature synthesis. This is in contrast to the extremely flat terraces with well-defined steps for the prepared single crystal MgO. This observations instilled confidence that nanosphere synthesis would be successful, as the nanocubes were of high quality and there was plenty of MgO(100) facets available for line-of-sight deposition.

The TEM grids with the MgO nanocubes were then fixed to a Mo sample plate with spot welded Ta strips and inserted into our deposition chamber. Approximately 5 nm of W was deposited, per QCM calibration, on the grid with the sample plate held at 500˚C. The film was not deposited at 600˚C due to concerns about the stability of the holey carbon film at high temperatures, and 400˚C has been shown to be adequate for epitaxy on MgO for sputtered samples.[47] Ten ML’s of $C_{60}$ were deposited at RT and the sample was heated to 400˚C for 20 minutes, exactly as the single crystal sample was. There are some possible sources of error that should be noted here. The temperature drop across the single crystal MgO and across the TEM grid were unknown and could not be taken into account.

This sample was then imaged with TEM after approximately two hours in air to allow transfer to the TEM. The images are shown in Figure 33. The nanocubes remain well resolved. A deposition in the form of small clusters is visible on the holey carbon grid as well as on the MgO cubes. The clusters on the MgO cubes are close in size to the nanospheres but we have not yet achieved atomic resolution on these structures. The biggest challenge in this TEM analysis is

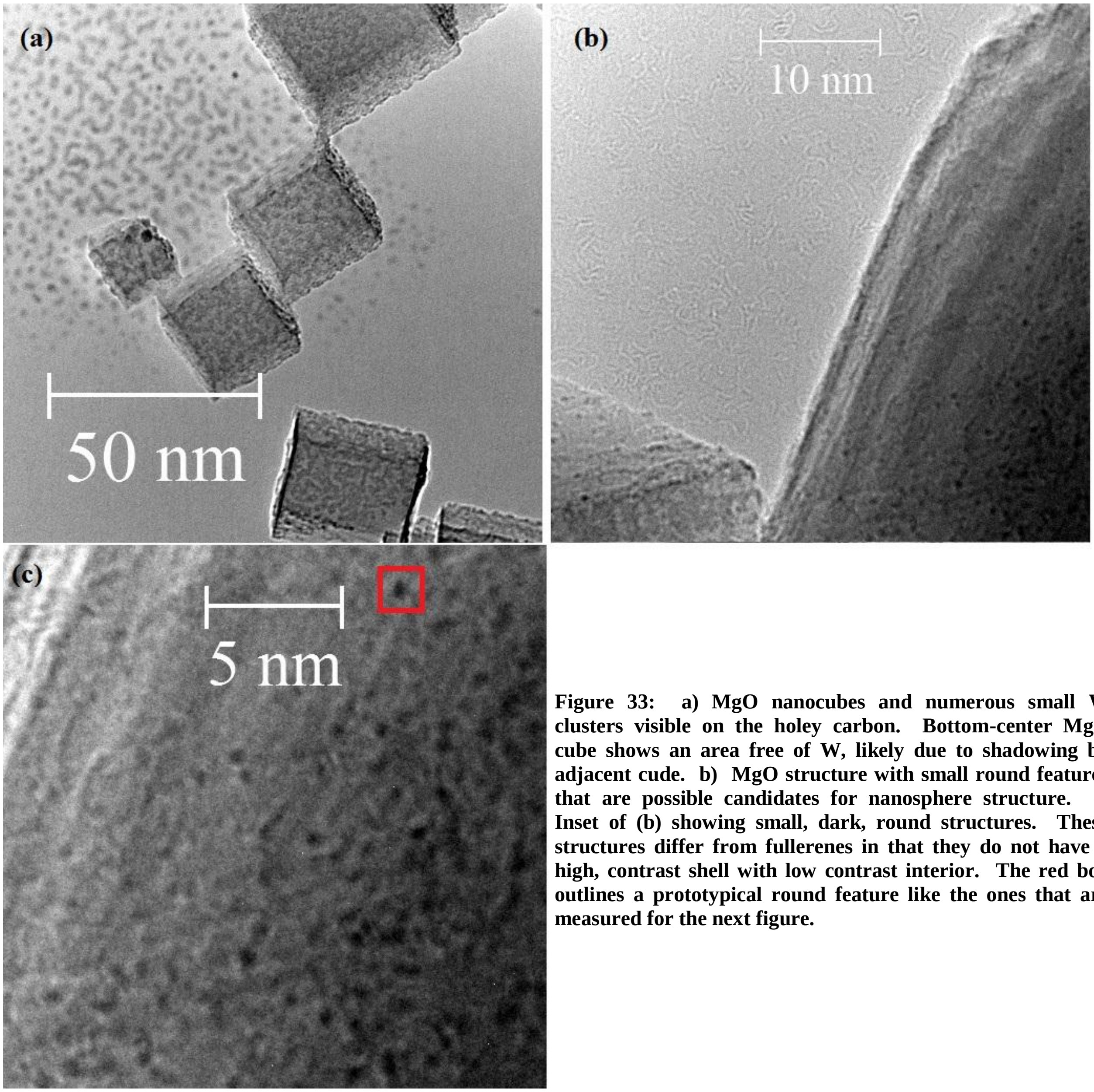

**Figure 33: a) MgO nanocubes and numerous small W clusters visible on the holey carbon. Bottom-center MgO cube shows an area free of W, likely due to shadowing by adjacent cude. b) MgO structure with small round features that are possible candidates for nanosphere structure. c) Inset of (b) showing small, dark, round structures. These structures differ from fullerenes in that they do not have a high, contrast shell with low contrast interior. The red box outlines a prototypical round feature like the ones that are measured for the next figure.**

that the TEM cube stacks “sway” continuously while imaging, which diminishes the TEM resolution.

These results show that this approach to investigating the nanospheres is worth pursuing further. In the future, there certainly needs to be a thicker layer of W deposited to better simulate the conditions that previously led to the growth of nanospheres.

## Section 4.7 Discussion

These nanospheres are quite remarkable from a nanostructure perspective because of their small and very narrow size distribution along with their temperature stability against sintering compared to similarly sized metallic clusters.[96] Controlling the size distribution of very small metallic nanostructures allows in turn for the control of quantum size effects which are relevant for a number of applications since they modulate properties from energy level spacing to heat capacity and optical absorption.[97] Production of nanoclusters in this size range is also of interest because it maximizes the proportion of metal atoms that are at the surface and can participate in any catalytic reactions. Since WC is a catalytic surface of interest, the novel nanostructure presented is relevant in and of itself, but the reactivity will likely be perturbed from that of a bulk terminated WC surface. Whether these changes are detrimental or enhance catalytic activity is unknown. Further investigation into the properties and synthesis of this structure is certainly warranted.

For the 400˚C synthesis, which is adequate to fully form the nanospheres, the distribution is narrowly peaked between 1 and 1.5 nm in diameter but broadens for the higher 500˚C annealing temperature. With a more accurate determination of the minimum temperature to form the nanospheres, even narrower size distributions might be achieved since excess heating seems to cause the nanospheres to slowly dissolve into the W film and it is unknown whether the nanospheres might form below 400˚C, although XPS of $C_{60}$ annealed on W rules out formation at temperatures below 225˚C.[38]

To unravel why the nanospheres form in the presence of W, a model is presented for their evolution. In some ways, the evolution of the nanospheres can be compared to previously observed reconstruction of metal surfaces in the presence of $C_{60}$. Specifically, Ni(110) reconstructs into parallel grooves that maximize contact with a layer of adsorbed $C_{60}$ while Cu(110) does not. To explain this, the authors show that hybridization of the metal d-states and the $C_{60}$ LUMO states can be modeled as a perturbation where the energy gain through hybridization should be much more significant for Ni(110) than Cu(110) based on the location of the d-band center.[33] An analogous argument for the W-$C_{60}$ interaction can be made with the only difference being that in the case of W, the d-band narrows rather than shifts[98] upon a reduction in coordination. This agrees with the observation that W bonds readily to $C_{60}$, at least in the presence of additional ligands, through back-donation of d-electrons into the LUMO levels of the $C_{60}$.[57]

The W atoms at the surface a nanosphere are less well coordinated electronically than corresponding W atoms at the surface of the W film, based on the convex curvature of the nanosphere surface. For W atoms to relocate from the substrate to the nanosphere surface, W-C bonds that form in the nanosphere structure must lower the atoms' energy enough to offset the energy increase induced by the lowering of electronic coordination at the nanosphere surface. If the entire nanosphere is converted to a WC phase, the loss of W coordination may not be energetically unfavorable since the cohesive energy of WC and $W_2C$ are significantly higher than W.

This explanation is satisfying from a thermodynamic perspective, but it leaves the kinetics of the process unclear. If W reacts with the fullerene in a manner that destroys the cage structure, this reaction must not occur until the cage is fully coated in W if the spherical structure is to be maintained. There are large energetic barriers to W atoms reducing their coordination which would be required to form a coating around the $C_{60}$. Could the W atoms bond with the fullerene as the shell grows, with the fullerene cage being preserved until the fullerene has been fully coated? Since the bonding of multiple W atoms to a single $C_{60}$ has not been experimentally observed, DFT must be consulted for support. Fortunately, some work has been done considering a $W_2$ molecule bonded to a fullerene via a single bond from one of the W atoms.[99] In this simulation, the bond strength was found to be 1.73 eV for an initially neutral $W_2$.

The change in cohesive energy of a tungsten atom due to a change in coordination can be calculated using a simple equation developed to explain trends within a tight-binding model:

$$E_C = AC^{\frac{2}{3}}$$

where $E_C$ is the energy of all interactions with surrounding atoms, A is a fitting constant, and C is the number of nearest neighbors.[100] From this equation, the extra 1.73 eV available from bonding to a fullerene is enough to offset the increase in energy due to a reduction in coordination by a single atom. This is helpful, but not enough to explain the structure since many W atoms must reduce their coordination as the shell grows around the fullerene. Additionally, the same DFT study found that two W atoms, bonded separately to a fullerene was very unfavorable energetically.

Another mechanism that could explain the structure is one in which W atoms are incorporated into the fullerene cage structure. It has already been predicted that a nanotube with a W/C lattice instead of a C lattice will be stable, via DFT simulations.[101,102] This structure is made up of a square 2-D lattice that is rolled into a tube structure with W-C bonding maintained everywhere. Also, simulations using semi-empirical methods have predicted the stability of fullerenes with C atoms substituted by Si, Ge, Al,[103] Zn, Cd, or Hg.[104] These fullerenes are predicted to be less stable and more reactive than $C_{60}$.

An explanation of the nanospheres involving a substitution of C atoms for W in the fullerene cage is attractive because it is consistent with several observations about the nanospheres. For one, many nanospheres were observed with diameters that are nearly identical to bare fullerenes. This implies that the physical size of the molecule has not increased significantly. Any explanation that involves an overgrowth of W around the fullerene is more likely to lead to a significant increase of the size distribution of the resulting structure. Substitution without direct bonding to the substrate could also explain why some nanospheres are mobile on the surface under the influence of the tip, while strong chemical bonding of the substrate to the nanosphere makes this phenomenon unlikely.

# Chapter V. Codeposition at High T and Formation of $W_xC_{1-x}$

A central aspect of this project was to investigate how variations in the WC stoichiometry affect the ultrathin films' properties and their subsequent susceptibility to oxidation. To this end, significant work was done preparing codeposited thin films from $C_{60}$ and W at elevated temperatures where the fullerene would be destroyed and incorporated into the carbide structure. Films were prepared with compositions of nominally 50, 60, and 75 atom% carbon per QCM calibrations (50/50, 60/40, 75/25) with thicknesses of 30 and 80 nm. The morphology of the films will be discussed initially, with spectroscopic and XPS data following in turn. An XPS analysis for a more precise determination of film compositions is in progress.

Table 1 is provided below as a guide to all of the figures presented in this chapter.

**Table 1**

| Figure # | Thickness (nm) | Composition (C/W) | Image Size (nm) | Analyses |
|---|---|---|---|---|
| **34** | 80 | 50/50, 60/40, 75/25 | 500-2000 | STM |
| **35** | 30 | 50/50, 60/40 | 1000-2000 | STM |
| **36** | 80 | 50/50, 60/40, 75/25 | 100-200 | STM |
| **37** | 80 | 50/50 | 500 | STM |
| **38** | 30 | 60/40 | 110 | STM |
| **39** | 80 | 50/50 | 50 | STM |
| **40** | 30 | 50/50 | 20 | STM, FFT |
| **41** | 30 | 50/50 | 50 | STM, STS |
| **42** | 80 | 60/40 | 15 | STM |
| **43** | 80 | 60/40 | 15 | STM, STS |
| **44** | - | 50/50, 60/40 | - | XPS |

## Section 5.1 Morphology and Composition of Codeposited Films

The initial set of films discussed are all ~80 nm thick as determined by the relative deposition rates, with a deposition rate of ~1.3 nm/min onto MgO(100) substrates held at 800˚C with a 10 min post-deposition anneal, also at 800˚C.

Figure 34 is a series of large area images of the three surface compositions. The 50/50 surface is filled with square islands 50-300 nm across. Steps between terraces are 1-2 nm in height. These islands have a preferential orientation across a very wide area indicating the

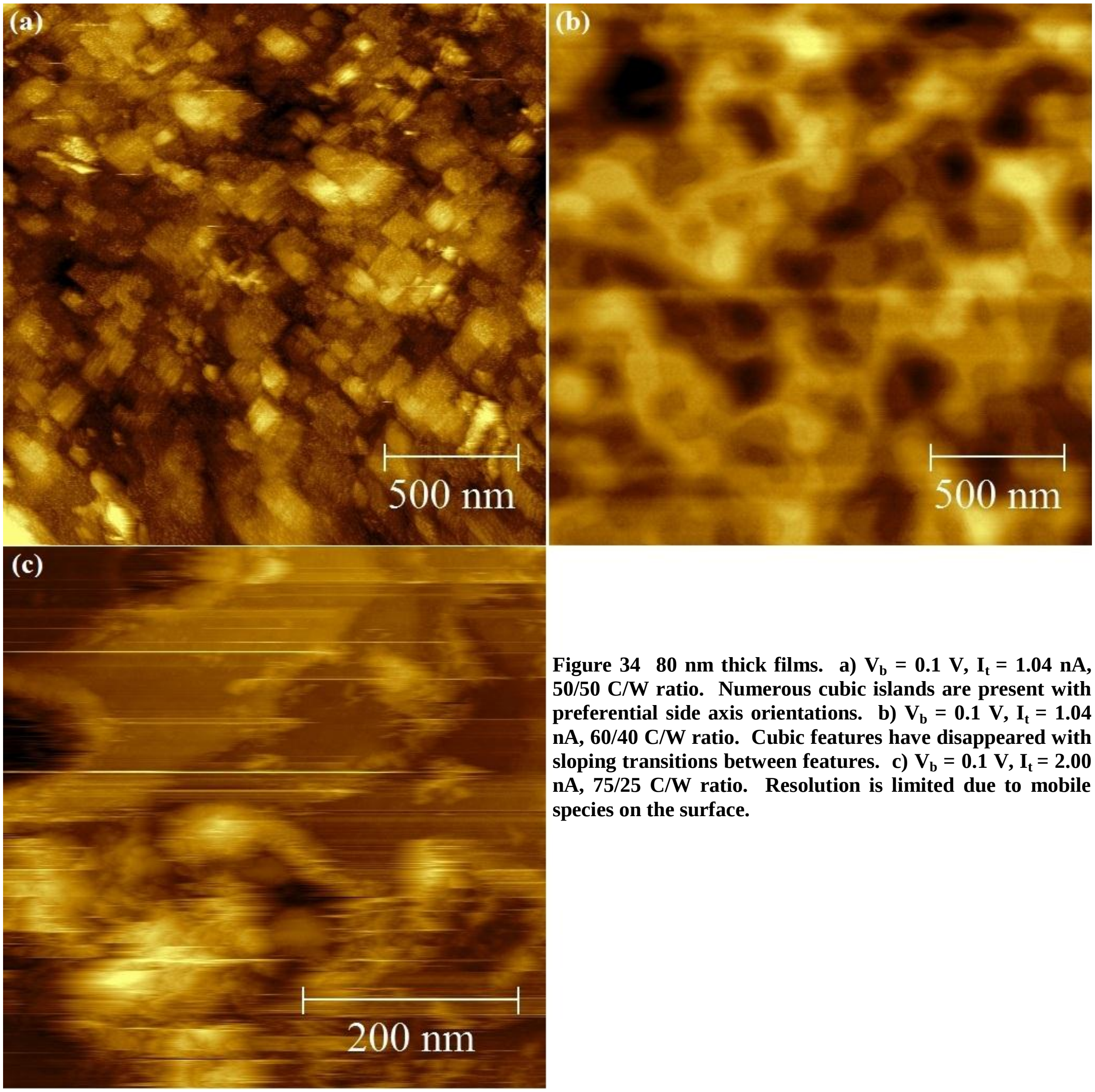

**Figure 34 80 nm thick films. a) $V_b$ = 0.1 V, $I_t$ = 1.04 nA, 50/50 C/W ratio. Numerous cubic islands are present with preferential side axis orientations. b) $V_b$ = 0.1 V, $I_t$ = 1.04 nA, 60/40 C/W ratio. Cubic features have disappeared with sloping transitions between features. c) $V_b$ = 0.1 V, $I_t$ = 2.00 nA, 75/25 C/W ratio. Resolution is limited due to mobile species on the surface.**

substrate is likely influencing the island orientation through epitaxy. These films are much more homogenous than the W films discussed in the last chapter, which had significant variation in morphology at different macroscopic locations on the sample. The improved homogeneity may owe to application of Ag glue across the entire interface of the MgO and sample plate that began with these samples.

The 60/40 surface is distinct from the 50/50 in that the cubic morphology is completely absent. The surface is characterized by gradual transitions between areas of differing height. It is likely that thermodynamically favored phase separation of the graphite from the carbide/tungsten already modifies the morphology to a large degree, as expected from the phase diagram (Figure 4).

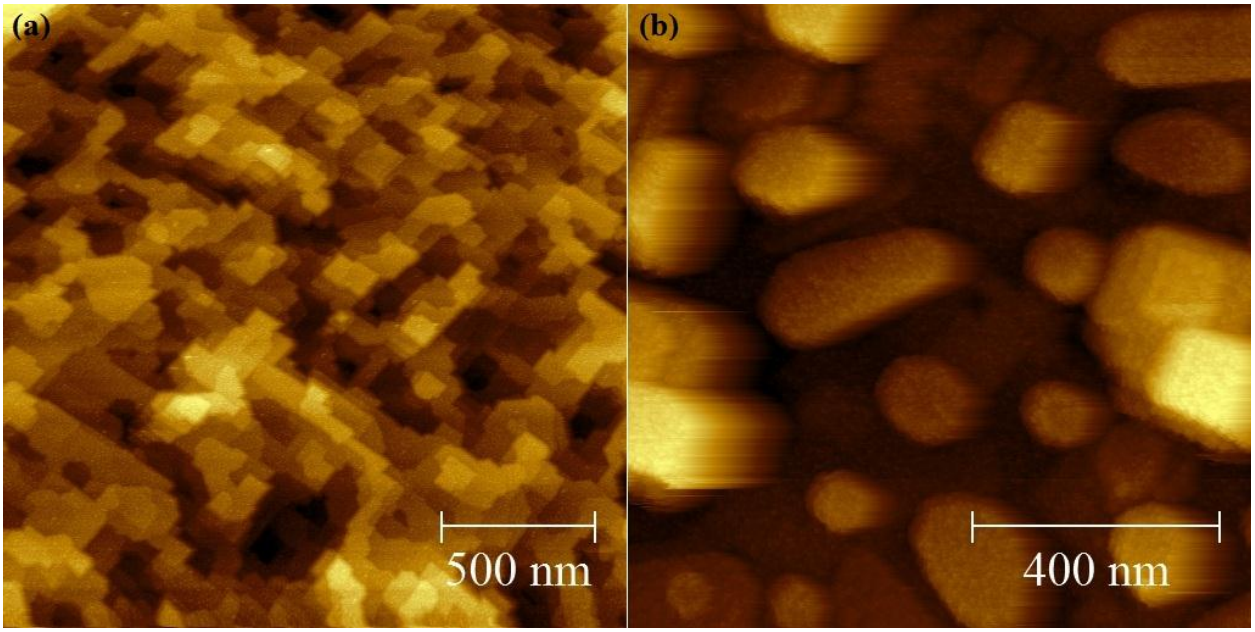

**Figure 35: a) $V_b$ = 0.1 V, $I_t$ = 1.50 nA, 50/50 C/W ratio. This 30 nm thick film shows cubic character but also long, meandering islands very similar to the underlying MgO substrate. b) $V_b$ = 0.1 V, $I_t$ = 0.60 nA, 60/40 C/W ratio. Presence of distinct islands with some showing cubic character, in contrast to thicker 60/40 film, where no island structure is observed.**

The 75/25 surface is characterized by a high mobility of surface species that obscure imaging at large length scales. In this case there are likely sizable, continuous regions of graphite which can be deformed under the influence of the tunneling tip. The particles, which can also be seen in Figure 34c appear to be rather mobile during imaging.

A second set of films was prepared in an identical way but with a thickness of ~30 nm. Wide area images of these films are presented in Figure 35. The morphologies share general characteristics with the thicker films.  The 50/50 surface again has many cubic features, but many of the islands are long and narrow and trace curving paths on top of the substrate.  This is likely due to the underlying MgO, whose morphology (Figure 3) is still mirrored in the morphology of the islands.

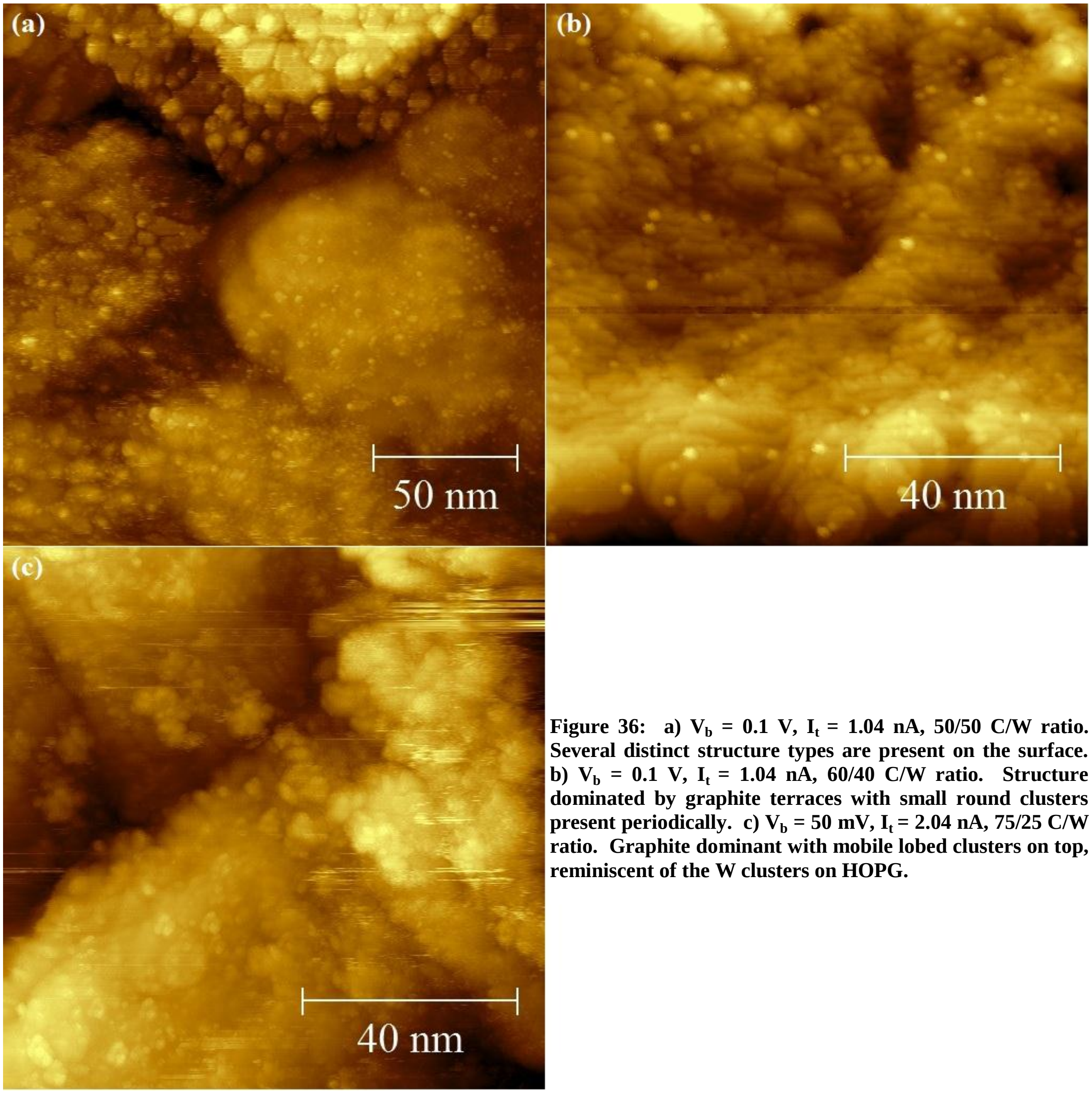

**Figure 36: a) $V_b$ = 0.1 V, $I_t$ = 1.04 nA, 50/50 C/W ratio. Several distinct structure types are present on the surface. b) $V_b$ = 0.1 V, $I_t$ = 1.04 nA, 60/40 C/W ratio. Structure dominated by graphite terraces with small round clusters present periodically. c) $V_b$ = 50 mV, $I_t$ = 2.04 nA, 75/25 C/W ratio. Graphite dominant with mobile lobed clusters on top, reminiscent of the W clusters on HOPG.**

The 60/40 30 nm surface (Figure 35b) displays distinct islands, in contrast with the thicker film of the same composition. Some islands show a cubic character with preferred orientation that is again absent in the thicker film. This is an indication that a cubic phase initially grows epitaxially on the substrate, likely metastable cubic $WC_{1-x}$ which is stable in the phase diagram between 2530 and 2750˚C and in the vicinity of 38% C (the stable WC and $W_2C$ are both hexagonal). The cubic phase is therefore stabilized by the MgO substrate. If the absence of cubic islands in the 80 nm film occurs because either graphite segregation interrupts epitaxy, or the surface segregated graphite obscures the underlying carbide.

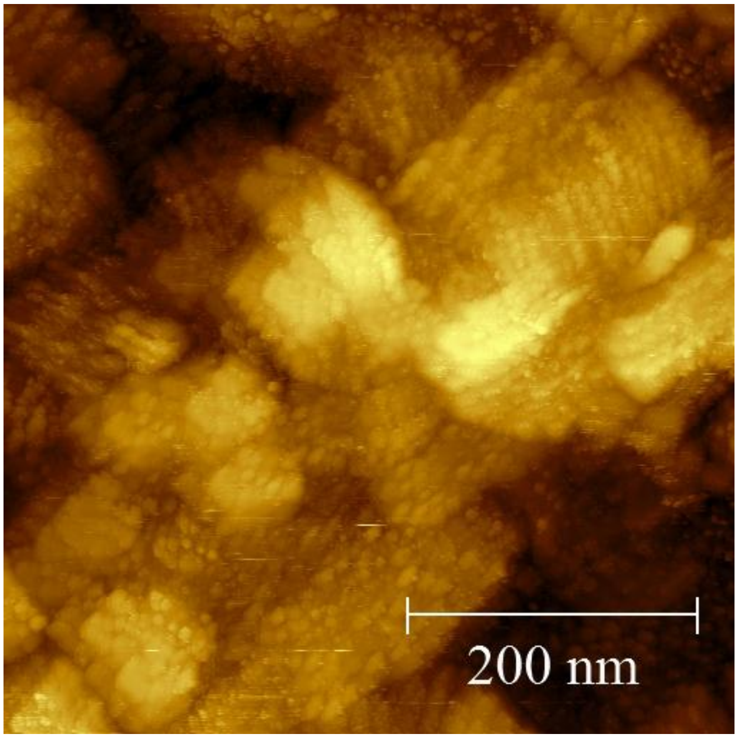

**Figure 37: $V_b$ = 0.1 V, $I_t$ = 1.04 nA, 50/50 C/W ratio, 80 nm thick. Elliptical islands organize into stripes pointing in preferred directions.**

At higher magnifications additional differences between the films emerge. Figure 36 shows the same three compositions for the 80 nm films. The 50/50 film in Figure 36a shows a hierarchy of morphologies: well-defined 10-30 nm diameter ellipsoidal islands which are the constituents of the larger cubic islands visible in Figure 34a, 50-100 nm irregularly shaped islands as in the center right of the image, and smaller 1-5 nm clusters dispersed across the surface of the irregularly shaped islands. Some of the ellipsoidal islands are arranged into parallel stripes as in Figure 37. The 30 nm thick 50/50 film showed the same collection of surface features at this size scale.

The 60/40 80 nm surface in Figure 36b is characterized by a highly layered structure with small clusters 2-5 nm in diameter and 5-10 Å tall. The steps between layers are 3-4 Å and are likely composed of graphite, which has a 3.35 Å interlayer distance.

By way of contrast, the 30 nm 60/40 film (Figure 38), is heavily covered by well-defined 10-20 nm islands that are very similar to the islands observed on the 80 nm

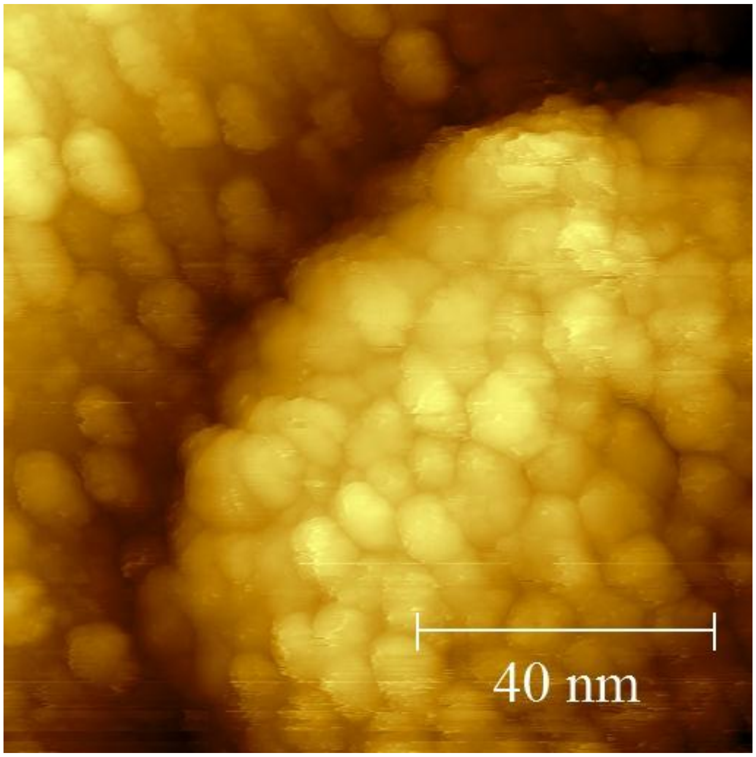

**Figure 38: $V_b$ = 0.1 V, $I_t$ = 0.60 nA, 60/40 C/W ratio, 30 nm thick. These well-defined islands are very similar to one type of feature on the 50/50 80 nm surface.**

50/50 surface, even having the preferred orientations and positioning that formed the stripes on top of some of the cubic islands (e.g. Figure 37), as can be seen in the top left corner of Figure 38. Only a small minority of areas were found with graphite or graphene. This could be due to a miscalibration of the deposition rates measured on QCM or that the surface evolves as a function of thickness, perhaps because epitaxy has not been interrupted at this early stage. In progress XPS analysis of these films should settle this question.

The 75/25 80 nm surface (Figure 36c) has large graphitized regions, confirmed by the characteristic 3.3 Å steps between terraces. The contribution from these extensive graphitized regions dramatically affects the film growth allowing for the growth of free lobed clusters reminiscent of the W clusters on graphite (e.g. Figure 10b). These results indicate a substantial modification of the film growth as a function of composition. The surface termination is dominated by graphite, which is also seen in atomic resolution images in the next section.

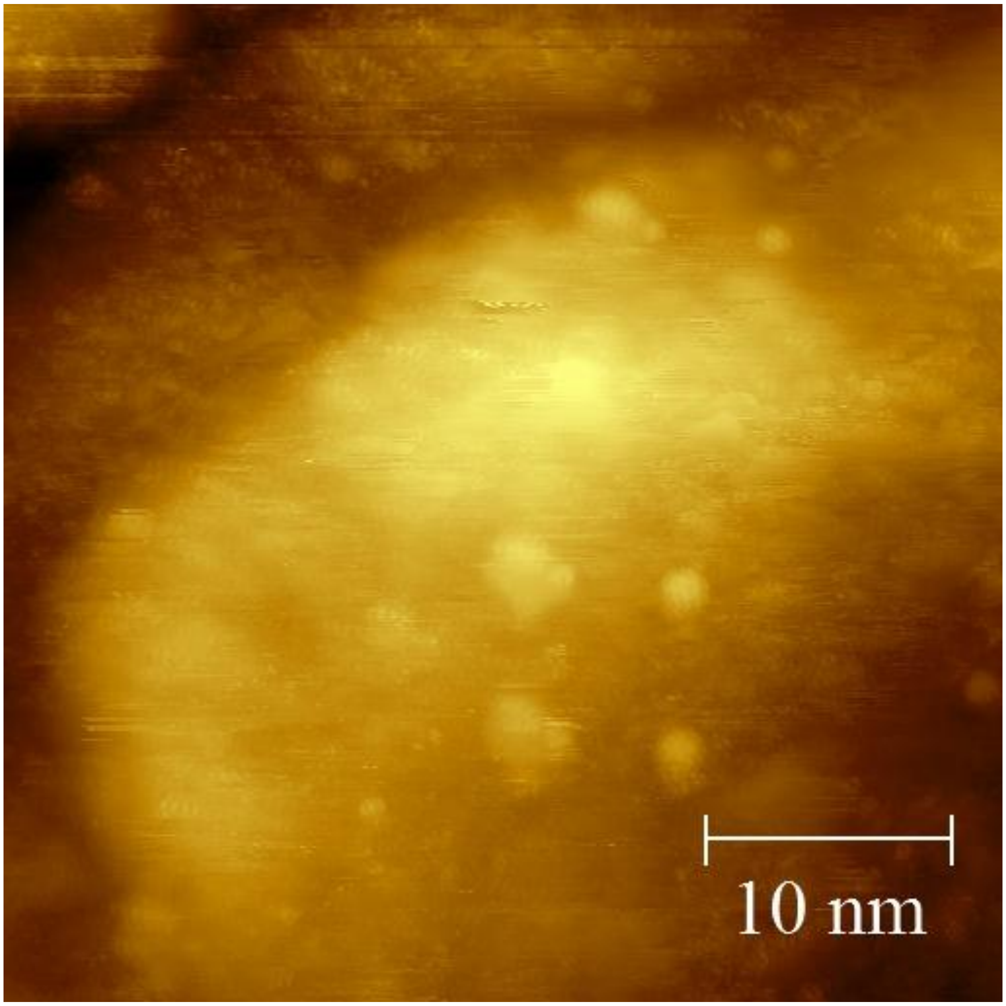

**Figure 39: $V_b$ = 0.1 V, $I_t$ = 1.04 nA, 50/50 C/W ratio, 80 nm thick. Higher magnification of central cloud-like region of Figure 36a reveals numerous parallel striped structures.**

Short, atomic scale stripes (Figure 39) were observed on the irregularly shaped island (distinct from the ellipsoidal islands) of the 50/50 80 nm surface in Figure 36a, which appeared smooth and featureless at the lower magnification. The lateral stripe separation was 3.05-4.65 Å with an average value of 4.07 Å. The orientation of the stripes spanned a range of angles, but as with the stripes on the nanospheres, these angles spanned a narrow range around the y-axis. It is again likely that this effect can be attributed to limitations of the STM and that the orientation preference is potentially an artifact. A more detailed study of the impact slope and surface roughness has on imaging is in progress.

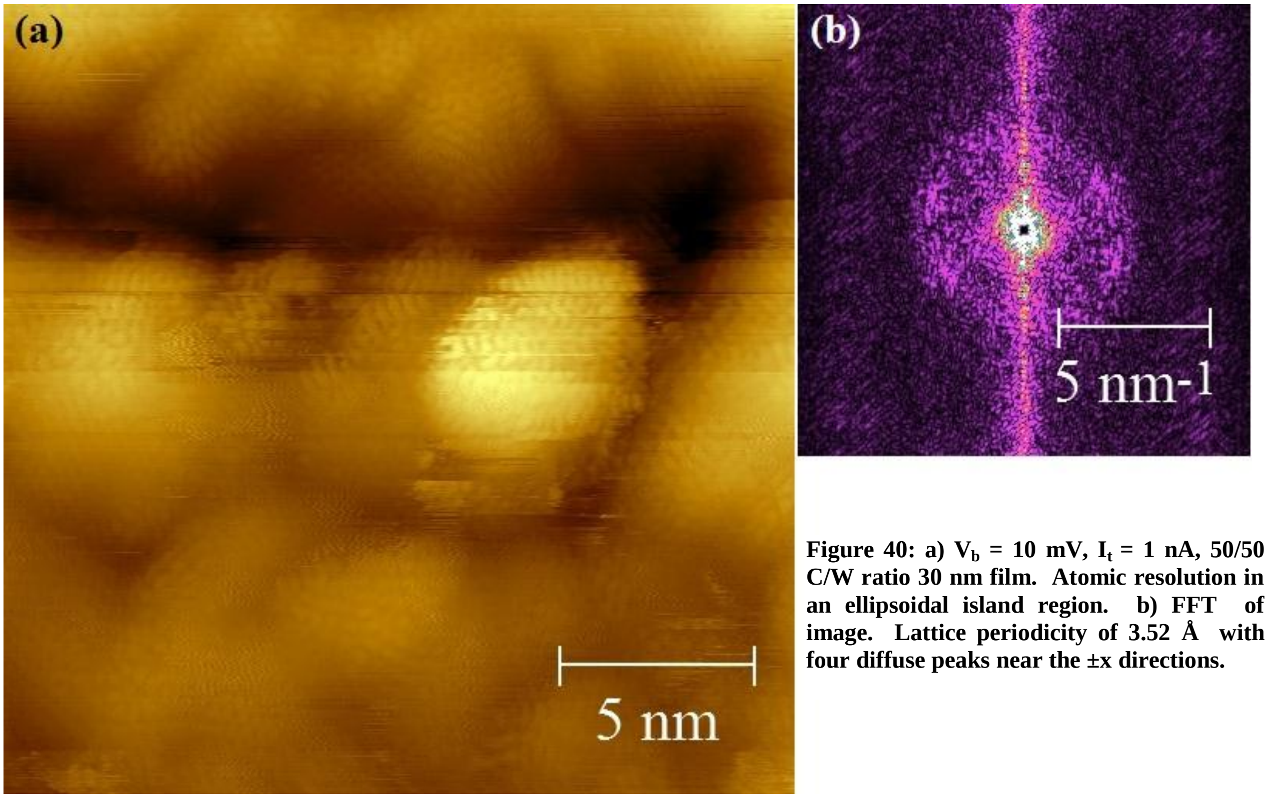

**Figure 40: a) $V_b$ = 10 mV, $I_t$ = 1 nA, 50/50 C/W ratio 30 nm film. Atomic resolution in an ellipsoidal island region. b) FFT of image. Lattice periodicity of 3.52 Å with four diffuse peaks near the ±x directions.**

Atomic resolution was never obtained on the 50/50 80 nm ellipsoidal island surface but was obtained on these features for the 30 nm film, Figure 40. Fast Fourier Transform (FFT) analysis reveals a diffuse ring with 4 peaks that correspond to a lattice periodicity of 3.46 Å, not very similar to the HOPG measured periodicity of 2.81 Å, again from FFT. The width of the FFT ring also indicates that there are a number of different periodicities occurring in the image, from approximately 2.89 to 4.33 Å. This range effectively excludes graphite as the surface layer here since an FFT of a hypothetical, similarly curved graphite surface would also have a diffuse ring due to distortion of the lattice periodicity on the inclined areas. The FFT of such a graphite surface would have periodicities ranging from about 2.47 Å for the most inclined areas to the

2.81 Å measured on flat HOPG, based on orientations from horizontal to the maximum azimuthal angle measured in Figure 40a.

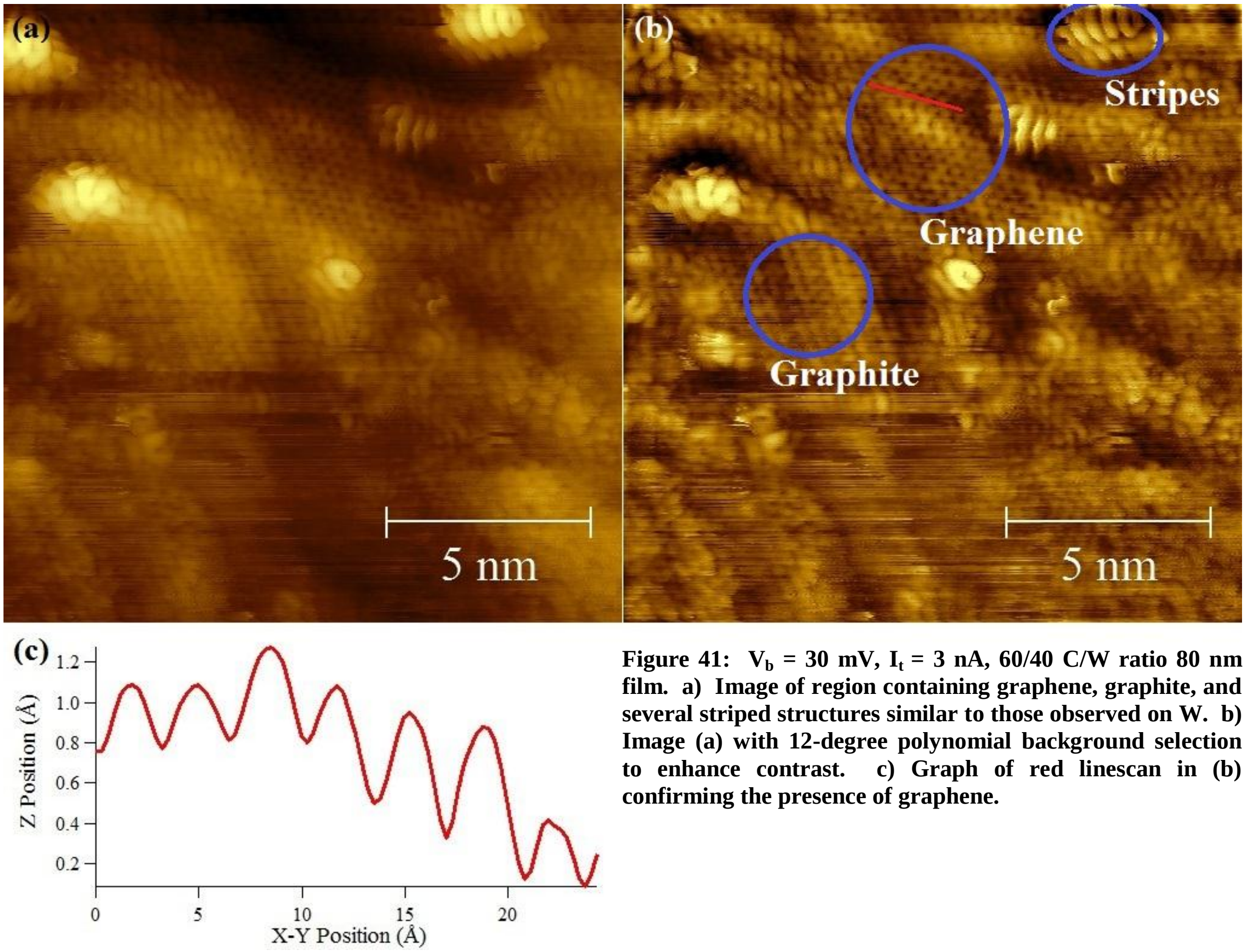

**Figure 41:** $V_b$ = 30 mV, $I_t$ = 3 nA, 60/40 C/W ratio 80 nm film. a) Image of region containing graphene, graphite, and several striped structures similar to those observed on W. b) Image (a) with 12-degree polynomial background selection to enhance contrast. c) Graph of red linescan in (b) confirming the presence of graphene.

The 80 nm thick 60/40 film is characterized at the atomic scale by a near universal coverage with graphite and graphene (Figure 41). The presence of graphene was confirmed by measuring the periodicity of the centers of the carbon rings-the dark spots in the images- to be 3.41 Å. This is in agreement with the 3.40 Å measured on an exfoliated graphene sample on Cu(111) with our STM. The observed coverage of graphene on this surface was approximately 20 %.

In addition to the graphene and graphite, the 60/40 surface exhibits highly localized striped domains with a periodicity of ~3.5 Å and a peak-to-valley corrugation of ~0.8 Å. It is quite likely that these features are formed by misalignment of two sheets of graphene on top of one another, similar to a small region of a Moire pattern. Moire patterns form because the misalignment creates periodically repeating geometries of the top sheet with respect to the bottom.[105] The formation of similar parallel stripes due to Moire pattern formation between two nanotubes of a multi-walled carbon nanotube have been observed.[106]

To recap the morphology observations, on the 50/50 80nm and the 50/50 and 60/40 30 nm surfaces, a cubic morphology was observed with approximately ellipsoidal islands whose atomic periodicity was greater than what is observed on graphite. The 60/40 30 nm surface also had a small fraction of its surface covered by graphite. The 60/40 80 nm surface is fully coated with a mixture of graphene and graphite and lacks evidence of the cubic island structure. The 75/25 80 nm surface is heavily coated with graphite which changes the growth mechanism to one favoring the growth of clusters on top of graphite.

The next few paragraphs will cover STS measurement of some of the films just discussed.

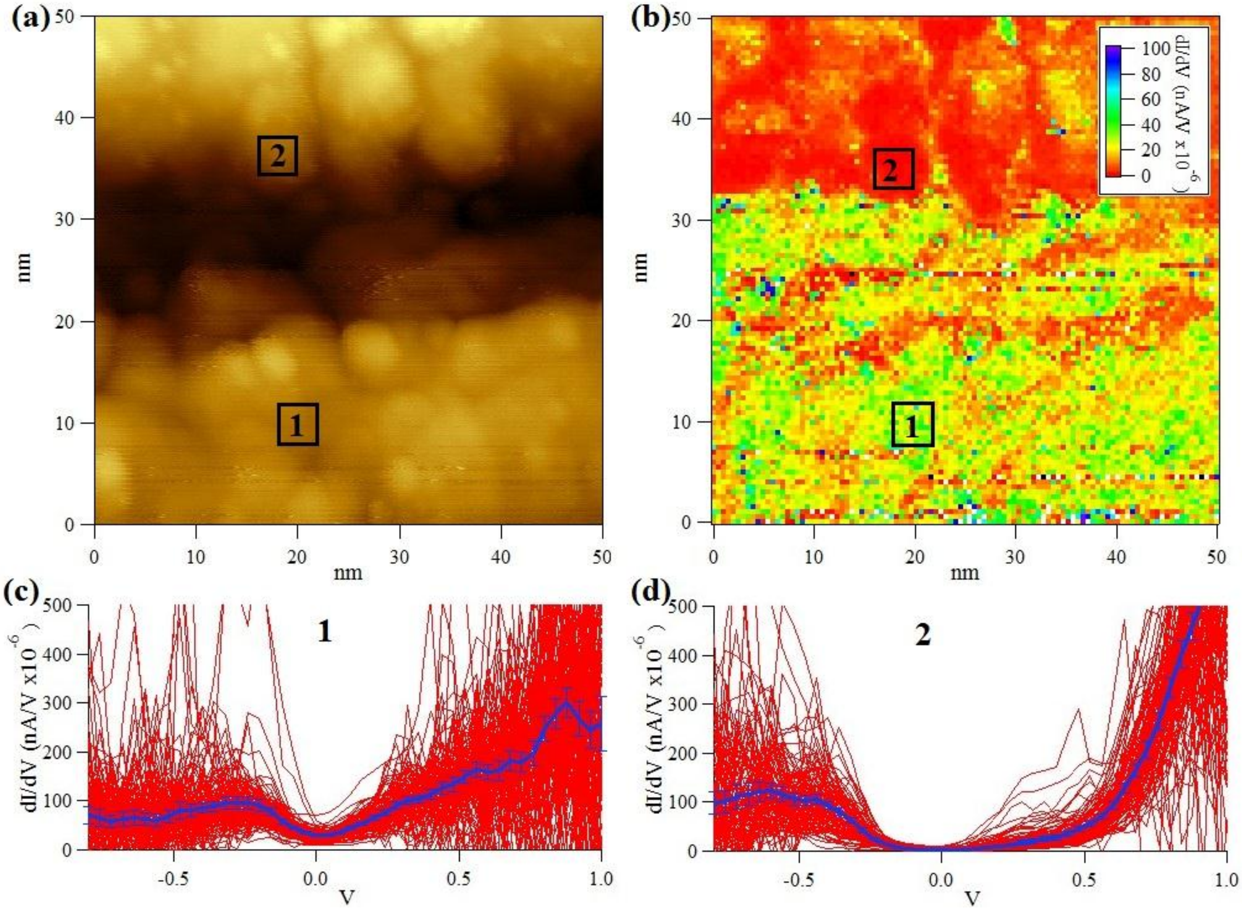

**Figure 42: (a) 1 V, 1.5 nA. Image of 50/50 30 nm region containing primarily ellipsoidal islands which are more visible in lower magnification images of the same region. (b) Spectral map of dI/dV values at $E_F$. (c) and (d) Spectra captured within areas 1 and 2, respectively. Spectra show two distinct, but similar spectral shapes. The features are very different from graphite, but cannot be classified directly since there is no STS of the various tungsten carbides in the literature.**

Figure 42b is an STS map of a region with ellipsoidal islands that make up a much larger cubic structure on the 50/50 30 nm film, as discussed previously (Figure 36a). Figure 40 corresponds to a region near the center of Figure 42. There are two distinct spectral shapes present here, with rather different LDOS at $E_F$. Neither shape is remotely similar to graphite, which presents as a nearly featureless parabola for this range of voltages.

STS of the 60/40 80 nm surface confirms the presence of significant amounts of graphite. From Figure 43, large regions of the surface show spectra that are relatively featureless parabolas like those in region 1, similar to previous spectra taken on HOPG. Spectra on top of a striped region are also most likely graphite or graphene, as the spectra bear little resemblance to the 50/50 surface where graphite is generally absent and are comparable to spectra taken on pure graphite. These STS measurements confirm the general conclusions of the STM morphology analysis.

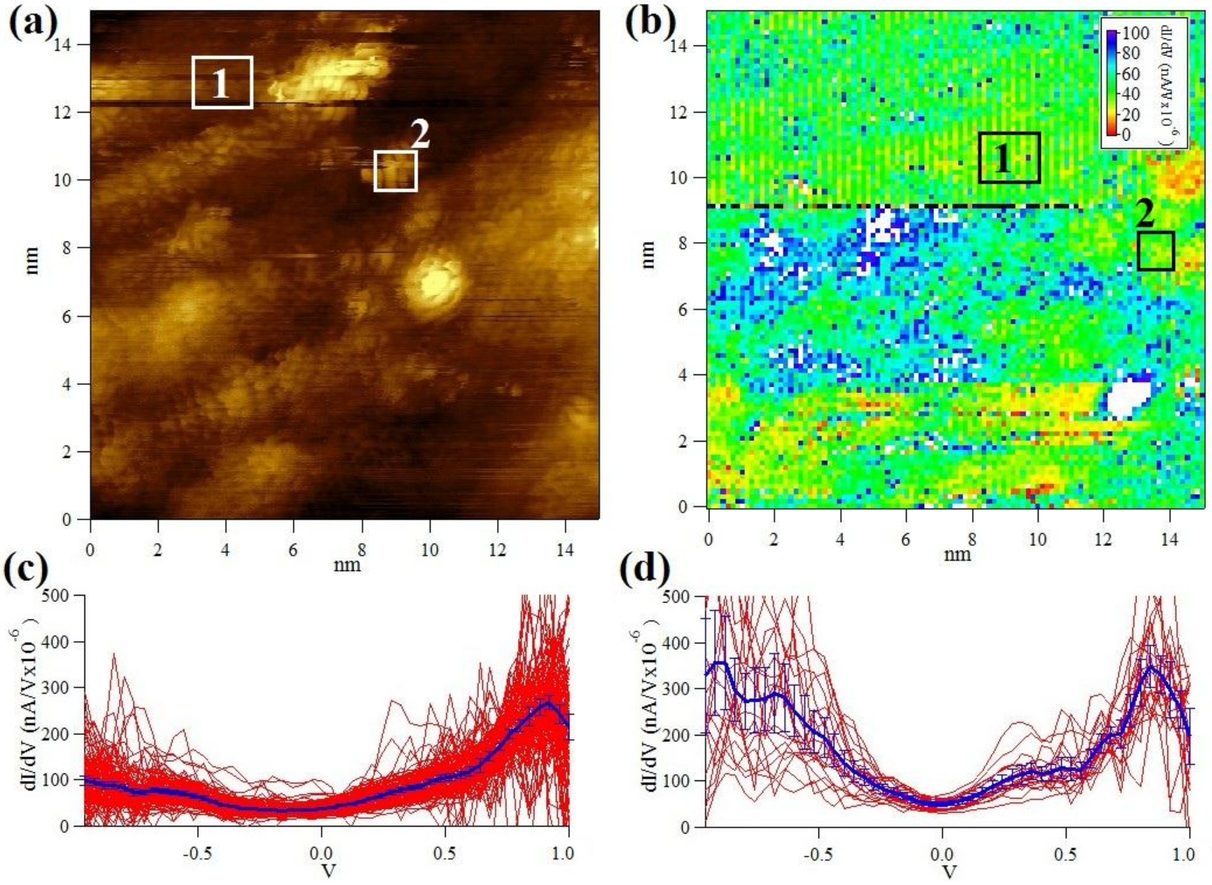

**Figure 43: (a) 30 mV, 3 nA. Image with atomic resolution on several features of interest for the 60/40 80 nm film. (b) Spectral map of dI/dV values at $E_F$ for much of the region (a). (c) through (e) Spectra captured within areas 1 through 3. Region 1 is composed of graphite. Region 2 is a striped feature with a spectral shape much more characteristic of graphite than the carbide.**

XPS analysis performed at Virginia Commonwealth University with Dr. Dmitry Pestov of the 50/50 and 60/40 80 nm surfaces provides additional context for understanding the film growth. Figure 44a shows the XPS spectra in the energy range of the C1s core level. The C1s peak is ideal for phase identification purposes since there is reasonable energy separation between the peaks that are associated with the various phases in the W-C system. Graphite

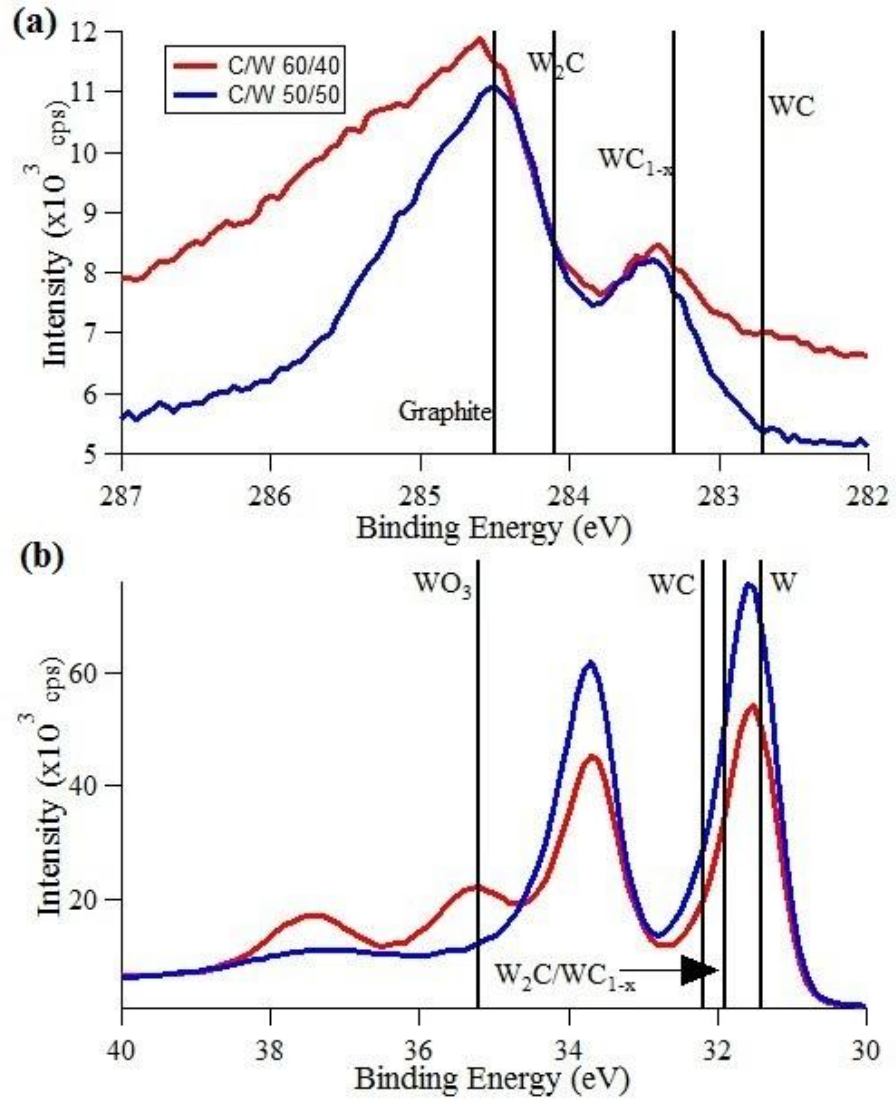

**Figure 44: XPS data showing the (a) C1s and (b) W4f region for both the 50/50 and 60/40 80 nm surfaces along with guides to literature peak positions. The carbide species is most likely WC$_{1-x}$. The 60/40 sample was stored in air for approximately 30 days prior to XPS analysis, explaining the copious amount of WO$_3$.**

bonding results in a peak at 284.6 eV[107] and that peak is strongly represented in both sets of spectra. This was expected for the 60/40 surface where graphite was readily observed everywhere on the surface. This peak position also corresponds to adventitious carbon due to storing samples in air. This could explain the strength of the peak on the 50/50 80 nm film where very little graphite was directly observed on surface. It is also possible that significant amounts of graphite exist near, but not on, the surface of the film and were thus invisible in the STM imaging. WC and W$_2$C have binding energies of the most prominent carbide peaks at about 282.8[107] and 284.1 eV,[108] respectively. Neither of these values were close to the measured peak. The cubic WC$_{1-x}$ phase has an expected peak position of 283.4 eV,[107] very close to the 283.45 eV that was measured here. This is first evidence that both surfaces are dominated by the cubic WC$_{1-x}$ phase and, possibly, graphite.

The W4f XPS spectra were also measured with the W4f$_{7/2}$ peak used for phase identification purposes. The expected W, W$_2$C, WC$_{1-x}$, and WC peak positions were, respectively, 31.4,[109] 31.8,[108] 31.8,[107] and 32.2 eV.[109] The close spacing of these positions made it difficult to identify the phase with confidence. The peak in the data at 31.5 eV is closest to the literature value for W, but is also very close to $WC_{1-x}$. The 60/40 sample showed a significant amount of $WO_3$ on the surface. This was due to the sample being intentionally oxidized under vacuum and also stored in air for 30 days prior to the XPS analysis being performed. The 50/50 sample was prepared specifically for the XPS analysis and was not intentionally oxidized and only spent about 4 hours in air prior to the analysis. This explains the near absence of $WO_3$ on its surface.

We are currently awaiting XPS data from the majority of the samples discussed in this thesis that should provide additional insight into the structure and response of the films to oxidation.

## Section 5.2 Discussion

The cubic morphology of the 50/50 surface was surprising initially, as the two stable carbides, WC and $W_2C$ both have hexagonal lattices. The cubic morphology can be attributed to the presence of metastable α-W and/or $WC_{1-x}$ phases. Both are cubic and have been observed for magnetron sputtered films at much lower C/W ratios.[47] The presence of an α-W phase seems unlikely since the homogeneity range for interstitial C in the phase is extremely narrow. $WC_{1-x}$ seems much more likely since it is often observed in low temperature thin film depositions.[107,110–112] The C1s spectra presented in Figure 44 agree with the assumption that $WC_{1-x}$ is the dominant, if not the only carbide phase present near the surface of the film. For the 50/50 film, this fact, combined with the observed cubic morphology, means that the cubic carbide is dominant throughout the film. $WC_{1-x}$ is favored due to the epitaxial interaction with the substrate and transformation to one of the hexagonal phases is not observed for film thickness up to 80 nm at least.

If $WC_{1-x}$ is the dominant carbide phase, there is a question of where all of the extra carbon goes. Formation of $WC_{1-x}$ with carbon content as high as 50% has been reported, but for the 60/40 films discussed here there is a question of where the excess carbon resides. On the 80 nm 60/40 film, XPS implies that $WC_{1-x}$ is the only carbide present. If surface graphitization was the only route to segregate excess carbon, one would expect to find >10 nm of graphite on the surface. >20% of the surface is covered with graphene, so clearly much of the carbon goes elsewhere. Since epitaxy is not broken, at least up to a thickness of 30 nm on the 60/40 film based on observed cubic morphology, and the main surface features observed are well-defined ellipsoidal islands, the ellipsoidal islands are likely columnar grains in contact with the MgO substrate and the carbon precipitates at the grain boundaries. The XPS data is not conclusive about what phase the carbon precipitates as, since the C1s peak positions are consistent with graphite, amorphous carbon (a-C), and adventitious carbon due to storing the samples in air for a time.

Since the cubic carbide has been identified as dominant, the spectra in Figure 42 are likely the LDOS at the surface of this carbide. There is significant variation in the LDOS, with both metallic spectra and spectra with a small bandgap being observed. This is not necessarily inconsistent with a single phase, as the $WC_{1-x}$ has a significant homogeneity range, from x = 0 - 0.4.[107] Changes in stoichiometry perturb the bonding configuration and the band structure. So these variations in the LDOS could certainly be consistent with $WC_{1-x}$ with different values of x.

The appearance of graphene, as observed on the 60/40 80 nm sample, from surface segregation of carbon is novel to the literature for transition metals, although the surface segregation of graphite was observed for SiC.[113] The segregation of the graphite from the newly deposited film is consistent with the phase diagram.

# Chapter VI. Oxidation of Codeposited Samples

This chapter is concerned with the changes that occur on the same 50/50, 60/40, and 75/25 films on MgO(100) that were discussed in Chapter V. The discussion will focus mainly on the spectral changes that occur in STS as there were few morphological changes of note after the oxidation. The lack of morphology change is in accord with prior oxidation experiments at RT of W clusters on graphite.

For these experiments the STM was positioned over a single 100x100 nm$^2$ region throughout the oxidation so the changes in a particular group of clusters could be measured directly. For oxidation of W clusters, there was an immediate increase in the apparent volume of the clusters (approximately 29% increase in volume of an initially 80 nm$^3$ cluster after 4.5x10$^{14}$ O$^2$/cm$^2$ exposure). These changes were relatively subtle in the imaging, however, with the appearance of the clusters remaining static despite significant, uniform changes in the diameter and height of the clusters. The apparent change in volume was due to two effects: firstly, the decreased density of the oxide layer (and addition of O atoms) relative to the bare W, and secondly, the reduction in apparent height due to higher tunneling resistance to the oxide. These effects compete in determining the measured volume, and in the early stages of oxidation the former predominated. Later in the oxidation, the apparent volume of the clusters decreased, likely due to evolution of the oxide layer towards the fully oxidized, insulating WO$_3$. The tunneling resistance increases rapidly and overcompensates the true increase in volume due to oxide evolution.

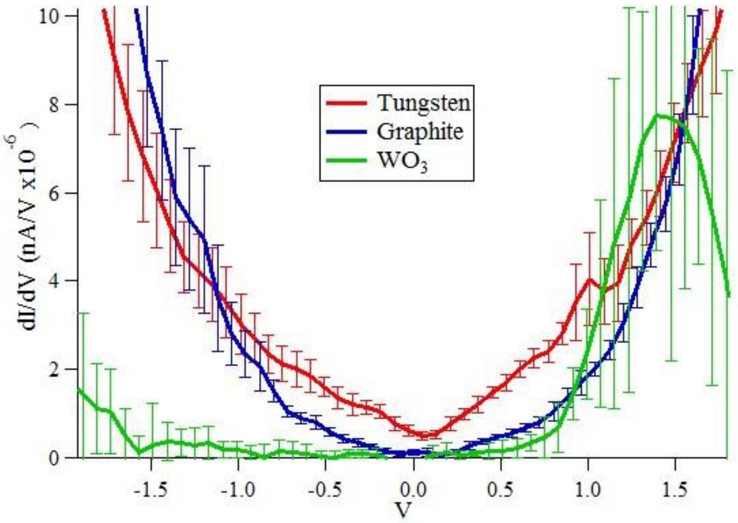

**Figure 45: 2 V, 0.1 nA. Comparison of STS from W and HOPG in same image, along with WO$_3$ taken the following day with the same tip. The differences are subtle and difficult to differentiate for W and HOPG if spectra are taken from different images where tip changes can swamp any differences in the actual LDOS. The WO$_3$ bandgap is easy to identify regardless of changes in the tip or tunneling resistance.**

STS analysis proved much more useful in illuminating the changes that were occurring locally on the W clusters. Prior to oxidation, the differences in

STS between W clusters and the graphite surface was relatively subtle (Figure 45) with W showing a higher LDOS at $E_F$ and a somewhat less parabolic shape. These spectra were taken in the same image with the same $V_b$ and $I_t$.

One issue that arose in performing these experiments was proper selection of STS scan parameters. In the end, a wider scan of >2 V on each side of zero bias seemed to provide more structure in the spectra and therefore more context for making interpretations. The downside of the wider scan is that, for the same current setting, the tunneling current while sweeping through small biases is much smaller for a larger initial voltage, relative to a lower initial voltage, and so structure near zero bias can be obscured by noise. Occasionally, multiple STS maps were measured with different parameters (V and I) on a single surface in close succession and in those cases, no inconsistency was found between the spectral shapes for bias ranges in common (not shown). Future experiments could incorporate this in a more systematic way to instill more confidence that spectral shapes can be generalized to a wide range of tunneling parameters.

Significant changes, especially in the magnitude of dI/dV can occur as a result of changing the tunneling conditions or due to tip changes (atomic reorganization at the tip apex) that were not infrequent. In this regard, the natural evolution towards $WO_3$ under oxidation, for both W and the carbides discussed in this chapter, proved to be a boon in the analysis of surface evolution, since it presents a rather significant modification of the STS spectra and is thus not as susceptible to modification of the tip. Nevertheless, to verify that tip changes were not causing a change in spectral shape, occasionally STS was performed on bare graphite. Changes in spectral shape on HOPG were never observed.

$WO_3$ is a wide bandgap material, with a 2.6 V bulk bandgap[114] that is straightforward to identify in STS measurements of the carbide or W surface. The example shape in Figure 45 following oxidation of W clusters is typical. Much as the bandgap of $C_{60}$ provided a strong contrast with the W in the analysis of $C_{60}$/W interactions, $WO_3$'s bandgap provides the contrast necessary to understand the oxidation experiments.

Table 2 contains a summary of the figures that will be presented to aid in following the sequence of experiments discussed.

**Table 2**

| **Figure #** | **Thickness (nm)** | **Composition (C/W)** | **Oxidation Temperature (˚C)** | **Exposure ($O_2/cm^2$)** |
|---|---|---|---|---|
| **46** | 80 | W | 23 | $8.4x10^{16}$ |
| **47** | 80 | 50/50 | 300 | $3.3\ x10^{16}$ |
| **48** | 30 | 60/40 | 300 | $3.3\ x10^{16}$ |
| **50** | 30 | 50/50 | 300 | $3.3\ x10^{16}$ |
| **51** | 30 | 50/50 | 600 | $4.95\ x10^{16}$ |
| **52** | 30 | 60/40 | 400 | $3.3x10^{15}$ |
| **53** | 30 | 60/40 | 600 | $4.95\ x10^{16}$ |
| **55** | 30 | 60/40 | - | - |

An overview of the oxidation of W clusters on graphite provides useful background in understanding the results of the carbide oxidation. For the experiment visualized in Figure 46, 6 ML of W were deposited on HOPG and exposed to $1x10^{-9}$ mbar of $O_2$ for 217 min at RT for a total $O_2$ coverage of $8.4x10^{16}$ $O_2/cm^2$ presuming a sticking coefficient of 1. This exposure is equivalent to around 100 ML of $O_2$. The resulting STS map, Figure 46a, was taken at -1.02 V where contrast between the $WO_3$ and W spectra is large. Red areas have a small dI/dV and blue/violet areas have a large dI/dV. It is important to realize that the color scale is set to maximize contrast and is changed for each image presented in the next few figures.

Figure 46 shows several aspects of the oxidation process on this surface. The spectral shapes in Regions A-C demonstrate that many areas on the surface have almost fully oxidized to $WO_3$, with a bandgap of about 1.5 V and the LDOS severely reduced between -1.5 and 1.0 V, which is approximately the same as the bandgap for the bulk $WO_3$. The full bulk bandgap is typically not observed due to a high density of surface states that are characteristic of $WO_3$ surfaces.[115]

The $WO_3$ regions occur in localized islands so this could be indicative of nucleation and growth of the fully oxidized regions, which is not unexpected since the transition to $WO_3$ is accompanied by a structural change from the underlying W. There are also areas where oxidation has led to an intermediate state between W and $WO_3$, such as Regions E and F. The spectra from these areas are characterized by a reduction in dI/dV at $E_F$ such that these areas are

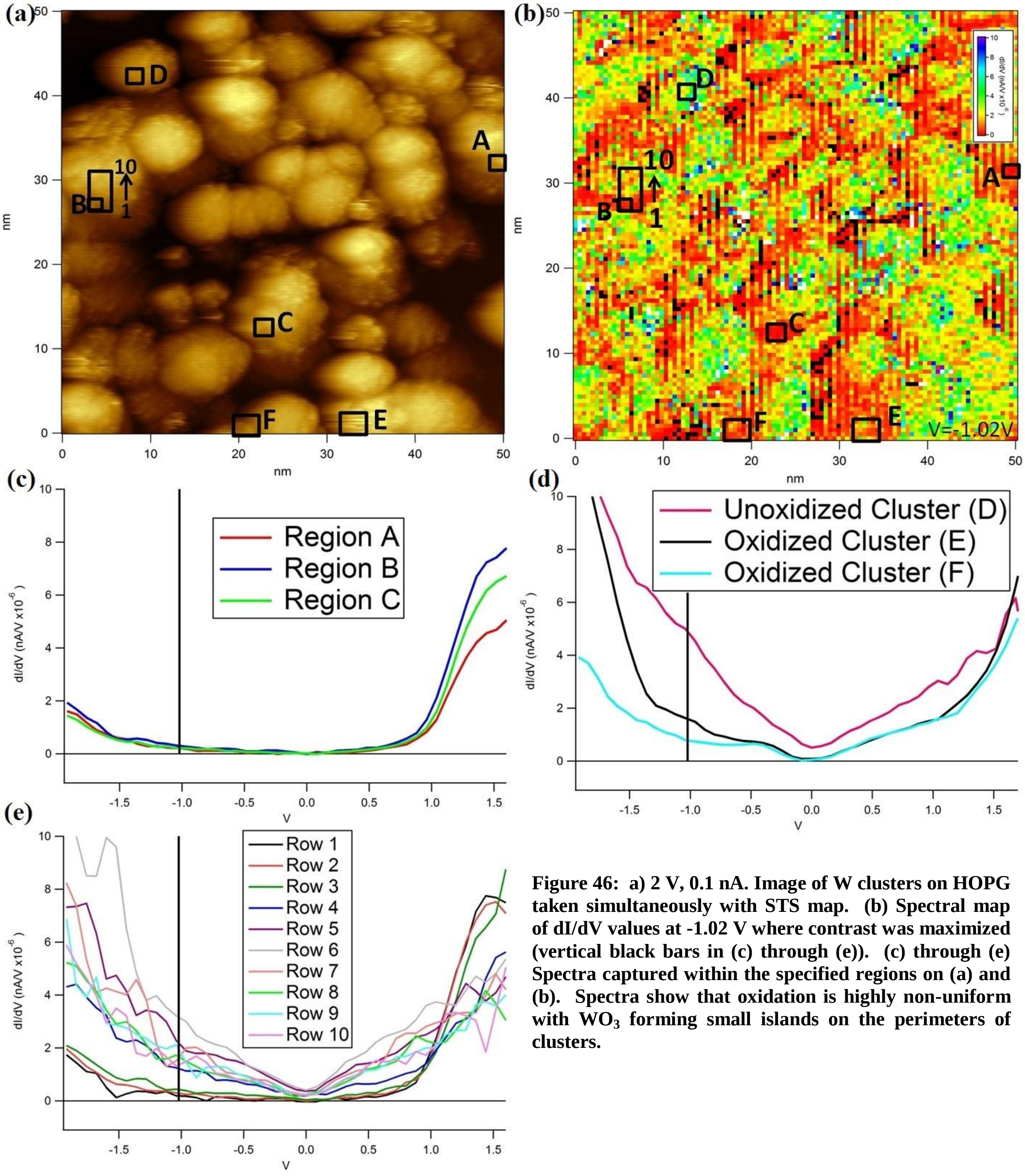

**Figure 46: a) 2 V, 0.1 nA. Image of W clusters on HOPG taken simultaneously with STS map. (b) Spectral map of dI/dV values at -1.02 V where contrast was maximized (vertical black bars in (c) through (e)). (c) through (e) Spectra captured within the specified regions on (a) and (b). Spectra show that oxidation is highly non-uniform with $WO_3$ forming small islands on the perimeters of clusters.**

either semimetallic like graphite or have a very narrow bandgap. $WO_2$ has been measured to have a smaller, but still metallic DOS at $E_F$ relative to metallic W via XPS,[116] and so this is a likely candidate for these regions. Mixed $W_xO_y$ materials do exist, but there is some debate about whether these represent independent structures or just defective $WO_2$ and $WO_3$ structures.[117,118] In this case, these non-stoichiometric oxides could be relevant since the surface might evolve towards the stable oxides in a number of steps that might account for the intermediate spectra shapes.

Figure 46e shows the evolution of the band structure across a boundary between a fully oxidized area (Row 1-3) and a very metallic region (Rows 4-10) near the coordinates (5 nm, 30 nm) in the image. Each “Row” is composed of 10 spectra with the same x-coordinate and consecutive y-coordinates that have been averaged together. This graph shows that there is a very abrupt change in the LDOS between Rows 3 and 4 which are spatially separated by 5 Å. The LDOS shape approached that of W in Rows 5 and 6 before passing back into a region of intermediate oxide in Rows 7-10. Morphologically, there are no changes in the cluster images other than the uniform dimensional changes discussed earlier.

## Section 6.1: Oxidation of Codeposited Carbide Samples

Controlled oxidation in UHV was performed on all of the codeposited carbide samples on MgO(100) discussed in the last chapter, 50/50, 60/40, and 75/25, with subsequent characterization performed by STM and STS.

The 50/50 80 nm surface was subjected to $1x10^{-7}$ mbar of $O_2$ for 20 min for a total dose of $3.3x10^{16}$ $O_2/cm^2$ with the substrate held at a constant temperature of 300˚C. The morphology of the surface at large scales was indistinguishable from the preoxidation surface discussed in Section 5.1. Atomic resolution on the post-oxidation surface was never obtained.

Figure 47 shows a region of characteristic ellipsoidal islands as they are observed on the 50/50 80 nm surface. These islands are the smallest morphologically distinct features on the surface. From the spectra in Figure 47c-e it can be seen that the degree of oxidation is quite uniform throughout the surface with spectra characterized by a highly asymmetric shape, a small or near-bandgap at $E_F$ and a small inflection to more negative slopes at a small negative bias. The spectra are quite different from the carbide dI/dV found in Figure 42, which possess a shoulder at small negative bias. The spectra are also clearly distinct from the intermediate oxidation seen in Figure 46d,e which show a much sharper v-shape near $E_F$. This could be due to the different reaction pathways that must be followed to remove C atoms from the lattice prior to the formation of $WO_2$ or $WO_3$. For example[119]:

$$WC + O_2 \rightarrow WO_2 + C$$

Mixed oxy-carbides may also form.

The carbon is eventually removed via further reactions that produce CO and $CO_2$, but the

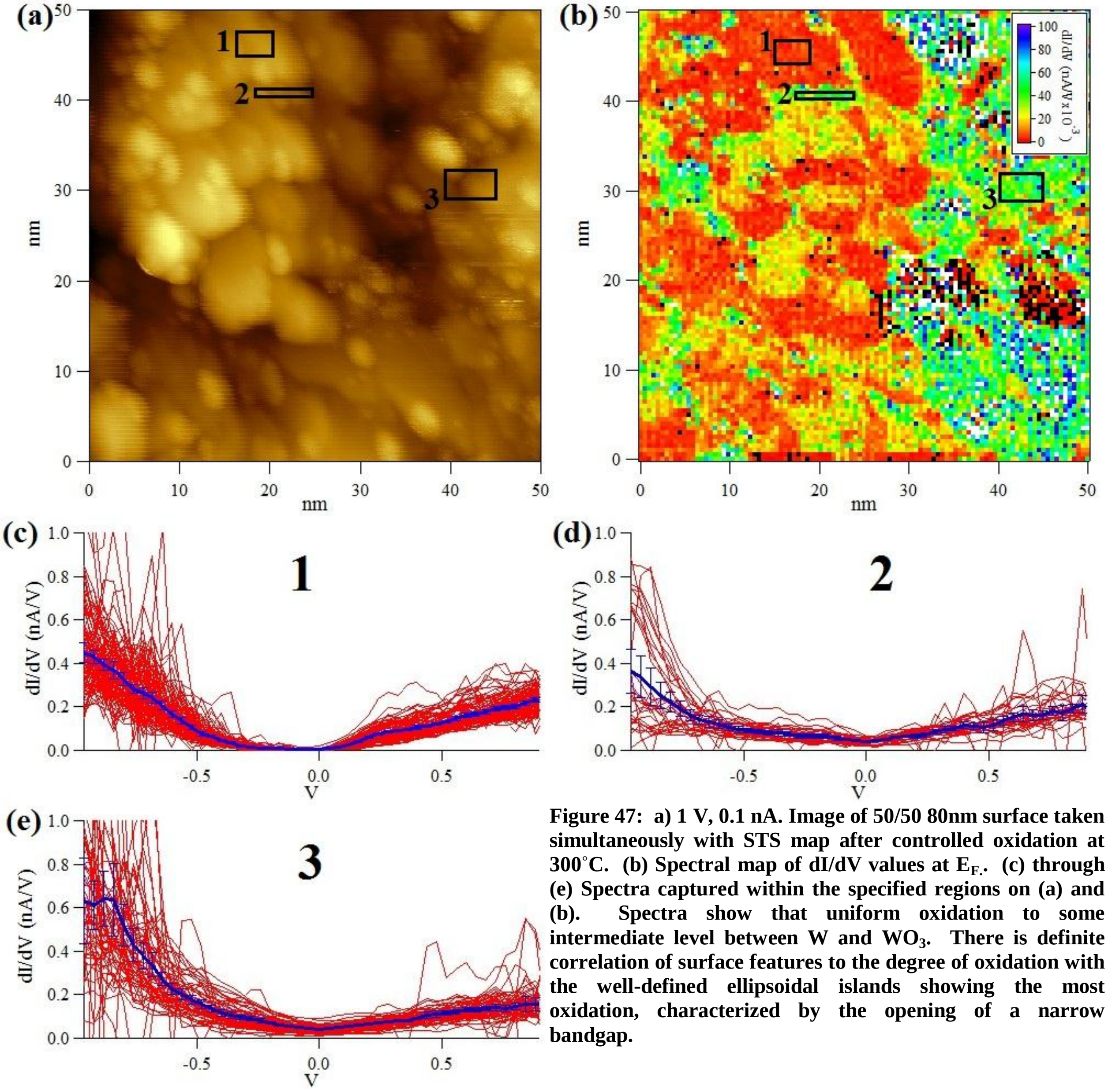

**Figure 47: a) 1 V, 0.1 nA. Image of 50/50 80nm surface taken simultaneously with STS map after controlled oxidation at 300˚C. (b) Spectral map of dI/dV values at $E_F$. (c) through (e) Spectra captured within the specified regions on (a) and (b). Spectra show that uniform oxidation to some intermediate level between W and $WO_3$. There is definite correlation of surface features to the degree of oxidation with the well-defined ellipsoidal islands showing the most oxidation, characterized by the opening of a narrow bandgap.**

temporary presence of unbonded surface C or mixed oxy-carbides could produce the changes to these spectra.

The degree of oxidation, characterized by the presence of and/or the width of a bandgap, shows a strong dependence on the local morphology. The well-defined ellipsoidal islands on the left hand side of the image showed the most advanced oxidation. Oxidation seemed to be relatively uniform within a single island or cluster. Notably, unlike in the case of the W oxidation, all areas are oxidized to some extent and the original surface is not retained. The surface oxidation does not fully progress to $WO_3$ anywhere and the variation in presence and/or width of bandgaps within a small region of the surface is indicative of intermediate and mixed surface termination.

The 60/40 80 nm surface was exposed to identical oxidation conditions as the 50/50 80

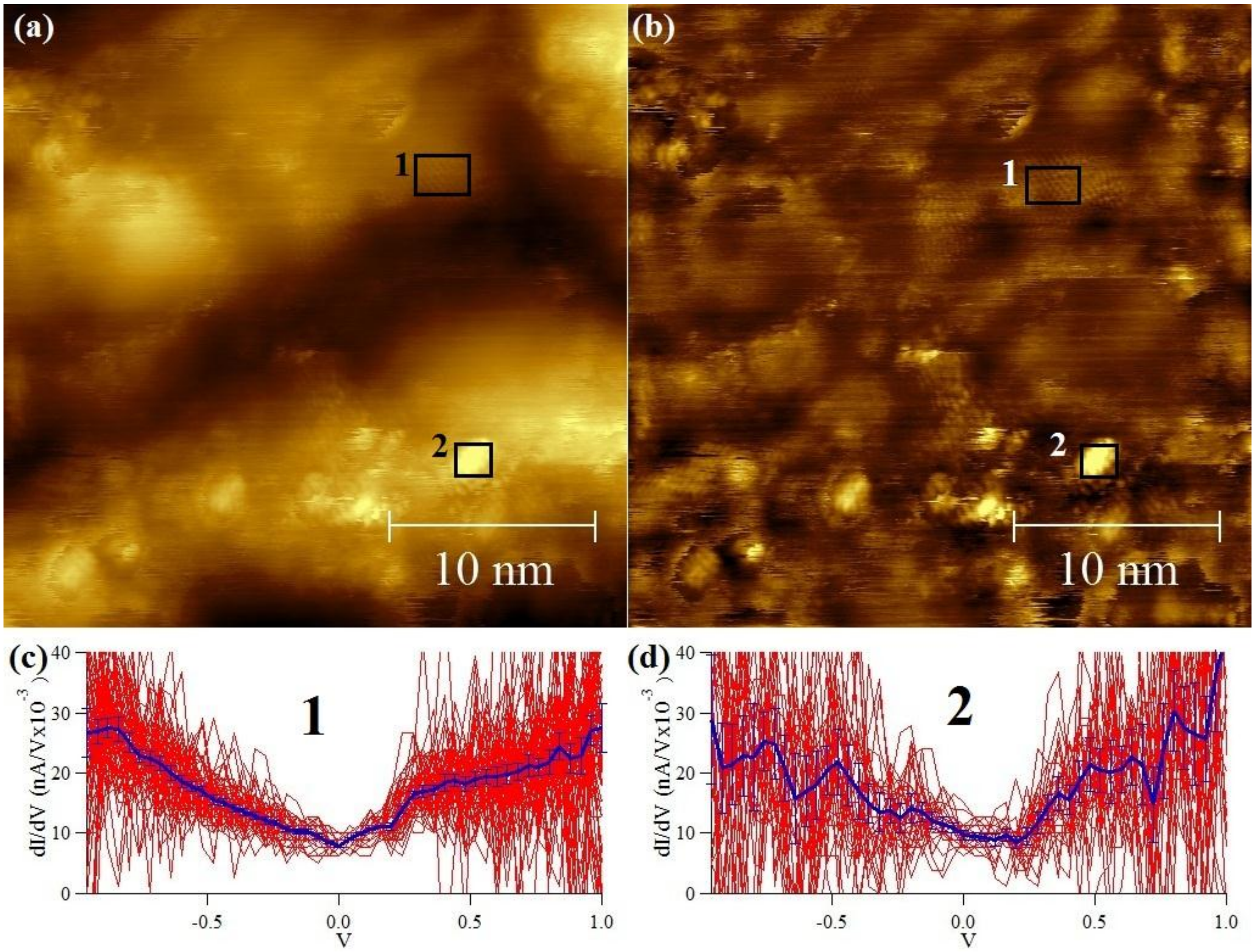

**Figure 48: a) $V_b = 0.5$ V, $I_t = 20$ nA, image of post-oxidation 60/40 80 nm surface with atomic resolution on graphene as well as the striped structures discussed for the pre-oxidation surface. b) Same image as (a) with 12-degree polynomial background subtraction to enhance the contrast on the atomic scale features. (c)-(d) Spectra obtained from regions 1 and 2. Region 1 is graphene and displays a Dirac point at $E_F$. Region 2 displays a more graphite-like shape near $E_F$ but the spectra are quite noisy.**

nm surface. The resulting surface morphology was again indistinguishable from the pre-oxidation images. In this case, however, atomic resolution was attained in some regions of the surface. Figure 48 shows a region where graphene is resolved, confirmed again by a 3.35 Å ring center-to-center distance, as well as the striped clusters that were discussed in the pre-oxidation chapter (Figure 43) and identified as graphite. The atomic-scale features observed are fully consistent with those observed for the pre-oxidation.

The STS spectra from Figure 48, which were collected with $V_b$=1.0 V and $I_t$=1.5 nA, are also similar to the pre-oxidation spectra (Figure 43). Region 1 contains graphene, confirmed by measuring the ring center-to-center distance, and the STS shows a Dirac point at $E_F$ which is a linear approach to the DOS minimum and a discontinuity in the slope at that minimum. This is consistent with the theoretical DOS for graphene except that there should be dI/dV=0 at the Dirac point. The striped feature in Region 2 has a similar LDOS to its pre-oxidation counterpart, albeit the spectra were rather noisy in this area. The modification of the surface in response to $O_2$ exposure is minimal, both with respect to topography and dI/dV spectroscopy data. The bandgap opening, which is characteristic of oxidation on the carbide as well as the W surface, is not observed here, and the graphite surface largely remains stable.

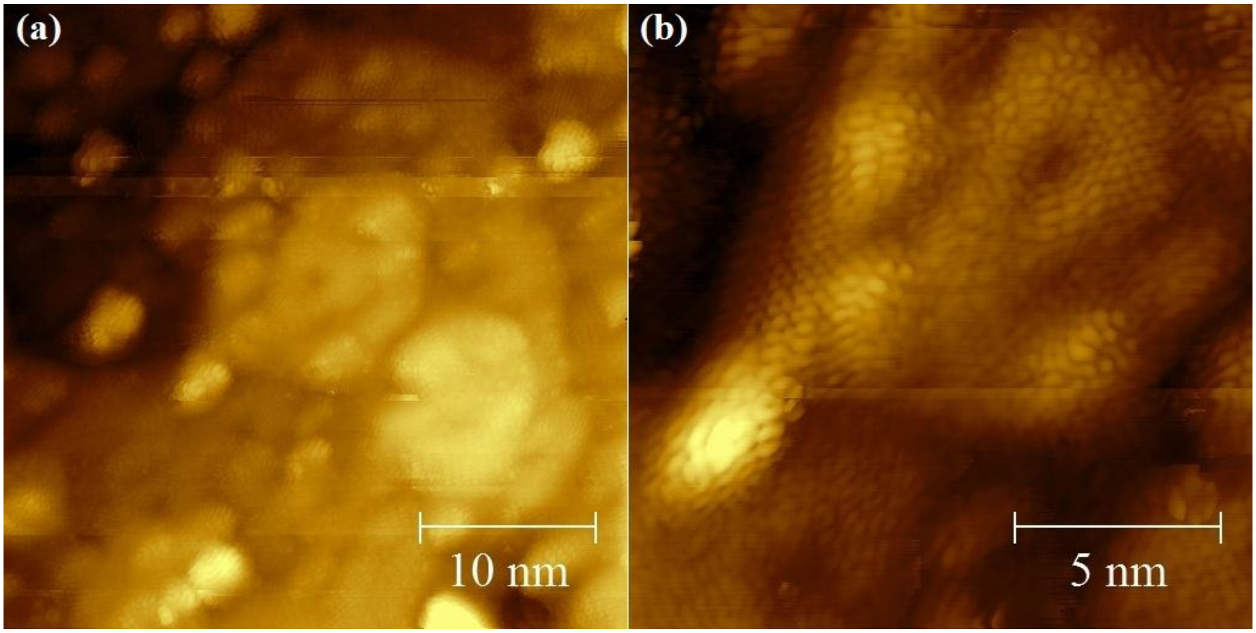

**Figure 49: $V_b$ = 0.05 V, $I_t$ = 2 nA. a) Image of 75/25 80 nm post-oxidation surface showing how heavily graphitized the entire surface remains. b) Central region of (a). Demonstrates the formation of the striped domains from graphite.**

A number of STS maps were produced for the 60/40 80 nm post-oxidation surface. All of these maps showed similar phenomenon to what is shown in Figure 48. Features associated with carbide, topographic or spectroscopic, were never observed.

The 75/25 80 nm surface was exposed to identical oxidation conditions as the other two surfaces. All imaging and spectroscopy indicated the entire surface remained heavily graphitized, in agreement with the 60/40 sample. Figure 49 shows one representative region.

The 30 nm thick films (50/50 and 60/40) discussed earlier were also oxidized to investigate their response. These films, however, were exposed to more severe conditions than the 80 nm films with respect to $O_2$ dose and temperature.

The 30 nm 50/50 film was initially oxidized under identical conditions to the 80 nm 50/50 (and 60/40) film for a dose of $3.3 \times 10^{16}$ $O_2/cm^2$ at 300˚C. This surface showed a slightly

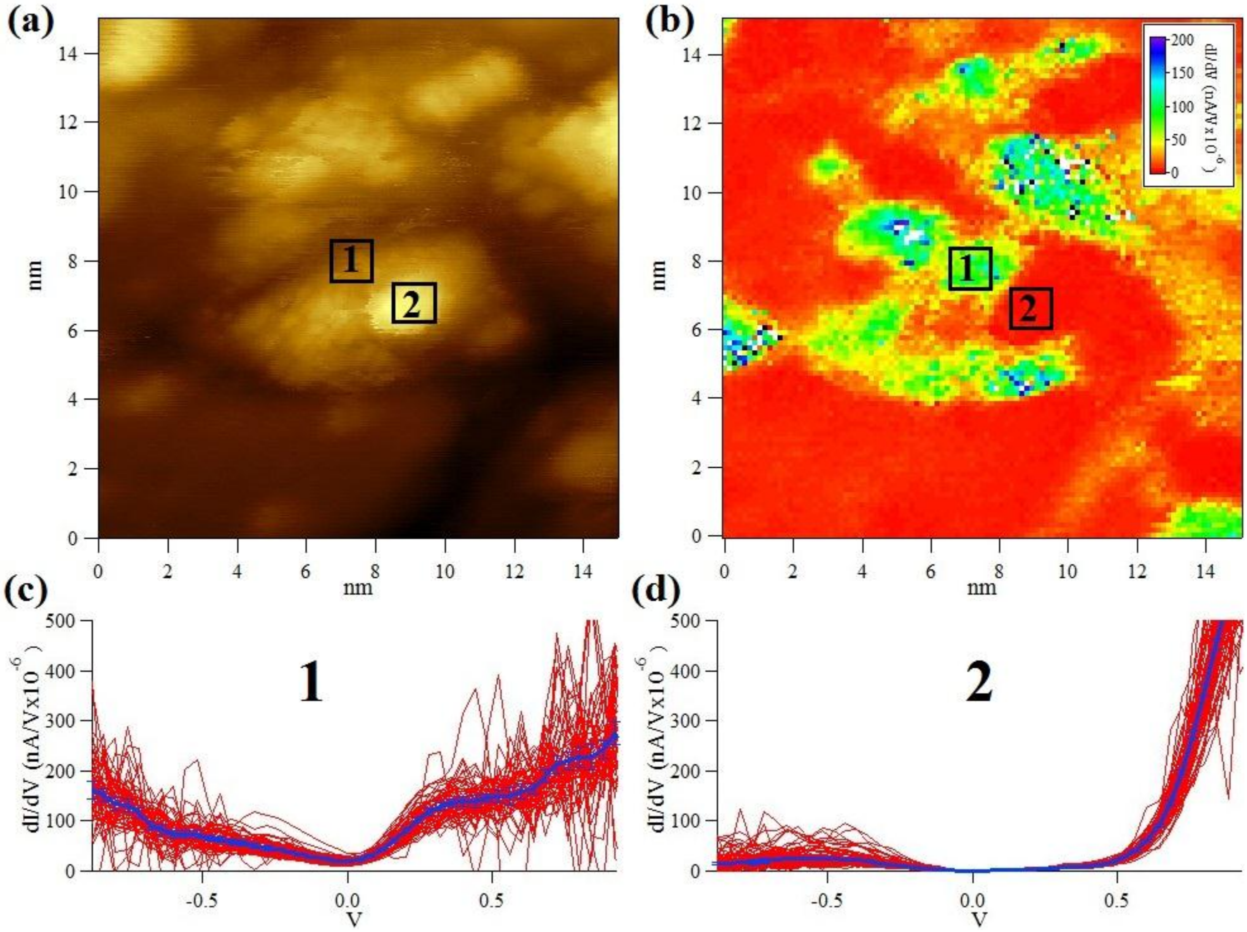

**Figure 50: (a) 1 V, 1.5 nA. Image of region composed of ellipsoidal islands on the 50/50 30 nm thick film after 300˚C oxidation. (b) Spectral map of dI/dV values at $E_F$ captured simultaneously with (a). (c) and (d) Spectra captured within areas 1 and 2, respectively. Region 1 is composed of lightly oxidized carbide whereas Region 2 has oxidized almost completely to $WO_3$.**

more extensive degree of oxidation owing most likely to a certain degree of inherent surface inhomogeneity. The oxidation continues to be highly non-uniform, with areas of nearly pristine carbide existing within 1 nm of surfaces showing uniform and extensive oxidation, as illustrated in Figure 50. Region 1 has a very similar spectral shape to the carbides presented in Figure 42, with the only difference that the shoulder between -0.5 and 0 V disappearing after oxidation. This is consistent with the evolution towards $WO_3$ observed thus far for all surfaces, with the LDOS for the occupied states (negative voltage) being generally lower than the empty state LDOS, which corresponds to positive bias voltages. Region 2 has opened an ~1 V bandgap and all polarities within the $WO_3$ bulk bandgap show severely depressed LDOS.

The 30 nm 50/50 film was then exposed to a much more extensive oxidation, 30 min at $1\text{x}10^{-7}$ mbar with the film held at 600˚C for a dose of $4.95\text{x}10^{16}$ $O_2/cm^2$; or $8.25\text{x}10^{16}$ $O_2/cm^2$ including the prior oxidation at 300˚C. A representative area of the resulting film is shown in

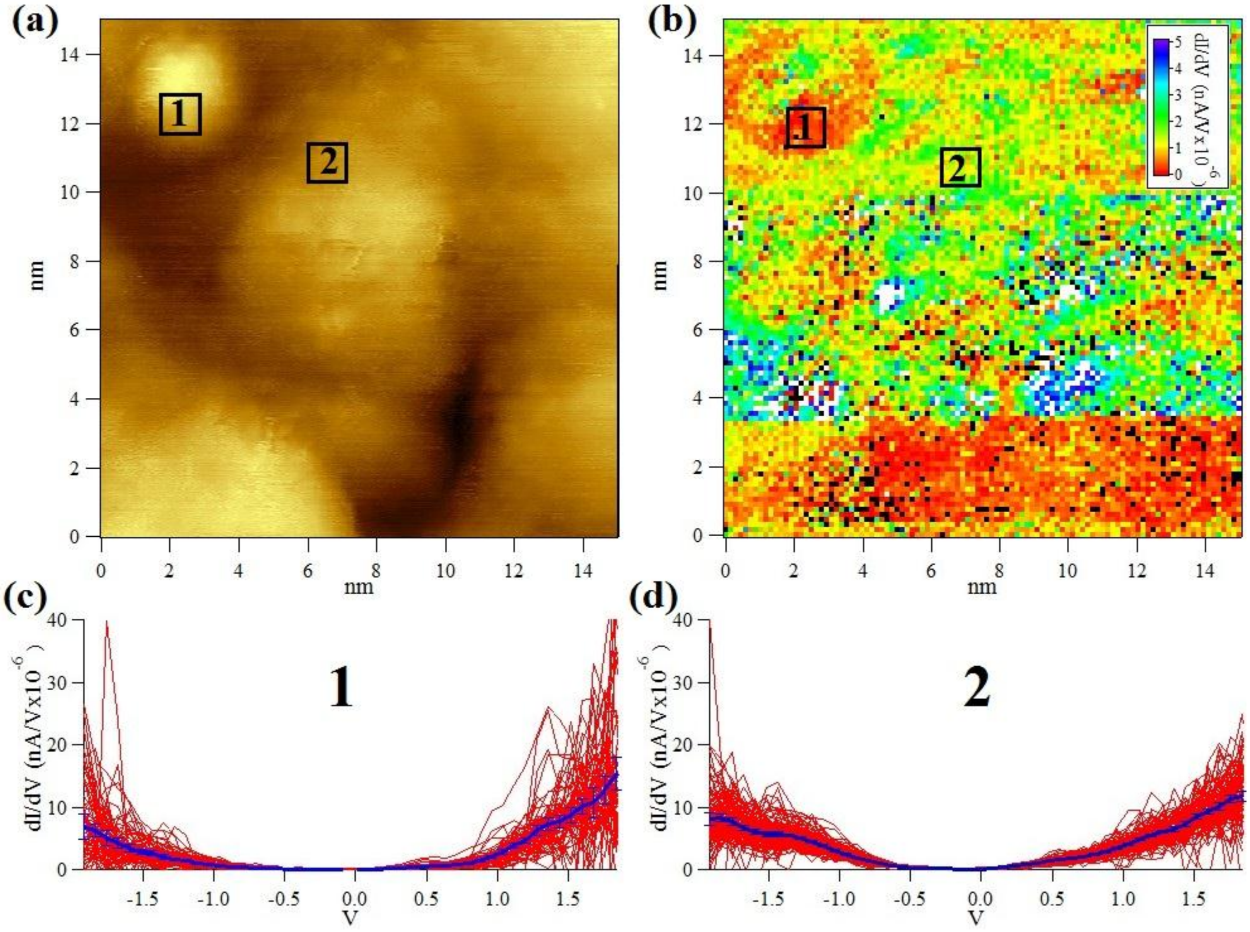

**Figure 51: (a) 2 V, 0.1 nA. Image of region composed of ellipsoidal islands on the 50/50 30 nm thick film after 600˚C oxidation. (b) Spectral map of dI/dV values at -0.5 V in region (a). (c) and (d) Spectra captured within areas 1 and 2, respectively. Both regions have oxidized significantly. Region 1 shows similar dI/dV to previous spectra attributed to $WO_3$. Region 2 is also quite oxidized but with a much smaller bandgap.**

Figure 51. Region 1 is oxidized to a full 1.5 V bandgap with a strong depression in LDOS between -1.5 and 1.0 V. Region 2 is at an intermediate stage of oxidation with a somewhat smaller bandgap. This film differs from the more mildly oxidized one in that no areas were found that had not oxidized to the point of opening a bandgap. This is also the reason the $WO_3$ islands on the STS map stand out less prominently from a visual point of view as compared to Figure 50.

Morphologically, in keeping with prior oxidation results, no changes to the surface were found, aside from the need to image at higher voltages to stay out of the bandgap region and thus have a sufficient tunneling current.

The 30 nm 60/40 film was exposed to $1x10^{-8}$ mbar of $O_2$ at 400˚C for 20 min for a total

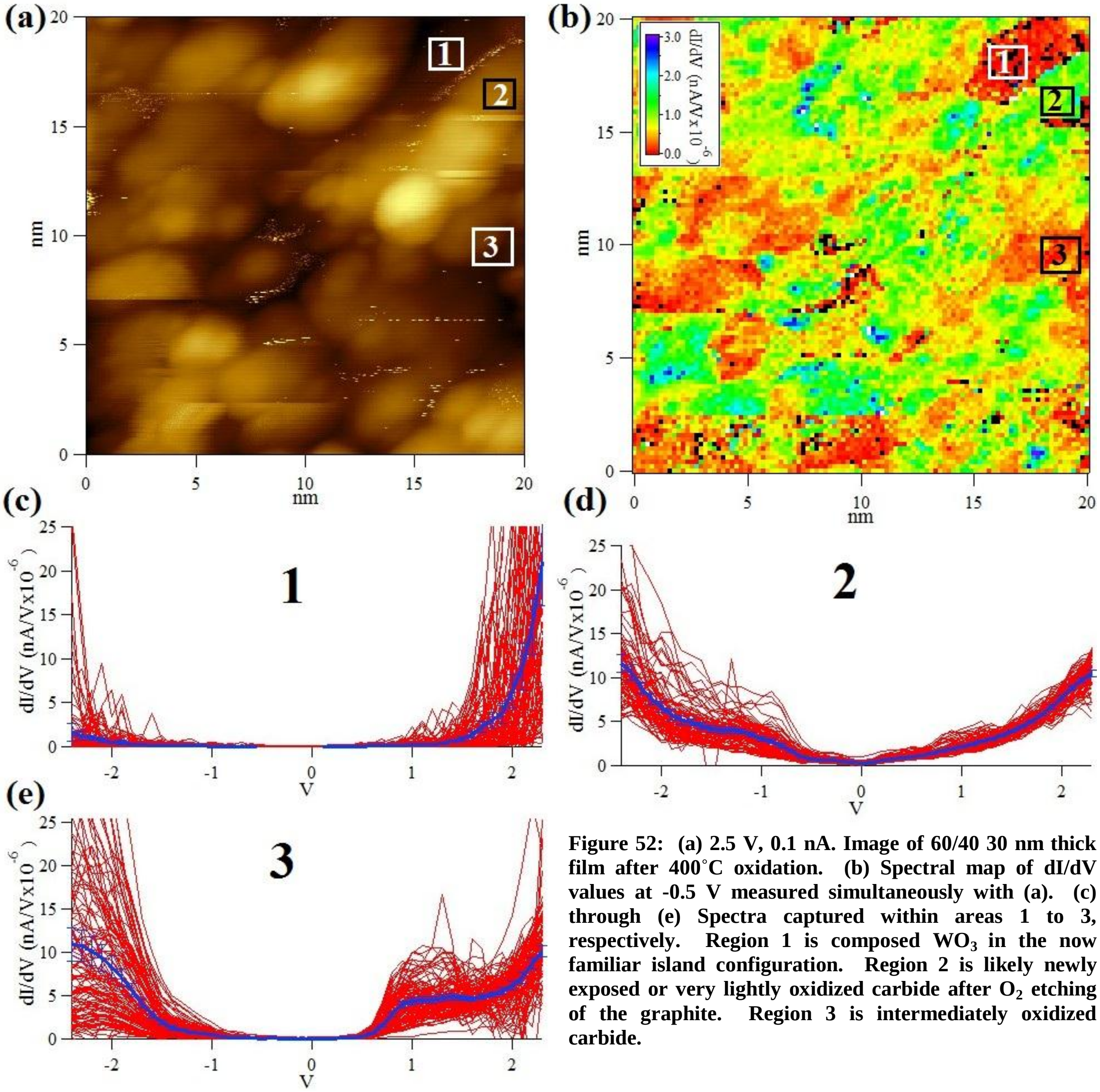

**Figure 52: (a) 2.5 V, 0.1 nA. Image of 60/40 30 nm thick film after 400˚C oxidation. (b) Spectral map of dI/dV values at -0.5 V measured simultaneously with (a). (c) through (e) Spectra captured within areas 1 to 3, respectively. Region 1 is composed $WO_3$ in the now familiar island configuration. Region 2 is likely newly exposed or very lightly oxidized carbide after $O_2$ etching of the graphite. Region 3 is intermediately oxidized carbide.**

dose of $3.3\text{x}10^{\mathbf{15}}$ $O_2/cm^3$. The resulting film showed unstable imaging for conditions that yielded atomic resolution on the pre-oxidation surface (<0.1 V, >1 nA). This limits conclusions that can be drawn about morphology. The images that were taken, at higher voltages to stay out of the bandgap of the $WO_3$ regions, showed identical morphology to the pre-oxidation images.

Figure 52 shows an STS map taken on the post-oxidation 60/40 surface. It is characterized by regions with fairly pristine carbide, well-defined islands of $WO_3$, and islands of incompletely oxidized carbides. The dI/dV of the $WO_3$ in Region 1 closely approximates the measured bulk bandgap of 2.6 V. Region 2 has a parabolic shape like graphite, but the shoulder near -1 V and the general asymmetry is characteristic of the lightly oxidized 50/50 film in Region 2 of Figure 51.

Region 3 is also an oxide, but distinct from the one in Region 2. This differentiation shows the utility of the wider range of voltages explored on this surface.

Recall that the 60/40 80 nm pre-oxidation surface was predominantly, if not exclusively, graphitized, and that the 80 nm 60/40 film remained fully graphitized after the 300˚C oxidation. The pre-oxidation 60/40 30 nm surface had a low coverage of graphite (<10%), but after the 400˚C oxidation with an order of magnitude less $O_2$ exposure than the 80 nm surface was exposed to, this surface is denuded of graphite. This shows that the $O_2$ exposure at elevated temperatures etches away the graphite. It also implies that there is a possible increase in the rate of etching for 400 vs. 300˚C. Since the 30 nm 60/40 surface had a lower coverage of graphite to begin with, this conclusion is somewhat speculative, but a significant fraction of the 60/40 80 nm surface was covered with graphene, and this remained the case after the oxidation with no exposed carbide found, so there is reason to believe that graphite etching was minimal for the 300˚C oxidation. Etching of the 30 nm surface at 400˚C also explains why a larger fraction of this surface showed insufficient oxidation to open a bandgap (the green areas in Figure 52b) relative to the 50/50 surface oxidized at a lower temperature (green areas in Figure 50b). Some fraction of the carbide was protected from oxidation by graphite until being exposed by graphite removal through etching at some late stage of the $O_2$ exposure.

Another 60/40 30 nm sample was oxidized at 600˚C at 1x10$^{-7}$ mbar $O_2$ for 30 min for a total dose of 4.95x10$^{16}$ $O_2$/cm$^3$. Despite the need to etch away some graphite before oxidation of the carbide could begin, this surface was overwhelmingly dominated by $WO_3$. Figure 53 shows the STS map of a representative region. All areas have a $WO_3$-like bandgap. This surface also seems to have a more uniformly $WO_3$ surface than the 50/50 30 nm surface that was equivalently oxidized, Figure 51. The reasons for this difference remain unclear.

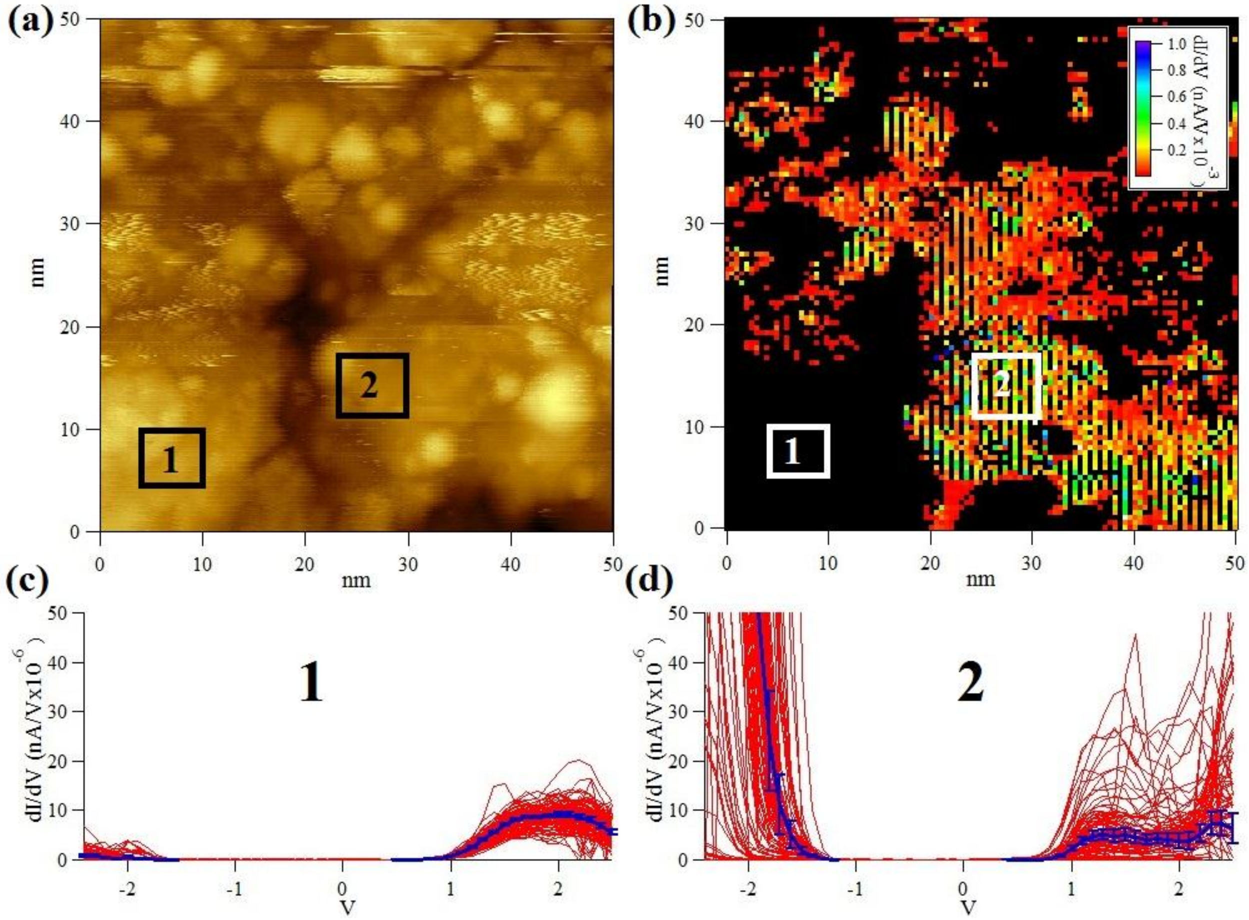

**Figure 53: (a) 2.5 V, 0.1 nA. Image of 60/40 30 nm thick film after 600˚C oxidation. (b) Spectral map of dI/dV values at -2.2 V measured simultaneously with (a). (c) and (d) Spectra captured within areas 1 and 2, respectively. Both areas have a bandgap characteristic of $WO_3$, but dI/dV rises much more at negative polarity outside the bandgap for Region 2.**

There is a clear delineation, however, between two regions of the surface. Region 2 has a consistently large rise in dI/dV at negative polarity outside the bandgap, relative to Region 1. This could be due to some sort of instability in the measurement. Many measurements during this experiment were quite noisy and had vertical stripes of differing dI/dV magnitude like those visible in the colored regions of Figure 53b. These variations do not correlate to surface features and must originate within the experimental apparatus. A vacuum issue required running the turbomolecular pump during these measurements, causing a larger than normal vibration of the instrument which could certainly be the culprit.

Nevertheless, the differences between Regions 1 and 2 do correlate to surface features and therefore the differences likely arise from the surface structure. It is possible that this variation could be due to the thickness of the $WO_3$ layer. Taking a simple model where the potential within the oxide is constant and similar to that of vacuum in the absence of an applied voltage, at negative polarity electrons tunnel from the surface to the tip leaving holes in the valence band of the insulator, Figure 54a. To refill these valence states, electrons in the conduction band of the carbide must tunnel through the oxide to the (now-depleted) valence state of the surface oxide atoms. For certain very small oxide thicknesses the tunneling from the carbide happens much faster than the tunneling to the tip and so the dI/dV is relatively unaffected. For larger oxide thicknesses, the tunneling from the carbide to the depleted valence states will become the rate limiting step. This could be what is occurring in Figure 53 with Region 1 having a greater oxide thickness than Region 2.

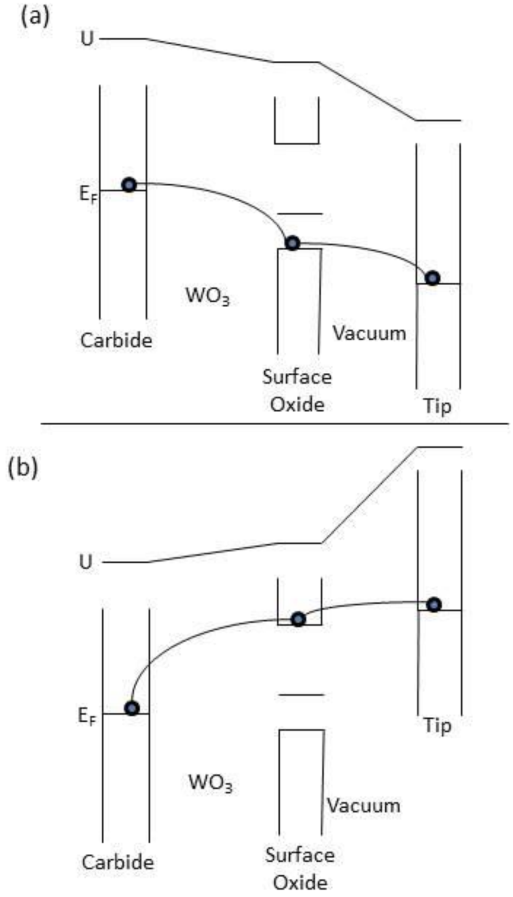

**Figure 54: Model of phenomenon in Figure 53 for negative bias (a) and positive bias (b). a) When tunneling from carbide to surface oxide is slower than tunneling from surface oxide to tip, depression of dI/dV occurs. b) Larger bias or thicker oxide required for tunneling from surface oxide to carbide to be rate limiting since the large bandgap ensures $\Delta V$ between surface oxide and carbide will be large.**

This raises a question about the lack of a similar effect at positive voltages. After all, there would still be two tunnel junction when measuring the empty states of the oxide but Region 1 and 2 show similar dI/dV here. In this case, Figure 54b, the voltage difference between the bottom of the oxide conduction band and $E_F$ of the carbide-oxide interface, the two relevant states at positive bias, remains much larger than the potential difference between $E_F$ of the carbide-oxide interface and the top of the valence band of the oxide at the surface, the two relevant states at negative bias. Perhaps this explains why tunneling through the oxide has not become the rate limiting step for Region 1 at positive bias. Differences in the way electrons and holes are transported through the oxide as well as defect or surface states that sit near the conduction band are two other possible explanations for why dI/dV is not suppressed for the thicker oxide at positive bias.

To evaluate the stability of the now oxide-covered films, a central concern when considering WC as a catalysis material, we performed a thermal treatment in UHV on the 60/40 30 nm film. To start, recall that the 60/40 30 nm film oxidized at 600˚C was uniformly covered with $WO_3$. This film was then annealed for 2 hr at 600˚C in UHV. The resulting morphology was similar to all prior images of this film. The STS on the surface changes considerably,

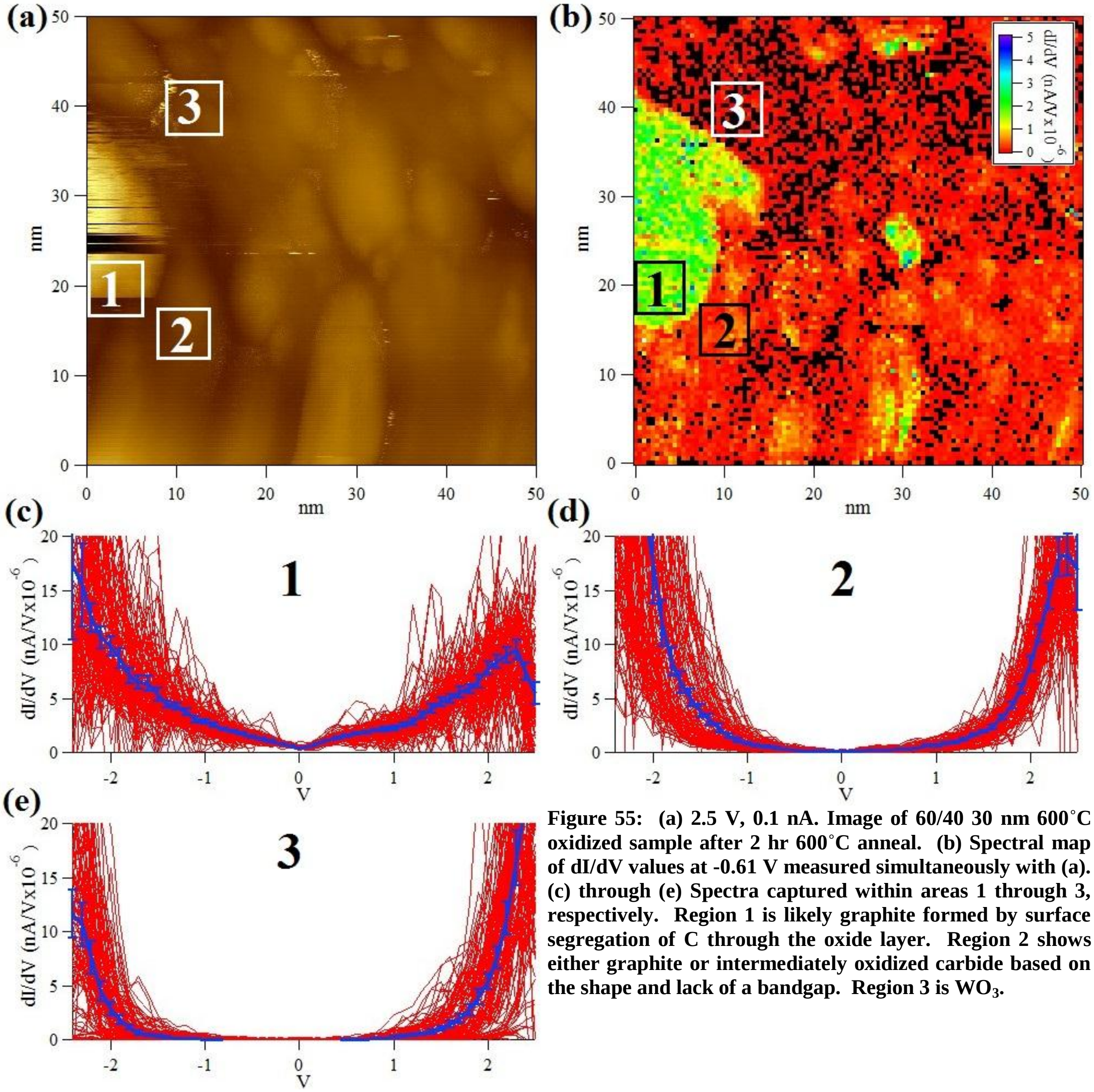

**Figure 55: (a) 2.5 V, 0.1 nA. Image of 60/40 30 nm 600˚C oxidized sample after 2 hr 600˚C anneal. (b) Spectral map of dI/dV values at -0.61 V measured simultaneously with (a). (c) through (e) Spectra captured within areas 1 through 3, respectively. Region 1 is likely graphite formed by surface segregation of C through the oxide layer. Region 2 shows either graphite or intermediately oxidized carbide based on the shape and lack of a bandgap. Region 3 is $WO_3$.**

however. Figure 55 shows a representative region of the surface with a mobile cluster on the left and a group of islands. Region 1 is likely graphene because of the discontinuity in $d^2I/dV^2$ at $E_F$. Region 2 is probably graphite based on the symmetry, parabolic shape, and lack of a bandgap. The LDOS never actually reaches zero so there is no bandgap in this region. Region 3 is $WO_3$, but notably, dI/dV rises outside of the bandgap region much more significantly on both sides of $E_F$ than before the anneal, Figure 53. These results indicate that high temperature annealing of the heavily oxidized film causes a graphitization of the surface and, possibly, some decrease in the oxide thickness based on the way dI/dV is no longer suppressed outside the $WO_3$ bandgap.

## Section 6.2: Discussion

Overall, the oxidation of the carbide samples showed some commonality with the oxidation of pristine W clusters on HOPG, Figure 46. STS spectra showing the signature of the $WO_3$ tended to evolve in isolated and well-defined islands that grow in size with increasing $O_2$ exposure and/or oxidation temperature, e.g. Figure 50 vs. Figure 53, before likely growing in thickness to such an extent that it might be responsible for the depression of the tunneling current to the sample, e.g. Region 1 vs. 2 of Figure 53. The nucleation and growth of $WO_3$ islands had been observed previously in Thermogravimetric (TG) analysis of WC exposed to flowing air at different heating rates and the determination of appropriate kinetic parameters.[119]

The incomplete oxidation to $WO_{3-x}$, $0<x<3$, occurs in a more uniform manner across the entire surface of the sample early in the oxidation process, exemplified by the comparison between the pre-oxidation STS (Figure 42) and STS taken immediately after the mildest oxidation performed (Figure 50). Intermediate oxidation steps ($WO_{3-x}$, $0<x<3$ or oxy-carbides) were not found in Ref. 125. This is likely due to the relatively low $O_2$ partial pressures in our experiments or because the study in Ref. 125 used the hexagonal WC, not the cubic $WC_{1-x}$ that is most likely present here. Our analysis delivers a mesoscopic view of the oxidation process – the initial steps of oxidation: adsorption, dissociation, and incorporation of O atoms into the surface structure will require a study which focuses on atomic resolution STM on well-defined surfaces of various carbides with $O_2$ coverages limited to well below one ML equivalent.

For oxidation of graphite covered surfaces such as the 60/40 and 75/25 samples, oxidation at high temperatures etches the graphite layers away. The etching of graphite in $O_2$ at elevated temperatures has been studied, again by TG analysis, with onset of oxidation around 400˚C.[120] This agrees well with our results as there was no evidence of etching for 60/40 80 nm after the 300˚C oxidation (Figure 48), whereas the low initial coverage of graphite on the 60/40 30 nm surface is removed completely after a similar oxidation at 400˚C (Figure 52).

One clear observation from these experiments is that pristine W clusters oxidize much more rapidly than the carbide films studied here. The W surface of Figure 46 has widespread but small $WO_3$ islands despite oxidation at RT. A carbide surface exposed to the same order of magnitude of $O_2$ coverage but oxidized at 300˚C has no $WO_3$ islands nucleated on its surface and is dominated by intermediate oxides and oxy-carbides. Apart from the surface chemistry, it is also necessary to take the surface morphology into account. The two surface morphologies are not equivalent. The surface of the WC films are much flatter than the cluster covered surface. If the rate of oxidation depends on site-specific nucleation of $WO_3$, then the greater variety and density of reaction sites on the outside of round metallic clusters relative to a nearly flat, likely epitaxial film, makes a direct comparison of oxidation rates problematic.

# Chapter VII: Conclusions

In the course of this investigation, we set out to examine the interactions between W and $C_{60}$ leading to an understanding of the processes at work when high temperatures are applied to synthesize a carbide surface. These composition-controlled films were then examined to determine their properties. Finally, the films were subjected to oxidation at elevated temperatures to examine their response and see if insights could be gained that may allow the engineering of such surfaces to minimize their susceptibility to oxidation.

To start, films of W and $C_{60}$ were deposited on graphite at RT in various sequences and the resulting surfaces characterized by STM and STS. It was found that W on graphite grows into clusters in accordance with a liquid drop mechanism before transitioning to agglomeration of these small clusters. Interactions between these agglomerations of W and $C_{60}$ were found to be strangely weak considering the literature which concludes that the attractive interaction between W and $C_{60}$ is quite strong.

When $C_{60}$ was deposited onto the graphite before W, the surface corrugation of $C_{60}$ inhibited the diffusion of W atoms on the surface and led to a unique monotonically decreasing distribution of measured cluster sizes. This distribution was found to be appropriate for a theoretical mechanism of cluster growth that requires an initially increasing mobility of the W clusters with increasing size. To justify this highly non-intuitive and unique to the experimental literature conclusion, an explanation involving decreasing electronic coordination of W clusters with the adjacent $C_{60}$ as the cluster grows, before transitioning back to a decreasing mobility regime above a certain size, was presented.

In parallel with the dynamics of cluster diffusion on the surface of the $C_{60}$ surface, there was unambiguous evidence of W atoms intercalating into the bulk of the $C_{60}$ layer and causing the fullerenes to cease their rotation. Evidence of perturbation of the band structure near $E_F$ due to this interaction was scant for a low density of intercalated $C_{60}$.

Higher densities of intercalated W were found in areas where only one ML of $C_{60}$ existed on the surface. In these regions the density of intercalated $C_{60}$ was high and changes to the fullerene electronic structure were found in the vicinity of $E_F$ via STS. Specifically, the band gap in these regions was found to compress significantly.

A switch of substrates to MgO(100) allowed for the deposition of relatively flat, and perhaps epitaxial based on a cubic morphology, layers of W. These surfaces contained striped domains at the atomic scale. When $C_{60}$ was deposited on this surface, the fullerenes organized into FCC(111) layers on most of the surface with some areas showing an amorphous structure that was attributed to variations in surface roughness on the W film.

Upon annealing, all fullerenes desorbed except for the first ML, in accordance with the literature. The remaining fullerenes displayed a unique set of properties. They were metallic, as verified by unambiguous STS measurements, with a significant LDOS at $E_F$. They also had an atomic scale surface corrugation that does not correspond to the molecular orbitals of the $C_{60}$ molecule. Some of these structures were mobile under the influence of the tip and had a size distribution that was very narrow around the size of a fullerene but which broadened considerably with increasing annealing temperature. Under oxidation, these structures showed spectral features suggesting the presence of $WO_3$, yet the atomic-scale ridges remained unaffected.

For all these reasons, these new structures were dubbed nanospheres and it was judged unlikely that these observations could be explained through changes in the chemisorption of the fullerenes with the underlying W. Instead, it seems much more likely the nanospheres incorporate W into their structure in a very significant way. This degree of transformation is unique to the literature. Interactions with a transition metal substrate had been found to result in, at most, a reconstruction of the substrate to maximize coordination with the fullerene layer.

It is not at all clear what the mechanism is that allows these nanospheres to form. In our judgment, the cohesive energy of the W makes an overgrowth of W around the surface of the fullerene unlikely. Instead we propose that a novel metallofullerene structure is formed with incorporation of W atoms into the cage structure. A few papers in the quantum chemistry literature find such structures stable, at least in the limit of only one or two tungsten atoms incorporated into the cage. We propose that for the changes we see, especially the mode of oxidation, significantly more W must be incorporated into the cage structure.

Attempts to image the nanospheres with TEM to determine if they remain hollow were inconclusive. More investigation is certainly warranted to understand the structure and mechanism of its formation, and also to see if other carbide-forming transition metals can also form these structures. One route that could be considered and would allow for some alternative spectroscopic techniques would be metal vapor synthesis, which has successfully been used to form fullerene complexes with Sn, Ir, and Au.[121]

The remainder of the investigation revolved around codeposited films on MgO held at high enough temperatures to ensure the destruction of the fullerene cage and synthesis of carbide thin films of various compositions. The films grown showed cubic morphology with XPS data indicating that the films were dominated by the cubic, metastable $WC_{1-x}$ phase. Extra carbon above what could be incorporated into the $WC_{1-x}$ phase was found to surface segregate, at least in part, and formed surface graphite layers that grew thicker with increasing C/W ratio, with the segregation so significant in the 75/25 sample that it interfered with the growth mechanism of the film.

The $WC_{1-x}$ regions were characterized by small elliptical islands that had a tendency to adopt preferential positions and orientations such that they formed larger parallel stripes on the surface. Atomic scale features were found on this surface that adopted a wide range of periodicities and orientations. A flatter carbide surface would provide a better opportunity to characterize this likely surface reconstruction and its relationship to the bulk lattice structure.

STS measurements of the elliptical islands showed a characteristic spectral shape that showed some variation between well-defined regions. The shape was highly distinct from the graphite that was measured on the surface of the 60/40 and 75/25 films. This proved helpful in the analysis of oxidation of these surfaces.

The 60/40 80 nm surface contained copious graphene-covered areas, certainly a new result for this material system. For the 60/40 surface numerous striped atomic-scale features were found that likely originate from strained graphite and/or Moire patterns of mismatched graphite layers based on the similarity of their STS spectra to graphite spectra.

Oxidation of these carbide surfaces at elevated temperatures showed some common behaviors. For carbide exposed directly to $O_2$ (i.e. not covered by graphite) $WO_3$ formed well-defined islands that grew in size with prolonged or more severe oxidation. There was also suggestive evidence that these islands expanded not just laterally across the surface but into the bulk based on changes to the magnitude of dI/dV outside the bandgap once the surface had been overspread by $WO_{3.}$

There were a variety of intermediate spectral shapes observed between that of the pristine carbide and that of a uniform $WO_3$ layer. For even the mildest oxidations, no region of the surface displayed the spectra of pristine carbide, rather there was a relatively uniform change to the initial carbide spectra that was interpreted to be an initial oxidation to some $WO_{3-x}$ or oxycarbide species separate from the nucleation and growth of the $WO_3$ islands. One concern with this interpretation is that physisorbed oxygen could interfere with the measured spectra, leading to an inability to interpret oxidation in areas not fully oxidized to $WO_3$.

On the graphite-covered surfaces, there was a possible transition between 300 and 400˚C to a regime where $O_2$ exposure led to appreciable etching away of the graphite, exposing the underlying carbide. The degree of oxidation observed implied that the graphite surface layer protected underlying carbide from oxidation until etching away of the graphite was complete.

To see if changes due to oxidation could be reversed, an anneal of one of the thoroughly oxidized surface was performed at 600˚C for 2 hr in UHV. After annealing, surface segregation of carbide led to the re-graphitization of a large fraction of the surface but all un-graphitized areas remained uniformly covered with $WO_3$. There was, however, a large increase in the magnitude of dI/dV outside the bandgap, indicating that the $WO_3$ thickness had decreased such that it no longer interfered with tunneling to the surface as appreciably.

These results, taken together, indicate that annealing an oxidized surface with a supersaturated carbide phase underneath does lead to the partial reversal of oxidation but that it probably occurs at the oxide-carbide interface rather than the surface. Unfortunately, C atoms appear to diffuse easily through the oxide layer and form a surface graphite layer that covers the surface completely before the oxidized surface is converted back to carbide.

Further experiments could determine if less fully oxidized surfaces can be repaired via this anneal method. Also, alternative substrates could be tried that might favor the growth of stable WC phase, which may show different behavior from what was found in this investigation. DFT simulations could also be performed that predict the STS signatures of various oxidized $WC_xO_y$ species as well as the effect of adsorbed oxygen, which would allow for a much fuller interpretation of the spectroscopic data presented thus far.

All together, the results of the last two chapters presented demonstrate that oxidation of metallic surfaces can be investigated fruitfully using STM and STS.

# References

1. Levy, R. B. & Boudart, M. Platinum-Like Behavior of Tungsten Carbide in Surface Catalysis. *Science* **181,** 547–549 (1973).
2. Gubanov, V. A., Ivanovsky, A. L. & Zhukov, V. P. *Electronic Structure of Refractory Carbides and Nitrides*. (Cambridge University Press, 2005).
3. Didziulis, S. V. *et al.* Substrate-Dependent Reactivity of Water on Metal Carbide Surfaces. *J. Phys. Chem. B* **103,** 11129–11140 (1999).
4. Frantz, P., Didziulis, S. V., Merrill, P. B. & Perry, S. S. Spectroscopic and Scanning Probe Studies of Oxygen and Water on Metal Carbide Surfaces. *Tribology Lett.* **4,** 141–148 (1998).
5. Fukui, K., Lo, R.-L., Otani, S. & Iwasawa, Y. Novel Selective Etching Reaction of Carbon Atoms on Molybdenum Carbide by Oxygen at Room Temperature Visualized by Scanning Tunneling Microscopy. *Chem. Phys. Lett.* **325,** 275–280 (2000).
6. Hwu, H. H. & Chen, J. G. Reactions of Methanol and Water Over Carbide-Modified Mo(110). *Surf. Sci.* **536,** 75–87 (2003).
7. Hwu, H. H., Chen, J. G., Kourtakis, K. & Lavin, J. G. Potential Application of Tungsten Carbides as Electrocatalysts. *J. Phys. Chem. B* **105,** 10037–10044 (2001).
8. Kato, M. *et al.* Oxygen Adsorption on a $Mo_2C(0001)$ Surface: Angle-Resolved Photoemission Study. *Surf. Sci.* **601,** 201–208 (2007).
9. Kitchin, J. R., Nørskov, J. K., Barteau, M. A. & Chen, J. G. Trends in the Chemical Properties of Early Transition Metal Carbide Surfaces: A Density Functional Study. *Catal. Today* **105,** 66–73 (2005).
10. Kuramochi, H. *et al.* Surface Reconstruction of TiC(001) and its Chemical Activity for Oxygen. *Appl. Phys. Lett.* **75,** 3784–3786 (1999).
11. Liu, P. & Rodriguez, J. A. Effects of Carbon on the Stability and Chemical Performance of Transition Metal Carbides: A Density Functional Study. *J. Chem. Phys.* **120,** 5414–5423 (2004).
12. Ren, J., Huo, C.-F., Wang, J., Li, Y.-W. & Jiao, H. Surface Structure and Energetics of Oxygen and CO Adsorption on $\alpha$-$Mo_2C(0001)$. *Surf. Sci.* **596,** 212–221 (2005).
13. Ren, J. *et al.* Adsorption of NO, $NO_2$, Pyridine and Pyrrole on $\alpha$-$Mo_2C(0001)$: A DFT Study. *Surf. Sci.* **601,** 1599–1607 (2007).
14. Sürgers, C., Schöck, M. & Löhneysen, H. v. Oxygen-Induced Surface Structure of Nb(110). *Surf. Sci.* **471,** 209–218 (2001).
15. Chaudhuri, S. K. & Lovley, D. R. Electricity Generation by Direct Oxidation of Glucose in Mediatorless Microbial Fuel Cells. *Nat. Biotech.* **21,** 1229–1232 (2003).
16. Rosenbaum, M., Zhao, F., Schröder, U. & Scholz, F. Interfacing Electrocatalysis and Biocatalysis with Tungsten Carbide: A High-Performance, Noble-Metal-Free Microbial Fuel Cell. *Angew. Chem. Int. Edit.* **45,** 6658–6661 (2006).
17. Cheekatamarla, P. K. & Finnerty, C. M. Reforming Catalysts for Hydrogen Generation in Fuel Cell Applications. *J. Power Sources* **160,** 490–499 (2006).
18. Chhina, H., Campbell, S. & Kesler, O. Thermal and Electrochemical Stability of Tungsten Carbide Catalyst Supports. *J. Power Sources* **164,** 431–440 (2007).

19. Weigert, E. C., Zellner, M. B., Stottlemyer, A. L. & Chen, J. G. A Combined Surface Science and Electrochemical Study of Tungsten Carbides as Anode Electrocatalysts. *Top. Catal.* **46,** 349–357 (2007).
20. Harnisch, F., Schröder, U., Quaas, M. & Scholz, F. Electrocatalytic and Corrosion Behaviour of Tungsten Carbide in Near-Neutral pH Electrolytes. *Appl. Catal. B.-Environ.* **87,** 63–69 (2009).
21. Hsu, I. J., Kimmel, Y. C., Dai, Y., Chen, S. & Chen, J. G. Rotating Disk Electrode Measurements of Activity and Stability of Monolayer Pt on Tungsten Carbide Disks for Oxygen Reduction Reaction. *J. Power Sources* **199,** 46–52 (2012).
22. Chen, J. G. Carbide and Nitride Overlayers on Early Transition Metal Surfaces: Preparation, Characterization, and Reactivities. *Chem. Rev.* **96,** 1477–1498 (1996).
23. Reinke, P. & Oelhafen, P. The Molybdenum–Carbon Interface: Formation and Electronic Structure of the Carbide layer. *Surf. Sci.* **468,** 203–215 (2000).
24. Kahn, A., Koch, N. & Gao, W. Electronic Structure and Electrical Properties of Interfaces between Metals and π-Conjugated Molecular Films. *J. Polym. Sci. Pol. Phys.* **41,** 2529–2548 (2003).
25. *Nanostructured Materials for Solar Energy Conversion*. (Elsevier Science, 2007).
26. Shirakawa, T., Umeda, T., Hashimoto, Y., Fujii, A. & Yoshino, K. Effect of ZnO Layer on Characteristics of Conducting Polymer/$C_{60}$ Photovoltaic Cell. *J. Phys. D: Appl. Phys.* **37,** 847 (2004).
27. Halls, J. J. M., Pichler, K., Friend, R. H., Moratti, S. C. & Holmes, A. B. Exciton Diffusion and Dissociation in a Poly(p-phenylenevinylene)/$C_{60}$ Heterojunction Photovoltaic Cell. *Appl. Phys. Lett.* **68,** 3120–3122 (1996).
28. Haddon, R. C. *et al.* $C_{60}$ Thin Film Transistors. *Appl. Phys. Lett.* **67,** 121–123 (1995).
29. Park, H. *et al.* Nanomechanical Oscillations in a Single-$C_{60}$ Transistor. *Nature* **407,** 57–60 (2000).
30. Winkelmann, C. B., Roch, N., Wernsdorfer, W., Bouchiat, V. & Balestro, F. Superconductivity in a Single-$C_{60}$ Transistor. *Nat. Phys.* **5,** 876–879 (2009).
31. Hunt, M. R. C., Modesti, S., Rudolf, P. & Palmer, R. E. Charge Transfer and Structure in $C_{60}$ Adsorption on Metal Surfaces. *Phys. Rev. B* **51,** 10039–10047 (1995).
32. Cepek, C., Goldoni, A. & Modesti, S. Chemisorption and Fragmentation of $C_{60}$ on Pt(111) and Ni(110). *Phys. Rev. B* **53,** 7466–7472 (1996).
33. Murray, P. W., Pedersen, M. Ø., Lægsgaard, E., Stensgaard, I. & Besenbacher, F. Growth of $C_{60}$ on Cu(110) and Ni(110) Surfaces: $C_{60}$-Induced Interfacial Roughening. *Phys. Rev. B* **55,** 9360–9363 (1997).
34. Gall, N., Rut'kov, E. & Tontegode, A. $C_{60}$ Decomposition on Some Transition Metal and Semiconductor Surfaces. *Fullerene Sci. Techn.* **9,** 241 (2001).
35. Liu, H. & Reinke, P. Gold Cluster Formation on $C_{60}$ Surfaces Observed with Scanning Tunneling Microscopy: Au-Cluster Beads and Self-Organized Structures. *Surf. Sci.* **601,** 3149–3157 (2007).
36. Reinke, P. & Oelhafen, P. In Situ Photoelectron Spectroscopy Investigation of Silicon Cluster Growth on Fullerene Surfaces. *Phys. Rev. B* **71,** 045420 (2005).
37. Duffe, S. *et al.* Softlanding and STM Imaging of $Ag_{561}$ Clusters on a $C_{60}$ Monolayer. *Eur. Phys. J. D.* **45,** 401–408 (2007).
38. Wertheim, G. K. & Buchanan, D. N. E. Reaction of $C_{60}$ with Metals: W. *Solid State Commun.* **88,** 97–100 (1993).

39. Hesper, R., Tjeng, L. H. & Sawatzky, G. A. Strongly Reduced Band Gap in a Correlated Insulator in Close Proximity to a Metal. *Europhys. Lett.* **40,** 177–182 (1997).
40. Lu, X., Grobis, M., Khoo, K. H., Louie, S. G. & Crommie, M. F. Charge Transfer and Screening in Individual $C_{60}$ Molecules on Metal Substrates: A Scanning Tunneling Spectroscopy and Theoretical Study. *Phys. Rev. B* **70,** 115418 (2004).
41. Sau, J. D., Neaton, J. B., Choi, H. J., Louie, S. G. & Cohen, M. L. Electronic Energy Levels of Weakly Coupled Nanostructures: $C_{60}$-Metal Interfaces. *Phys. Rev. Lett.* **101,** 026804 (2008).
42. Cho, J. *et al.* Structural and Electronic Decoupling of $C_{60}$ from Epitaxial Graphene on SiC. *Nano Lett.* **12,** 3018–3024 (2012).
43. Ohno, T. R. *et al.* Metal-Overlayer Formation on $C_{60}$ for Ti, Cr, Au, La, and In: Dependence on Metal-C<sub>60<sub> Bonding. *Phys. Rev. B* **47,** 2389–2393 (1993).
44. Lairson, B. M., Visokay, M. R., Sinclair, R., Hagstrom, S. & Clemens, B. M. Epitaxial Pt(001), Pt(110), and Pt(111) Films on MgO(001), MgO(110), MgO(111), and $Al_2O_3$(0001). *Appl. Phys. Lett.* **61,** 1390–1392 (1992).
45. Kohmoto, O. & Jr, C. A. Ferromagnetic Resonance in Epitaxial Fe Films on MgO. *Jpn. J. Appl. Phys.* **31,** 2101–2103 (1992).
46. Hsu, W.-Y. & Raj, R. MgO Epitaxial Thin Films on (100) GaAs as a Substrate for the Growth of Oriented $PbTiO_3$. *Appl. Phys. Lett.* **60,** 3105–3107 (1992).
47. Palmquist, J.-P. *et al.* Magnetron Sputtered W–C Films with $C_{60}$ as Carbon Source. *Thin Solid Films* **444,** 29–37 (2003).
48. Perry, S. S. & Merrill, P. B. Preparation and Characterization of MgO(100) Surfaces. *Surf. Sci.* **383,** 268–276 (1997).
49. Cukauskas, E. ., Kirchoefer, S. W. & Chang, W. Morphology and Dielectric Properties of $Ba_{0.5}Sr_{0.5}TiO_3$ Thin Films on Annealed (100)MgO. *J. Cryst. Growth* **236,** 239–247 (2002).
50. Suzuki, T. M., Morimoto, Y. Y. S. & Shimizu, T. Annealing Temperature Dependence of MgO Substrates on the Quality of $YBa_2Cu_3O_x$ Films Prepared by Pulsed Laser Ablation. *Jpn. J. Appl. Phys.* **34,** 4038–4042 (1995).
51. Curl, R. F. & Smalley, R. E. Probing $C_{60}$. *Science* **242,** 1017–1022 (1988).
52. Kroto, H. W., Heath, J. R., O'Brien, S. C., Curl, R. F. & Smalley, R. E. $C_{60}$: Buckminsterfullerene. *Nature* **318,** 162–163 (1985).
53. Shin, H. *et al.* Floating Two-Dimensional Solid Monolayer of $C_{60}$ on Graphite. *Phys. Rev. B* **82,** 235427 (2010).
54. Haddon, R. C. *et al.* Conducting Films of $C_{60}$ and $C_{70}$ by Alkali-Metal Doping. *Nature* **350,** 320–322 (1991).
55. Iwasa, Y. & Takenobu, T. Superconductivity, Mott–Hubbard states, and Molecular Orbital Order in Intercalated Fullerides. *J. Phys.: Condens. Matter* **15,** R495 (2003).
56. Nagao, S., Kurikawa, T., Miyajima, K., Nakajima, A. & Kaya, K. Formation and Structures of Transition Metal−$C_{60}$ Clusters. *J. Phys. Chem. A* **102,** 4495–4500 (1998).
57. Balch, A. L. & Olmstead, M. M. Reactions of Transition Metal Complexes with Fullerenes ($C_{60}$, $C_{70}$, etc.) and Related Materials. *Chem. Rev.* **98,** 2123–2166 (1998).
58. Moffatt, W. G. & Operation, G. E. C. R. and D. C. T. M. *The handbook of binary phase diagrams*. (General Electric Company, Corporate Research and Development, Technology Marketing Operation, 1981).
59. Meyer, E., Hug, H. J. & Bennewitz, R. *Scanning Probe Microscopy: The Lab on a Tip*. (Springer, 2003).

60. Stroscio, J. A., Feenstra, R. M. & Fein, A. P. Electronic Structure of the Si(111)2 × 1 Surface by Scanning-Tunneling Microscopy. *Phys. Rev. Lett.* **57,** 2579–2582 (1986).
61. Stroscio, J. A. & Kaiser, W. J. *Scanning Tunneling Microscopy*. **27,** (Academic Press, 1993).
62. Woodruff, D. P. & Delchar, T. A. *Modern Techniques of Surface Science*. (Cambridge University Press, 1994).
63. Lamb, R. N., Baxter, J., Grunze, M., Kong, C. W. & Unertl, W. N. An XPS Study of the Composition of Thin Polyimide Films Formed by Vapor Deposition. *Langmuir* **4,** 249–256 (1988).
64. Chen, W. & Roberts, J. T. Adsorption and Reaction of $WF_6$ on W(100). *Surf. Sci.* **324,** 169–184 (1995).
65. Ekinci, K. L. & Valles, J. M. Morphology of Quench Condensed Pb Films near the Insulator to Metal Transition. *Phys. Rev. Lett.* **82,** 1518–1521 (1999).
66. Vinod, C. P., Kulkarni, G. U. & Rao, C. N. R. Size-Dependent Changes in the Electronic Structure of Metal Clusters as Investigated by Scanning Tunneling Spectroscopy. *Chem. Phys. Lett.* **289,** 329–333 (1998).
67. Marcus, P. & Hinnen, C. XPS Study of the Early Stages of Deposition of Ni, Cu and Pt on HOPG. *Surf. Sci.* **392,** 134–142 (1997).
68. Vijayakrishnan, V. & Rao, C. N. R. An Investigation of Transition Metal Clusters Deposited on Graphite and Metal Oxide Substrates by a Combined Use of XPS, UPS and Auger Spectroscopy. *Surf. Sci.* **255,** L516–L522 (1991).
69. Piednoir, A. *et al.* Atomic Resolution on Small Three-Dimensional Metal Clusters by STM. *Surf. Sci.* **391,** 19–26 (1997).
70. Binns, C., Baker, S. H., Demangeat, C. & Parlebas, J. C. Growth, Electronic, Magnetic and Spectroscopic Properties of Transition Metals on Graphite. *Surf. Sci. Rep.* **34,** 107–170 (1999).
71. Wepasnick, K. A. *et al.* Surface Morphologies of Size-Selected $Mo_{100\pm2.5}$ and $(MoO_3)_{67\pm1.5}$ Clusters Soft-Landed onto HOPG. *J. Phys. Chem. C* **115,** 12299–12307 (2011).
72. Granqvist, C. G. & Buhrman, R. A. Log-Normal Size Distributions of Ultrafine Metal Particles. *Sol. St. Comm.* **18,** 123–126 (1976).
73. Bardotti, L., Prével, B., Treilleux, M., Mélinon, P. & Perez, A. Deposition of Preformed Gold Clusters on HOPG and Gold Substrates: Influence of the Substrate on the Thin Film Morphology. *Appl. Surf. Sci.* **164,** 52–59 (2000).
74. Winkler, C., Carew, A., Raval, R., Ledieu, J. & McGRATH, R. Scaling Parameters for Gold and Copper Cluster Growth on an Alumina Single Crystal Surface. *Surf. Rev. Lett.* **08,** 693–697 (2001).
75. Liu, H., Lin, Z., Zhigilei, L. V. & Reinke, P. Fractal Structures in Fullerene Layers: Simulation of the Growth Process. *J. Phys. Chem. C* **112,** 4687–4695 (2008).
76. Szuba, S., Czajka, R., Kasuya, A., Wawro, A. & Rafii-Tabar, H. Observation of $C_{60}$ Film Formation on a Highly Oriented Pyrolitic Graphite Substrate via Scanning Tunnelling Microscopy. *Appl. Surf. Sci.* **144–145,** 648–652 (1999).
77. Hashizume, T. *et al.* Intramolecular Structures of $C_{60}$ Molecules Adsorbed on the Cu(111)-(1×1) Surface. *Phys. Rev. Lett.* **71,** 2959–2962 (1993).
78. Meakin, P., Vicsek, T. & Family, F. Dynamic Cluster-Size Distribution in Cluster-Cluster Aggregation: Effects of Cluster Diffusivity. *Phys. Rev. B* **31,** 564–569 (1985).

79. Dresselhaus, M. S., Dresselhaus, G. & Eklund, P. C. *Science of Fullerenes and Carbon Nanotubes: Their Properties and Applications*. (Academic Press, 1996).
80. Lu, X., Grobis, M., Khoo, K. H., Louie, S. G. & Crommie, M. F. Spatially Mapping the Spectral Density of a Single $C_{60}$ Molecule. *Phys. Rev. Lett.* **90,** 096802 (2003).
81. Tang, K., Jin, X. & Tang, Y. Syntheses, Structures, and Properties of Novel Molybdenum and Tungsten Complexes of Fullerenes. *Phys. Solid State* **44,** 612–614 (2002).
82. Lin, H. *et al.* Many-Body Effects in Electronic Bandgaps of Carbon Nanotubes Measured by Scanning Tunnelling Spectroscopy. *Nat. Mater.* **9,** 235–238 (2010).
83. Gall', N. R., Rut'kov, E. V. & Tontegode, A. Y. Interaction of $C_{60}$ Molecules with the (100)W Surface: Adsorption, Initial Stages of Film Growth, and Thermal Transformation of the Adsorption Layer. *Semiconductors* **38,** 1023–1029 (2004).
84. Wertheim, G. K. & Buchanan, D. N. E. Interfacial Reaction of $C_{60}$ with Silver. *Phys. Rev. B* **50,** 11070–11073 (1994).
85. J.E. Rowe *et al.* Synchrotron Radiation and Low Energy Electron Diffraction Studies of Ultrathin $C_{60}$ Films Deposited on Cu(100), Cu(111) and Cu(110). *Int. J Mod. Phys. B* **6,** 3909 (1992).
86. Thürmer, K., Koch, R., Weber, M. & Rieder, K. H. Dynamic Evolution of Pyramid Structures during Growth of Epitaxial Fe (001 ) Films. *Phys. Rev. Lett.* **75,** 1767–1770 (1995).
87. Kato, M., Wada, M., Sato, A. & Mori, T. Overview no. 78 Epitaxy of Cubic Crystals on (001) Cubic Substrates. *Acta. Metall. Mater.* **37,** 749–756 (1989).
88. Szczudło, Z., Zuber, S. & Ciszewski, A. Cleaning of W(001) by Ar-ion Bombardment for STM Investigation. *Vacuum* **72,** 47–52 (2003).
89. Bode, M., Pascal, R. & Wiesendanger, R. STM Study of Carbon-Induced Reconstructions on W(110): Strong Evidence for a Surface Lattice Deformation. *Surf. Sci.* **344,** 185–191 (1995).
90. Jackson, A. M., Myerson, J. W. & Stellacci, F. Spontaneous Assembly of Subnanometre-Ordered Domains in the Ligand Shell of Monolayer-Protected Nanoparticles. *Nat. Mater.* **3,** 330–336 (2004).
91. Cesbron, Y., Shaw, C. P., Birchall, J. P., Free, P. & Lévy, R. Stripy Nanoparticles Revisited. *Small* **8,** 3714–3719 (2012).
92. Büttner, M. & Reinke, P. Fullerene Nanostructures on Defect-Rich Graphite Surfaces. *J. Phys. Chem. C* **113,** 8107–8111 (2009).
93. Altman, I. S. *et al.* Zero-Phonon Lines in the Photoluminescence Spectra of MgO:$Mn^{2+}$ Nanocrystals. *Phys. Rev. B* **68,** 125324 (2003).
94. Nasibulin, A. G. *et al.* In Situ TEM Observation of MgO Nanorod Growth. *Cryst. Growth Des.* **10,** 414–417 (2010).
95. Stankic, S., Cottura, M., Demaille, D., Noguera, C. & Jupille, J. Nucleation and Growth Concepts Applied to the Formation of a Stoichiometric Compound in a Gas Phase: The Case of MgO Smoke. *J. Cryst. Growth* **329,** 52–56 (2011).
96. Reinke, P. *Inorganic Nanostructures: Properties and Characterization*. (Wiley-VCH, 2012).
97. Halperin, W. P. Quantum Size Effects in Metal Particles. *Rev. Mod. Phys.* **58,** 533–606 (1986).
98. Long, N. H. *et al. Spin Relaxation and the Elliott-Yafet Parameter in W(001) Ultrathin Films: Surface States, Anisotropy and Oscillation Effects*. (2013). at <http://arxiv.org/abs/1302.0140>

99. Infante, I., Gagliardi, L. & Scuseria, G. E. Is Fullerene $C_{60}$ Large Enough to Host a Multiply Bonded Dimetal? *J. Am. Chem. Soc.* **130,** 7459–7465 (2008).

100. Guevara, J., Weissmann, M. & Llois, A. M. The Functional Dependence of the Cohesive Energy on Coordination in Transition-Metal Systems. *J. Phys.: Condens. Matter* **6,** 3939 (1994).

101. Pan, H., Feng, Y. P. & Lin, J. Hydrogen Adsorption by Tungsten Carbide Nanotube. *Appl. Phys. Lett.* **90,** 223104–223104–3 (2007).

102. Ganji, M. D. Theoretical Study of the Adsorption of $CO_2$ on Tungsten Carbide Nanotubes. *Phys. Lett. A* **372,** 3277–3282 (2008).

103. Ibrahim, M., El-Haes, H. & Jalbout, A. F. Semiempirical Molecular Modelling Study of $C_{60}$ Doped with Silicon, Germanium, and Aluminium. *Chin. J. Phys.* **44,** 432–39 (2006).

104. Neeraj Misra, Apoorva Dwivedi & Anoop Pandey. Geometrical Electronic, and Vibrational Properties of Fullerene Rings Doped with Transition Metals. *Chin. J. Phys* **50,** 64–72 (2012).

105. Rong, Z. Y. & Kuiper, P. Electronic Effects in Scanning Tunneling Microscopy: Moiré Pattern on a Graphite Surface. *Phys. Rev. B* **48,** 17427–17431 (1993).

106. Fukui, N. *et al.* Moiré Image Patterns on Double-Walled Carbon Nanotubes Observed by Scanning Tunneling Microscopy. *Phys. Rev. B* **79,** 125402 (2009).

107. Voevodin, A. A., O’Neill, J. P., Prasad, S. V. & Zabinski, J. S. Nanocrystalline WC and WC/a-C Composite Coatings Produced from Intersected Plasma Fluxes at Low Deposition Temperatures. *J. Vac. Sci. Technol., A* **17,** 986–992 (1999).

108. Aizawa, T., Hishita, S., Tanaka, T. & Otani, S. Surface Reconstruction of $W_2C(0001)$. *J. Phys.: Condens. Matter* **23,** 305007 (2011).

109. Moulder, J. F. & Chastain, J. *Handbook of X-Ray Photoelectron Spectroscopy: A Reference Book of Standard Spectra for Identification and Interpretation of XPS Data*. (Perkin-Elmer Corporatioon, Physical Electronics Division, 1992).

110. Pauleau, Y. & Gouy-Pailler, P. Characterization of Tungsten-Carbon Layers Deposited on Stainless Steel by Reactive Magnetron Sputtering. *J. Mater. Res.* **7,** 2070–2079 (1992).

111. Cavaleiro, A., Vieira, M. T. & Lempériere, G. The Structure of Thin Films Deposited from a Sintered Tungsten Carbide with a High Cobalt Content (15 wt.%). *Thin Solid Films* **185,** 199–217 (1990).

112. Srivastava, P. K., Vankar, V. D. & Chopra, K. L. Very Hard W–C Coatings on Stainless Steel by RF Reactive Magnetron Sputtering. *J. Vac. Sci. Technol., A* **4,** 2819–2826 (1986).

113. Muehlhoff, L., Choyke, W. J., Bozack, M. J. & Yates, J. T. Comparative Electron Spectroscopic Studies of Surface Segregation on SiC(0001) and SiC(0001). *J. Appl. Phys.* **60,** 2842–2853 (1986).

114. Dixon, R. A. *et al.* Electronic States at Oxygen Deficient $WO_3(001)$ Surfaces: a Study by Resonant Photoemission. *Surf. Sci.* **399,** 199–211 (1998).

115. Malagù, C. *et al.* Photo-Induced Unpinning of Fermi Level in $WO_3$. *Sensors* **5,** 594–603 (2005).

116. Katrib, A., Hemming, F., Wehrer, P., Hilaire, L. & Maire, G. The Multi-Surface Structure and Catalytic Properties of Partially Reduced $WO_3$, $WO_2$ and WC + $O_2$ or W + $O_2$ as Characterized by XPS. *J. Electron. Spectrosc. Relat. Phenom.* **76,** 195–200 (1995).

117. Warren, A., Nylund, A. & Olefjord, I. Oxidation of Tungsten and Tungsten Carbide in Dry and Humid Atmospheres. *Int. J. Refract. Met. H.* **14,** 345–353 (1996).

118. Khyzhun, O. Y. XPS, XES and XAS Studies of the Electronic Structure of Tungsten Oxides. *Journal of Alloys and Compounds* **305,** 1–6 (2000).
119. Ribeiro, C. A., Souza, W. R. de, Crespi, M. S., Neto, J. A. G. & Fertonani, F. L. Non-Isothermal Kinetic of Oxidation of Tungsten Carbide. *J. Therm. Anal. Calorim.* **90,** 801–805 (2007).
120. Xiaowei, L., Jean-Charles, R. & Suyuan, Y. Effect of Temperature on Graphite Oxidation Behavior. *Nucl. Eng. Des.* **227,** 273–280 (2004).
121. Zhao, W. *et al.* Metal Vapor Synthesis of Air-Sensitive Transition Metal Fullerides: Evidence of IR Spectra. *Sol. St. Comm.* **92,** 313–317 (1994).